Doctoral Dissertation

Development of a blood-brain barrier capillary network model for assessing transport of cancer microenvironment sensitive polymer drugs

PIANTINO MARIE VIRGINIE

June 2022

Graduate School of Engineering
Osaka University

Content

General Introduction

Pharmaceutical drug development is a lengthy and highly expensive process, whose costs have steadily increased over recent decades, due to the development of new modalities such as RNA therapeutics, antibody drug conjugates, or gene therapy [1,2]. Drug candidate libraries must be tested against potential targets, as well as drug side effects and toxicity towards human tissue to allow their commercialization [3]. The permeation mechanism and the delivery efficiency of intravenously injected drugs to the brain are also poorly understood. In particular, drug candidates for neurological pathologies have higher failure rates at the bench-to-bed transition than any other drugs [4]. It has been demonstrated that of the mere 8% of candidates reaching the initial Phase 1 of human safety testing, only a limited number received commercial approval [1]. The adverse effects on the brain microvasculature are still poorly understood, and the question is whether they arise from endogenous pathological mechanisms or from the drugs themselves. Damage or dysfunction of the brain vasculature are often associated with many neurological diseases, including brain cancers. Glioblastoma multiform (GBM) is not only one of the most common forms of brain cancer in adults, but also one of the deadliest brain tumors, with a median survival of 12 months with appropriate treatments. It is also one of the most vascularized brain cancers, and is associated with a high remodeling of the extracellular matrix (ECM). There has been intensive research dedicated to modeling the characteristic features of GBM in order to understand its impact on brain vascularization, particularly the regulation of the angiogenic signaling pathways, as microvascular proliferation is a hallmark of GBM [5,6]. It is important to modeling pathological tissues for improving evaluation accuracy of the treatments for brain diseases.

The shortage of effective therapies and low success rate of investigational drugs are partly due to the lack of reliable models to effectively screen potential therapeutic molecules, especially the brain [7]. Animal models are commonly used in pharmaceutical and industrial research for the assessment of drug toxicity and efficacy and pharmacokinetic studies. They remain however poor predictors of drug safety in humans due to interspecies differences. The relevance and related ethical issues arising from animal models also limit their use for the investigation of drug delivery in the brain [8]. Although there have been rising concerns about the use of animals for drug delivery and toxicological assays, they continue to be used worldwide for scientific purposes. A recent study by Taylor and Alvarez has estimated the animal testing numbers worldwide, with an increase from 115.2 million animals to 192.1 million between 2005 and 2015 [9]. According to European Union definitions, China and Japan

were ranked first and third place for animal uses in 2015, with estimated 20.5 and 5 million procedures, respectively [9]. It thus seems unlikely to see a significant reduction of animal testing in the immediate future. Nevertheless, there have been increasing efforts from the scientific community and pharmaceutical companies to limit the proportion of animal research, whenever possible, through the development of alternative techniques, such as advanced biomimetic *in vitro* cellular models of the brain microvasculature.

In the average human adult brain, the surface exchange area between itself and the vascular system is between 12 and 18 m^2 [10]. Blood vessels can be categorized depending on their size and diameter, with large vessels (>6 mm in diameter), small vessels (1-6 mm) and microvessels or capillaries (<1 mm) [11]. The brain vasculature is a highly complex network which comprises of arteries and arterioles, capillaries, venules and veins. The large surface exchange area is mainly due to the presence of the brain microvasculature comprising more than 100 billion capillaries, with a density of about 500 m/cm^3, which correspond to an average length of about 600 km [10,12]. Modeling the brain microvasculature is thus of importance to collect more relevant *in vitro* data simulating the drug permeation or toxicity assessment of compounds in the brain for improved clinical translations. Notably, the *in vitro* blood-brain barrier (BBB) models can provide a valuable tool for investigating the transport of drugs into the brain [13]. The BBB represents a physical and metabolic barrier that separates the periphery from the brain tissue. The BBB comprises brain microvascular endothelial cells (BMEC) are surrounded by supporting cells, pericytes (PCs) and astrocytes (ACs), themselves unsheathed in the basement membrane (BM) (**Figure 1**).

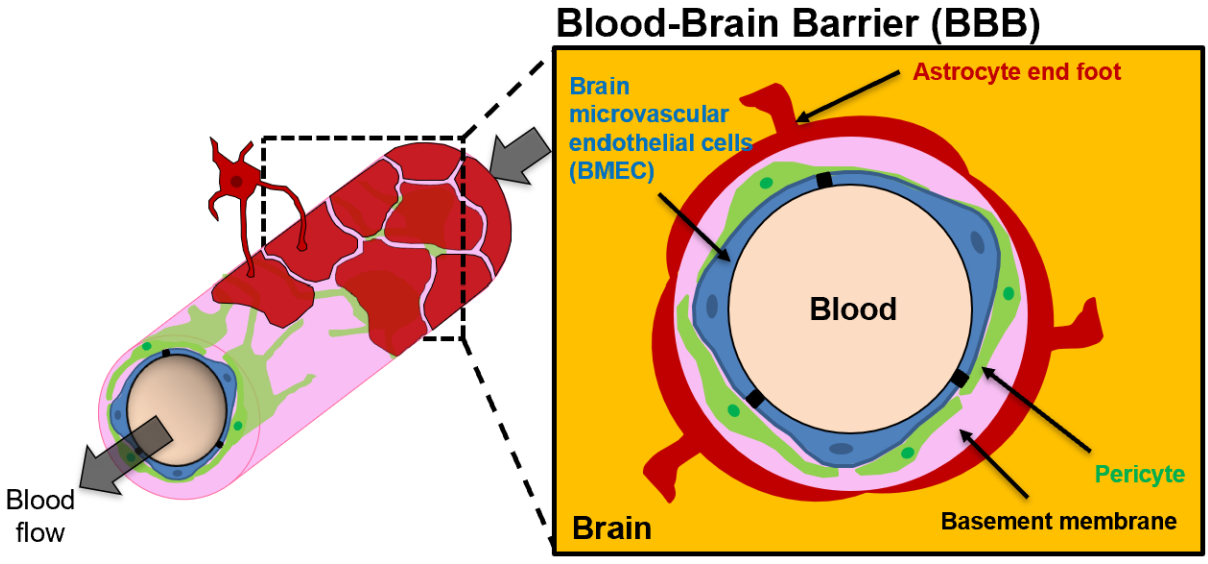

Figure 1. Structure of the Blood-Brain Barrier (BBB).

The BBB plays an important role in brain homeostasis by regulating the exchange of substances between blood and brain parenchyma for enabling sufficient brain nutrition and oxygenation, wastes removal [14], and by preventing the entry of neurotoxic substances circulating in the blood. The restrictive permeability mainly arises from the presence of highly specialized BMEC. The brain endothelium indeed greatly differs from that in the rest of the human body since the BMEC are highly polarized, display minimal vesicular trafficking, and have high expression of tight junction proteins (TJs) between adjacent BMEC [15]. They also express solute carriers that regulate the transport of ions and small molecules and exhibit receptor-mediated processes for the specific uptake of macromolecules.

The presence of TJs between the BMEC lead to high endothelial electrical resistance and low paracellular permeability. The transendothelial electrical resistance (TEER) reflects the junction development and barrier integrity. Although TEER values across human brain endothelium cannot be measured *in vivo*, TEER measurements performed on rat and frog brains have been estimated to be around 1500-2000 Ω x cm^2, much higher than the 3-33 Ω x cm^2 in the other tissues [16]. The BBB regulates the transport of nutrients and ions in the brain tissue but also impedes the brain uptake of potentially harmful substances and neurotherapeutics. Generally, paracellular transport is limited to small lipid drugs with molecular weight (MW) no more than 450 Da, hydrogen bonds acceptor less than 7, hydrogen bonds donor less than 3, and with a calculated logarithm of the partition coefficient between *n*-octanol and water (CLogP) less than 5 [17]. Moreover, it is reported that the BBB prevents 98% of small molecular drugs and almost 100% of macromolecular drugs from entering the brain via circulation [17], making the drug delivery a considerable challenge for the treatment of brain diseases. Other transportation routes should be therefore considered for the transportation of large-sized therapeutics, for example the new modalities such as antibody-drug conjugates, polypeptides and oligonucleotides, which have a MW above that threshold.

Alternatively, metabolites can also be delivered into the brain by specific transporters expressed on the BMEC membrane. Among them, the transferrin receptor (TfR)-mediated transcytosis is available for the brain delivery of large-sized molecules. The TfR, a homodimeric transmembrane protein of 180 kDa, is responsible for the transport of transferrin-bound iron into the brain [18]. Iron is required for several fundamental biological processes that maintain normal neurological functions (oxygen transport, neurotransmitter metabolism, DNA synthesis) [19]. The crystal structure of the human TfR shows the presence of three regions in the extracellular space : a protease-like domain in contact with the cell membrane, a helical

domain comprising the dimer contact regions and an apical domain (**Figure 2**) [20]. The delivery of iron to the brain is enabled by the binding and intracellular trafficking of the iron bound to the transferrin (Tf), which is the native ligand of the TfR, with a dissociation constant K_d of 0.22 nM [21]. The Tf is a 80 kDa glycoprotein which contains two lobes of ~40 kDa, the N- and C-lobes, which shares similar sequence and structure. Each lobe comprises two domains, with N-I and N-II in the N-lobe and C-I and C-II in the C-lobe. One ferric ion (Fe^{3+}) binds in a region of the Tf located at the interface between the two domains of each lobe. The Tf can bind up to two Fe^{3+} ions (Fe_2-Tf), and two iron-bearing Tf molecules can bind the dimeric TfR (**Figure 3**).

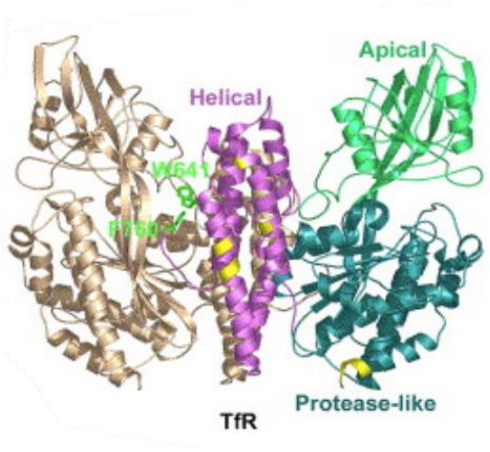

Figure 2. Structure of the TfR homodimer alone. One of the TfR chains is colored in brown and the other is color coded to differentiate the three domains [20].

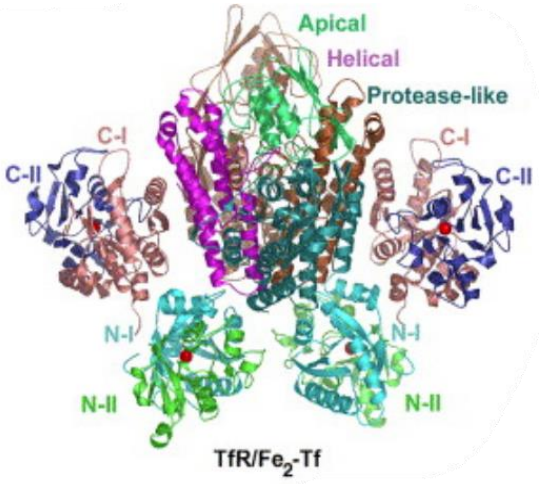

Figure 3. Structure of the TfR homodimer bound to Fe_2-Tf. The red dots represent the Fe^{3+} ions [20].

The TfR has gained particular attention due to its high expression level by both BMECs and brain cancer cells [22], making it an attractive target for the specific delivery of drugs into the brain and the tumor site. Various drug delivery systems (DDS) have been designed for improving the delivery efficiency of drugs into the brain by adding moieties targeting this transportation route for an enhanced transport across the BBB [29–33]. Assessing the functionality of TfR-mediated transport in the *in vitro* BBB models is therefore highly desired, as it could create opportunities for the screening of novel treatments of central nervous system (CNS) diseases.

Many studies have attempted to model the dynamic and complex structure that represents the brain vasculature for a better understanding of drug permeation in the brain, from simple transwell cultures to more complicated microfluidic systems (**Figure 3**).

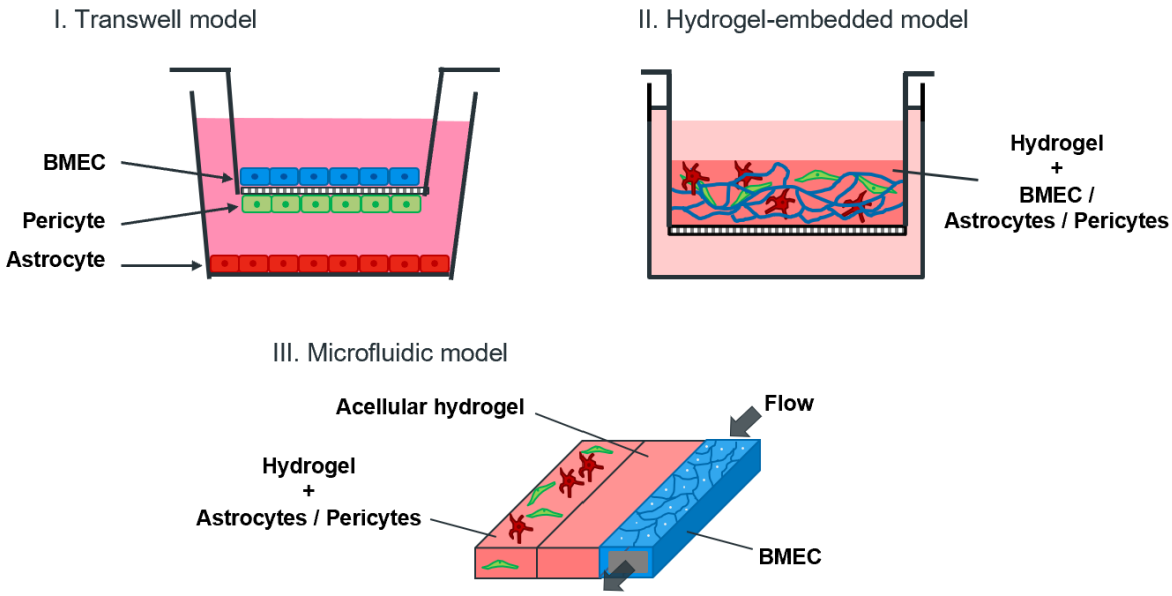

Figure 3. Schematic illustration of the construction of *in vitro* BBB models.

I. Transwell culture

For several decades, transwell cultures have been extensively used to predict drug permeability due to their simplicity, scalability and reproducibility. Transwell models typically comprise of a BMEC monolayer grown of the top of the porous polyester member of a culture insert, which is then suspended on the top of a well in a multi-well plate. More complex BBB model can be obtained by the co-culture with pericytes and/or astrocytes [29–31]. Each cell type can be physically separated by attaching them on both sides of the transwell or on the bottom of the well plate. For transport assays, the tested molecules can be loaded in the top ("blood" side) chamber and their accumulation in the bottom ("brain" side) chamber can be measured over time.

Although this system represents a cost-effective and reproducible method, it fails to accurately mimic some important BBB features and extracellular matrix (ECM) microenvironment which are critical factors for proper cellular differentiation and the polarization of the cells [4,28]. The two-dimensional (2D) configuration and the presence of artificial polyester membrane indeed reduce the possibility of the three cell types of the BBB to communicate directly and make physical contact with each other [31,32]. It is however known that a direct contact between BMEC and astrocytes is important to achieve a significant reduction in paracellular transport of models compounds as compared monoculture and indirect coculture [33–35].

II. Matrix embedded models using extracellular matrix or synthetic materials

The incorporation of a three-dimensional (3D) matrix is important in vascular and neural tissue engineering as it provides support and comprises appropriate ECM factors that enable the recapitulation of the morphological and functional characteristics of those cells. For a more relevant 3D microenvironment, the choice of material is a key factor to take into account when designing the cell scaffold. Cells of the BBB are mixed in a matrix made of native or synthetic materials to provide a scaffold that supports cell migration, cell-cell interaction and the formation of a self-organized vascular network, with sometimes the presence of lumen.

Synthetic materials possess many advantages that make them attractive for tissue engineering, such as the possibility to finely tune the mechanical properties and degradation rates by modifying the crosslinking degree or the composition. The porosity can be modulated by adjusting polymer chain lengths and density for supporting cell migration and vasculogenesis processes. Biocompatible synthetic materials used for modeling brain microvasculature include polymers such as poly(ethyl acrylate), poly(hydroxyethyl acrylate), poly(methacrylic acid) [36], or polyethylene glycol [37], which can be further modified with binding peptide sequences, such as arginylglycylaspartic acid (RGD), for promoting cell adhesion.

Natural materials can also be used because they are inherently bioactive, contain endogenous binding motifs for cell adhesion and cell infiltration, and also exhibit similar mechanical properties as the soft brain tissues. Such materials include type I collagen matrix [38–41], decellularized ECM (dECM) [42,43] and Matrigel [44,45]. Type I collagen is present in most human tissues including the brain, even though its concentration is considered to be lower than in other parts of the body [46]. Although it is known that collagens are not abundant in the brain ECM and are only limited to the vascular BM [47], type I collagen remains the most extensively used scaffold due to its easy access and mechanical tunability. Hydrogel made from type I collagen microfibers allowed to reach a stiffness and a Young's modulus close to mammalian brains [39,41]. Matrigel® is a soluble and sterile extract of BM from a mouse sarcoma tumor (Engelbreth–Holm–Swarm), which is characterized by a high content of ECM proteins. However, its highly variable composition and stiffness among production lots limit its potential use [48]. Decellularized ECM, characterized by the removal of native cells, can represent a good alternative for maintaining native tissue ECM components in terms of protein composition and growth factors as well as physical properties [43]. Brain dECM is however usually not from human source but usually from porcine or rodent origins [49,50], which can potentially affect the

relevance of the BBB model. The ECM origin and composition should indeed be carefully considered to ensure the accurate replication of the brain vasculature *in vitro*.

Although hydrogel-based models show compatibility for high-throughput screening (HTS), it lacks connection with the outside of the hydrogel in order to enable the perfusion of tested molecules inside the lumen of the blood capillary network, as seen in the native BBB when a drug is injected intravenously. The lack of exposure of BMEC to the physiological mechanical forces such as shear stress also prevents the induction of their BBB phenotype [51].

III. Microfluidic models

Microfluidic platforms have recently emerged to address the issues of transwell and hydrogel-based models by offering a closer representation of the *in vivo* microenvironment. In physiological conditions, the blood flow has mechanotransductive effects on BMEC, known to be of great importance for cell differentiation and TJ formation [52]. Indeed, shear stress developed by blood flow can increase TJ proteins and reduces the permeability properties. Therefore, more advanced BBB models have been developed using different materials, designs, and strategies, allowing for media to flow, hence generating a shear stress.

These "organ-on-chip" BBB models can reproduce a 3D multicellular configuration by co-culture of several types of BBB cells, physiochemical microenvironment, vascular perfusion under physiological shear stress [53]. An endothelium monolayer is, in most cases, seeded on the inner walls of rigid channels often made of polymers such as polydimethylsiloxane or polypropylene. These walls are pre-coated with adhesive proteins such as fibronectin to facilitate BMEC adhesion. BMEC are allowed to adhere under static conditions during a short period of time (usually 24 hours) before flow perfusion. For example, systems of perfused vessels in co-culture with supporting cells were engineered [54,55]. However, no direct cell-cell contact was possible between the endothelial cells and the supporting cells since they were physically separated by an acellular type I collagen gel or polycarbonate membrane, limiting the cell interactions to paracrine exchanges solely. Moreover, some of these models have a large vessel diameter (~600-800 µm) [54,56], which is much higher than the actual *in vivo* dimensions of the human BBB vasculature, composed of arterioles and venules (10-90 µm diameter) and capillaries (7-10 µm diameter) [57]. As these models cannot effectively recapitulate BBB microvasculature morphology, it may lead to an inaccurate reproduction of the blood flow and transport exchange events occurring in brain capillaries. Although this diameter could be greatly reduced below 30 µm of outer diameter in self-organization models [33,58,59], the "brain" side remains not easily accessible for the sample collection and in-depth composition analysis

after transport assays. Despite their advantages and potential development pathways, microfluidic platforms are still not widely used for HTS due to the difficulty of handling, and the special and expensive equipment required. Moreover, as for now, the number of samples per device is still limited, making the translation to HTS laborious [54,58].

Current *in vitro* BBB models cannot reproduce the human structural complexity of the brain microvasculature, and thus their functions are not enough for drug assessments. Therefore, the fabrication of 3D BBB with a structure similar to the native BBB which recapitulates the essential functions of the BBB, including barrier function properties sufficient to restrict the passage of molecules and functional transportation routes, such as the TfR-mediated transcytosis, is highly desired. Ideally, the 3D BBB model should be prepared in a format compatible with HTS and exhibit a perfusable blood capillary network in order to perform transport assays.

In this thesis, the author aimed to develop a robust 3D self-assembled microvascular network formed by BMEC covered by pericytes and astrocyte end feet inside the hydrogel. It exhibited perfusable microvasculature due to the presence of capillary opening structures on the bottom of the hydrogel, which is highly needed for performing permeability assays (**Figure 4**). The structure, the molecular permeability and the functionality of the transporters were evaluated in this 3D BBB model. Additionally, the possibility of using human induced pluripotent stem cells derived BMEC-like cells (hiPS-BMEC) as a BMEC source for the 3D BBB model was also investigated regarding their BBB-specific gene and protein expression profile, as well as their barrier function properties. The functionality of the TfR-mediated transcytosis on hiPS-BMEC was also assessed by permeability assays, competitive binding assays and confocal microscopy observations. Finally, in order to show potential applications of the 3D BBB model for HTS, a cancer-microenvironment responsive drug-free chemotherapy, named Molecular Block, was synthesized. This polymeric construct could potentially serve as a template molecule for the fabrication of drug-free chemotherapy treating brain diseases, which could be screened in a tumor model of the 3D BBB open capillary network.

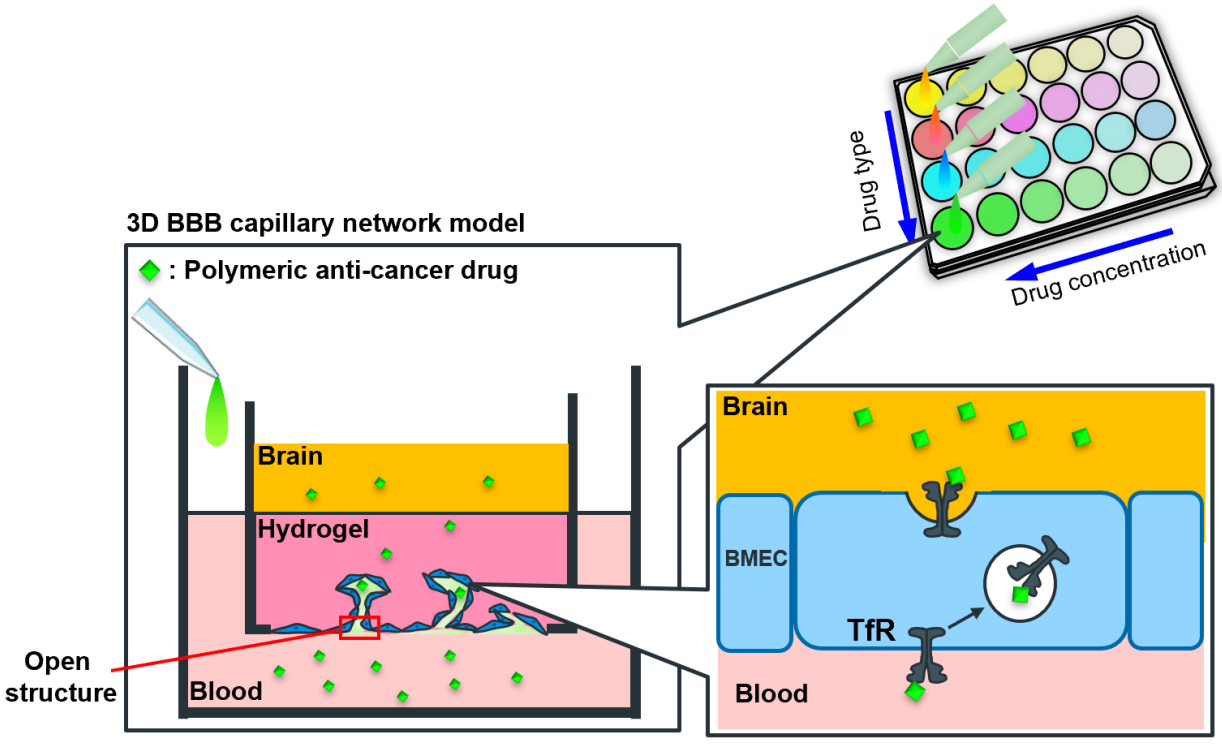

Figure 4. Schematic illustration of the fabrication of 3D BBB model for assessing the transport of polymeric anti-cancer drugs which can be transported by TfR-mediated transcytosis.

Outline of this thesis

In this thesis, the author describes the fabrication of a 3D blood-brain barrier (BBB) capillary network model for assessing the transport of anti-cancer drugs and cancer-microenvironment sensitive polymeric drug-free chemotherapy. This thesis includes the following three chapters.

Chapter 1.

Development of a three-dimensional blood-brain barrier network with opening capillary structures for drug transport screening assays

In this chapter, a 3D BBB model with perfusable open capillary structures at the bottom of the hydrogel was established. Studies in this chapter focused on the evaluation of the barrier function properties and the functionality of the TfR-mediated transcytosis by the BMEC capillary network by permeability assays.

Chapter 2.

Brain microvascular endothelial cells derived from human induced pluripotent stem cells as *in vitro* model for assessing blood-brain barrier transferrin receptor-mediated transcytosis

The source of BMEC is important to consider for the reproduction of the BBB properties *in vitro*. Human induced pluripotent stem cells derived BMEC-like cells (hiPS-BMEC) have recently generated great opportunities for the BBB modeling as they exhibit a paracellular tightness similar to the native BBB. In this study, the possibility of hiPS-BMEC for BBB modelling was investigated, particularly regarding their size-selective permeation and TfR-mediated transcytosis ability. Finally, as an applicative validation, two candidate peptides previously reported to be internalized using the TfR were screened with respect to their permeability ability across the hiPS-BMEC monolayer.

Chapter 3

Development of Highly Sensitive Molecular Blocks at Cancer Microenvironment for Rapid Cancer Cell Death

In this study, a drug-free chemotherapy named Molecular Block (MB) was prepared. The MB can form self-assembled aggregates on the cancer cell surfaces in response to the weak acid condition, leading to subsequent cancer cell death by membrane disruption. The effect of the hydrophilic-hydrophobic balance in the MB was discussed regarding their pH-dependent

self-assembly properties and cytotoxicity using 2D cultures of normal and cancer cells. The MB could be potentially used as a candidate molecule for brain diseases treatment.

References

[1] J. A. DiMasi, L. Feldman, A. Seckler, A. Wilson, *Clinical Pharmacology & Therapeutics* **2010**, *87*, 272.
[2] M.-J. Blanco, K. M. Gardinier, *ACS Med. Chem. Lett.* **2020**, *11*, 228.
[3] M. Culot, S. Lundquist, D. Vanuxeem, S. Nion, C. Landry, Y. Delplace, M.-P. Dehouck, V. Berezowski, L. Fenart, R. Cecchelli, *Toxicology in Vitro* **2008**, *22*, 799.
[4] V. K. Gribkoff, L. K. Kaczmarek, *Neuropharmacology* **2017**, *120*, 11.
[5] M. E. Hardee, D. Zagzag, *Am J Pathol* **2012**, *181*, 1126.
[6] F. J. Rodriguez, B. A. Orr, K. L. Ligon, C. G. Eberhart, *Oncotarget* **2012**, *3*, 98.
[7] G. Nzou, R. T. Wicks, E. E. Wicks, S. A. Seale, C. H. Sane, A. Chen, S. V. Murphy, J. D. Jackson, A. J. Atala, *Scientific Reports* **2018**, *8*, 7413.
[8] A. Figarol, M. Matsusaki, in *Biomaterials for Organ and Tissue Regeneration*, Elsevier, **2020**, pp. 425–439.
[9] K. Taylor, L. R. Alvarez, *Altern Lab Anim* **2019**, *47*, 196.
[10] W. M. Pardridge, *Drug Discovery Today* **2007**, *12*, 54.
[11] W. G. Chang, L. E. Niklason, *npj Regenerative Medicine* **2017**, *2*, 1.
[12] A. D. Wong, M. Ye, A. F. Levy, J. D. Rothstein, D. E. Bergles, P. C. Searson, *Front Neuroeng* **2013**, *6*, DOI 10.3389/fneng.2013.00007.
[13] R. Cecchelli, B. Dehouck, L. Descamps, L. Fenart, V. Buée-Scherrer, C. Duhem, S. Lundquist, M. Rentfel, G. Torpier, M. P. Dehouck, *Advanced Drug Delivery Reviews* **1999**, *36*, 165.
[14] N. J. Abbott, A. A. K. Patabendige, D. E. M. Dolman, S. R. Yusof, D. J. Begley, *Neurobiology of Disease* **2010**, *37*, 13.
[15] B. W. Chow, C. Gu, *Trends in Neurosciences* **2015**, *38*, 598.
[16] S. M. Stamatovic, R. F. Keep, A. V. Andjelkovic, *Curr Neuropharmacol* **2008**, *6*, 179.
[17] W. M. Pardridge, *NeuroRx* **2005**, *2*, 3.
[18] W. A. Jefferies, M. R. Brandon, S. V. Hunt, A. F. Williams, K. C. Gatter, D. Y. Mason, *Nature* **1984**, *312*, 162.
[19] A. R. Jones, E. V. Shusta, *Pharm Res* **2007**, *24*, 1759.
[20] A. M. Giannetti, P. J. Halbrooks, A. B. Mason, T. M. Vogt, C. A. Enns, P. J. Björkman, *Structure* **2005**, *13*, 1613.
[21] H. Fuchs, R. Gessner, *Biochim Biophys Acta* **2002**, *1570*, 19.
[22] A. Calzolari, L. M. Larocca, S. Deaglio, V. Finisguerra, A. Boe, C. Raggi, L. Ricci-Vitani, F. Pierconti, F. Malavasi, R. De Maria, U. Testa, R. Pallini, *Transl Oncol* **2010**, *3*, 123.
[23] Z. Pang, H. Gao, Y. Yu, L. Guo, J. Chen, S. Pan, J. Ren, Z. Wen, X. Jiang, *Bioconjugate Chem.* **2011**, *22*, 1171.
[24] R. Prades, S. Guerrero, E. Araya, C. Molina, E. Salas, E. Zurita, J. Selva, G. Egea, C. López-Iglesias, M. Teixidó, M. J. Kogan, E. Giralt, *Biomaterials* **2012**, *33*, 7194.
[25] T. Kang, M. Jiang, D. Jiang, X. Feng, J. Yao, Q. Song, H. Chen, X. Gao, J. Chen, *Mol. Pharmaceutics* **2015**, *12*, 2947.
[26] K. Fan, X. Jia, M. Zhou, K. Wang, J. Conde, J. He, J. Tian, X. Yan, *ACS Nano* **2018**, *12*, 4105.
[27] S. Ruan, L. Qin, W. Xiao, C. Hu, Y. Zhou, R. Wang, X. Sun, W. Yu, Q. He, H. Gao, *Advanced Functional Materials* **2018**, *28*, 1802227.
[28] K. Hatherell, P.-O. Couraud, I. A. Romero, B. Weksler, G. J. Pilkington, *Journal of Neuroscience Methods* **2011**, *199*, 223.

[29] R. Ito, K. Umehara, S. Suzuki, K. Kitamura, K. Nunoya, Y. Yamaura, H. Imawaka, S. Izumi, N. Wakayama, T. Komori, N. Anzai, H. Akita, T. Furihata, *Mol. Pharmaceutics* **2019**, *16*, 4461.
[30] R. Cecchelli, S. Aday, E. Sevin, C. Almeida, M. Culot, L. Dehouck, C. Coisne, B. Engelhardt, M.-P. Dehouck, L. Ferreira, *PLOS ONE* **2014**, *9*, e99733.
[31] A. Appelt-Menzel, A. Cubukova, K. Günther, F. Edenhofer, J. Piontek, G. Krause, T. Stüber, H. Walles, W. Neuhaus, M. Metzger, *Stem Cell Reports* **2017**, *8*, 894.
[32] N. L. Stone, T. J. England, S. E. O'Sullivan, *Front. Cell. Neurosci.* **2019**, *13*, DOI 10.3389/fncel.2019.00230.
[33] S. Bang, S.-R. Lee, J. Ko, K. Son, D. Tahk, J. Ahn, C. Im, N. L. Jeon, *Scientific Reports* **2017**, *7*, 8083.
[34] C. Kulczar, K. E. Lubin, S. Lefebvre, D. W. Miller, G. T. Knipp, *Journal of Pharmacy and Pharmacology* **2017**, *69*, 1684.
[35] N. J. Abbott, L. Rönnbäck, E. Hansson, *Nature Reviews Neuroscience* **2006**, *7*, 41.
[36] D. D. Veiga, J. C. Antunes, R. G. Gómez, J. F. Mano, J. L. G. Ribelles, J. M. Soria, *J Biomater Appl* **2011**, *26*, 293.
[37] C. Barry, M. T. Schmitz, N. E. Propson, Z. Hou, J. Zhang, B. K. Nguyen, J. M. Bolin, P. Jiang, B. E. McIntosh, M. D. Probasco, S. Swanson, R. Stewart, J. A. Thomson, M. P. Schwartz, W. L. Murphy, *Exp Biol Med (Maywood)* **2017**, *242*, 1679.
[38] J. S. Ruano-Salguero, K. H. Lee, *Mol. Pharmaceutics* **2018**, *15*, 5081.
[39] G. N. Grifno, A. M. Farrell, R. M. Linville, D. Arevalo, J. H. Kim, L. Gu, P. C. Searson, *Scientific Reports* **2019**, *9*, 13957.
[40] E. De Jong, D. S. Williams, L. K. E. A. Abdelmohsen, J. C. M. Van Hest, I. S. Zuhorn, *Journal of Controlled Release* **2018**, *289*, 14.
[41] A. Figarol, Y. Naka, Y. Shigemoto-Mogami, T. Furihata, K. Sato, M. Matsusaki, *Biomed. Mater.* **2020**, DOI 10.1088/1748-605X/aba5f1.
[42] C. Praça, S. C. Rosa, E. Sevin, R. Cecchelli, M.-P. Dehouck, L. S. Ferreira, *Stem Cell Reports* **2019**, *13*, 599.
[43] G. Gao, J. H. Lee, J. Jang, D. H. Lee, J.-S. Kong, B. S. Kim, Y.-J. Choi, W. B. Jang, Y. J. Hong, S.-M. Kwon, D.-W. Cho, *Advanced Functional Materials* **2017**, *27*, 1700798.
[44] R. Patel, A. J. Alahmad, *Fluids and Barriers of the CNS* **2016**, *13*, 6.
[45] S. Feng, J. Cen, Y. Huang, H. Shen, L. Yao, Y. Wang, Z. Chen, *PLOS ONE* **2011**, *6*, e20599.
[46] M. P. Ferro, S. C. Heilshorn, R. M. Owens, *Materials Science and Engineering: R: Reports* **2020**, *140*, 100522.
[47] U. Novak, A. H. Kaye, *Journal of Clinical Neuroscience* **2000**, *7*, 280.
[48] B. J. Klotz, L. A. Oosterhoff, L. Utomo, K. S. Lim, Q. Vallmajo-Martin, H. Clevers, T. B. F. Woodfield, A. J. W. P. Rosenberg, J. Malda, M. Ehrbar, B. Spee, D. Gawlitta, *Advanced Healthcare Materials* **2019**, *8*, 1900979.
[49] D. Sood, K. Chwalek, E. Stuntz, D. Pouli, C. Du, M. Tang-Schomer, I. Georgakoudi, L. D. Black, D. L. Kaplan, *ACS Biomater. Sci. Eng.* **2016**, *2*, 131.
[50] H.-G. Yi, Y. H. Jeong, Y. Kim, Y.-J. Choi, H. E. Moon, S. H. Park, K. S. Kang, M. Bae, J. Jang, H. Youn, S. H. Paek, D.-W. Cho, *Nature Biomedical Engineering* **2019**, *3*, 509.
[51] L. Cucullo, M. Hossain, V. Puvenna, N. Marchi, D. Janigro, *BMC Neuroscience* **2011**, *12*, 40.
[52] L. Cucullo, M. Hossain, W. Tierney, D. Janigro, *BMC Neuroscience* **2013**, *14*, 18.
[53] G. D. Vatine, R. Barrile, M. J. Workman, S. Sances, B. K. Barriga, M. Rahnama, S. Barthakur, M. Kasendra, C. Lucchesi, J. Kerns, N. Wen, W. R. Spivia, Z. Chen, J. Van Eyk, C. N. Svendsen, *Cell Stem Cell* **2019**, *24*, 995.

[54] N. R. Wevers, D. G. Kasi, T. Gray, K. J. Wilschut, B. Smith, R. van Vught, F. Shimizu, Y. Sano, T. Kanda, G. Marsh, S. J. Trietsch, P. Vulto, H. L. Lanz, B. Obermeier, *Fluids and Barriers of the CNS* **2018**, *15*, 23.
[55] S. I. Ahn, Y. J. Sei, H.-J. Park, J. Kim, Y. Ryu, J. J. Choi, H.-J. Sung, T. J. MacDonald, A. I. Levey, Y. Kim, *Nature Communications* **2020**, *11*, 175.
[56] A. Herland, A. D. van der Meer, E. A. FitzGerald, T.-E. Park, J. J. F. Sleeboom, D. E. Ingber, *PLOS ONE* **2016**, *11*, e0150360.
[57] H. Duvernoy, S. Delon, J. L. Vannson, *Brain Research Bulletin* **1983**, *11*, 419.
[58] M. Campisi, Y. Shin, T. Osaki, C. Hajal, V. Chiono, R. D. Kamm, *Biomaterials* **2018**, *180*, 117.
[59] S. Lee, M. Chung, S.-R. Lee, N. L. Jeon, *Biotechnology and Bioengineering* **2020**, *117*, 748.

Chapter 1

Development of a three-dimensional blood-brain barrier network with opening capillary structures for drug transport screening assays

1.1. Introduction

As mentioned in the general introduction, assessing the functionality of TfR-mediated transport in 3D BBB models is highly desired, as it could create opportunities for the screening of novel treatments of central nervous system (CNS) diseases. The validation of a BBB model usually relies on the assessment of barrier integrity and functionality of specific transport systems. It can respectively be checked by measuring the permeability of the dextran or specific substrates. The size-permeability of different molecular weight of dextran is often investigated in most BBB models to demonstrate the low paracellular transport [1–3]. Only few studies however demonstrate the functionality of specific transporters such as the transferrin receptor (TfR) [4,5]. For example, Wevers *et al.* investigated the functionality of the TfR by comparing the transcytosis ability of the anti-TfR antibody MEM-189 and control antibody IgG1 [4], with only a two-fold difference was observed. The functionality of the TfR in this model may be not sufficient to distinguish "hit" compounds from other candidates when performing high-throughput screening by transport assays. Therefore, a 3D BBB model displaying higher discrimination of candidate molecules based on their TfR-mediated transport efficiency is expected to improve the sensitivity of the drug screening assays. To perform permeability assays, dextran or other tested compound require the capillaries to have an open end to perfuse molecules inside the capillary lumen. These techniques cannot however be performed in our previously reported 3D self-organized BBB capillary network model due to the absence of a perfusable connection between the outside and the capillary lumen [6,7]. Controlling the capillary organization and opening in our BBB model, as originally reported in 3D blood-/lymph-capillary networks [8], would thus be beneficial for drug transport assays.

In this chapter, a 3D self-organized *in vitro* model of the BBB with perfusable opening structures was established in a transwell culture. This fully human 3D BBB model recapitulates direct cell-cell interactions between BMEC, astrocytes and pericytes. The size-selective permeation of molecules, the functionality of transport systems by the capillary network, such as efflux pumps and TfR-mediated transcytosis were investigated.

1.2. Experiments

1.1.1. Cell maintenance

The three cell lines used in this study have been developed and characterized in previous studies: human brain microvascular endothelial cells/conditionally immortalized clone 18 (HBEC), human astrocyte/conditionally immortalized clone 35 (HA), and human brain pericyte/conditionally immortalized clone 37 (HP) were kindly provided by Prof. Furihata from the School of Pharmacy, Tokyo University of Pharmacy and Life Sciences (Hachioji, Tokyo, Japan). All cells were cultured on 100 mm diameter collagen type I coated dishes (Ref. 4020-010, Iwaki, Shizuoka, Japan) and incubated at 33 °C, 5% CO_2. All culture media were supplemented with 4 µg/mL Blasticidin S HCl (Ref. R21001, Invitrogen, Waltham, USA) to maintain selective pressure during routine culture. HBEC were cultured in Vasculife (Ref. LEC-LL0005, VEGF-Mv, LifeLine, Frederick, USA) supplemented with 0.5 mL rh FGF-b, 0.5 mL ascorbic acid, 0.5 mL hydrocortisone hemisuccinate, 25 mL l-glutamine, 0.5 mL rh IGF-1, 0.5 mL rh EGF, 0.5 mL rh VEGF, 0.5 mL heparin sulfate, 25 mL fetal bovine serum (FBS) (kit, LifeFactor VEGF-Mv, LifeLine, Frederick, USA), 25 mL supplementary FBS (Gibco ThermoFisher, Waltham, USA), and 1% penicillin-streptomycin (P/S, 10,000 U.mL-1 - 10,000 µg.mL-1, Nacalai tesque, Kyoto, Japan). HA were cultured in Dulbecco's Modified Eagle Medium (DMEM, Ref. 08458-16, Nacalai tesque, Kyoto, Japan), complemented with 10% FBS, 1% P/S, 5 mL of N_2 supplement x100 (Ref. 17502048, Gibco ThermoFisher, Waltham, USA). HP were cultured in Pericyte Medium (Ref. 1201, ScienCell Research Laboratories, Carlsbad, USA), supplemented by 1% Pericyte Growth Supplement 100x, 10% FBS, and 1% P/S. HA and HP were pre-differentiated at 37 °C during 3 days prior to their use for the fabrication of the 3D model BBB model.

1.1.2. Fabrication of 3D BBB with open structures

One the first day of preparation, a solution of 10%wt gelatin was prepared using gelatin powder (Ref G1890, Sigma Aldrich, St. Louis, MO, USA) dissolved in PBS. This solution was first placed in warm water bath to make it completely dissolved. 450 µL of 10%wt gelatin solution was dispensed on a 24-well plate (Ref. 3820-024, Iwaki, Shizuoka, Japan). The 24-well culture inserts with 0.4 µm pore size (Ref. 3470, Costar, NY, USA) were placed on the gelatin solution by taking precautions to avoid bubbles formation below the insert. The 24-well plate was then incubated at 4 °C for 20 min to enable the gelation of the gelatin solution. After

complete gelation, the inserts were taken out from the gelatin mold and the culture insert membranes was removed. The insert without membranes were plasma-treated with a small plasma device (Ref. PM100, Yamato Scientific Co., Ltd., Tokyo, Japan) with 40 sccm, 100 W for 1 min to make them hydrophilic. The plasma-treated inserts were placed back onto the gelatin mold in the 24-well plate. The HBEC, HA and HP were harvested with a Trypsin/ EDTA solution composed of 0.25% trypsin (Ref. 209-19182, Fujifilm Wako, Osaka, Japan) with 0.02% EDTA (Ref. E6758-500G, Sigma Aldrich, St. Louis, MO, USA) and centrifuged at 130 g for 3 min at room temperature. The cell pellet was resuspended in non-complemented DMEM and cell count was performed with the Countess™ 3 Automated Cell Counter (ThermoFisher, Waltham, USA). For the preparation of each 3D BBB gel, 2 mg of fibrinogen (Ref. F8630-5G, Sigma Aldrich, St. Louis, MO, USA) were dispersed in 40 µL of non-complemented DMEM in a Eppendorf tube, while 4 x 10^5 HA, 2 x 10^5 HBEC and 2 x 10^5 HP, and 0.2 U thrombin (Ref. T4648-10kU, Sigma Aldrich, St. Louis, MO, USA) were dispersed in 20 µL of non-complemented DMEM in another Eppendorf tube. The other BBB configurations were prepared in a similar manner but by omitting HP, HA and/or HBEC inside the fibrin gel when necessary. Both solutions were quickly mixed before depositing in cell culture inserts and incubated for 20 min at room temperature for fibrinogen gelation. The fibrins gels were then incubated an additional 40 min at 37 °C, 5% CO_2 to dissolve the gelatin gels. After complete dissolution of the gelatin gels, 500 µL of PBS was added into the bottom of the 24-well plates. The fibrin gels were placed in a new well with 2.5 mL of triple media composed of Vasculife medium, Pericyte medium, and DMEM/N_2 medium (1:1:1; v:v:v), all without Blasticidin, and incubated at 37 °C, 5% CO_2 overnight.

On the next day, the insert with fibrin gel was placed upside down in a 6-well plate (Ref. 3810-006, Iwaki, Shizuoka, Japan) filled with 10 mL of triple media. HBEC was harvested for a second seeding on the fibrin gel, with 2 x 10^5 HBEC resuspended in 60 µL of triple media on top of each fibrin gel. The gels were incubated at 37 °C, 5% CO_2 to enable the adhesion of HBEC onto the fibrin gel. After 6 h incubation, the inserts were placed on top of 6 well culture plates thanks to a specifically designed 24- to 6-well plate adaptor. 4 mL of triple media were additionally added and incubated at 37 °C & 5% CO_2. Half of the media (7 mL of total 14 mL) was changed every 3-4 days before the subsequent experiments performed after 7 days of culture.

1.1.3. Immunofluorescence staining

After 7 days culture, the 3D BBB models were rinsed three times in PBS then fixed in 4% paraformaldehyde (PFA, Fujifilm Wako, Osaka, Japan) at room temperature (RT) for 15 min. Permeabilization was carried out using 0.2% Triton X-100 diluted in PBS for 15 min (Sigma-Aldrich, St. Louis, MO, USA). After PBS rinsing, blocking was performed for 1 h at RT with 1% bovine serum albumin (BSA, Ref. A3294-50G, Sigma-Aldrich, St. Louis, MO, USA) in PBS. The samples were incubated with primary antibodies overnight at 4 °C: mouse anti- human CD31 antibody (Ref. NCL-CD31-1A10, Leica, Wetzlar, Germany), mouse anti-human ZO-1 antibody (Ref. ZO1-1A12, Invitrogen, Waltham, MA, USA, or mouse anti-human Claudin-5 antibody (Ref. 35-2500, Thermo Fisher Scientific, Waltham, MA, USA) diluted at 1/100 in 1% BSA in PBS. After PBS rinsing, samples were incubated for 2 h at room temperature in the dark with secondary antibody goat anti-mouse conjugated with Alexa Fluor 647 (Ref. A21235, Thermo Fisher Scientific, Waltham, MA, USA) diluted at 1/100 in 1% BSA in PBS. Actin filaments were stained with fluorescein isothiocyanate (FITC)-labeled phalloidin (Ref. ab235137, Abcam, Cambridge, UK). The nuclei were counterstained with Hoechst33342 (Ref. H3570, Thermo Fisher Scientific, Waltham, MA, USA). After washing three times with PBS, the samples were observed with confocal laser scanning microscope FluoView FV3000 (Olympus, Tokyo, Japan) using ×10 or ×40 magnification.

1.1.4. Calculation of $CD31^+$ surface area in the 3D BBB models

The whole insert was imaged by taking large scale pictures of the 3D BBB models stained for CD31 using confocal laser scanning microscope FluoView FV3000 (Olympus, Tokyo, Japan) using ×10 magnification. Three sections of the 3D BBB gel (bottom, middle and top of the fibrin gel) were separately imaged for three BBB gels issued from three independent experiments. The observation settings were kept the same for imaging the 3D BBB gels, such as the step size, the thickness of each observed section, the exposition time and excitation power. The $CD31^+$ surface area was automatically generated by IMARIS software for the three sections of the 3D BBB gels (Oxford Instruments, Abingdon, UK). The total $CD31^+$ surface area for each was obtained by summing the $CD31^+$ surface area of the three sections of the gel (bottom, middle and top of the fibrin gel).

1.1.5. Leakage assay with Fluorescein Isothiocyanate Labeled Dextran

The perfusability of the open structures was assessed by adding a solution of 1 mg/mL FITC-dextran MW 2000 kDa (Ref. FD2000S, Sigma Aldrich, St. Louis, MO, USA) diluted in PBS in the bottom side of the insert. After one hour incubation at room temperature, observation by confocal microscopy was performed by confocal laser scanning microscope FluoView FV3000 (Olympus, Tokyo, Japan) using x60 magnification. This experiment was conducted using fixed samples.

1.1.6. Evaluation of the Transendothelial Electrical Resistance

The transendothelial electrical resistance (TEER) was measured for the fibrin gel without BBB cells and for 3D BBB model with open structures after 7 days culture. The TEER was measured in PBS at RT using a Millicell® ERS-2 Volt-Ohm Meter (Millipore, Bedford, MA, USA) equipped with a STX01 chopstick electrode (Millipore, Bedford, MA, USA). The TEER value was calculated from the following equation (1) [9] :

(1) $TEER = (R_{BBB} - R_{only\ gel}) \times A$

Where $R_{only\ gel}$ is the resistance of the fibrin gel without BBB cells; R_{BBB} is the resistance of the fibrin gel seeded with BBB cells, and A is the average value of $CD31^+$ surface area of three 3D BBB gels calculated by IMARIS software.

1.1.7. Permeability assays

One day prior to the permeability assays, the wells of 24-well plate were pre-incubated with 1 mL of 1% BSA (Ref. A3294, Sigma Aldrich, St. Louis, MO, USA) in PBS overnight at 37 °C, 5% CO_2 to prevent unspecific adsorption of the tested molecules on the walls of the plate. All the permeability assays were performed on day 7 and day 8 of culture of the 3D BBB models at 37 °C, 5% CO_2 in triple media, using 1000 µL of triple media in the bottom side and 200 µL in the top side of the inserts.

For the assessment of paracellular transport, 4 kDa (Ref. T1037, Sigma Aldrich, St. Louis, MO, USA), 20 kDa (Ref. 73766, Sigma Aldrich, St. Louis, MO, USA) and 70 kDa (Ref. T1162, Sigma Aldrich, St. Louis, MO, USA) of tetramethylrhodamine (TRITC)-labeled dextran at a final concentration of 1 mg/mL or 10 µM Lucifer Yellow (CH, dilithium salt) (Ref. L0259, Sigma-Aldrich, St. Louis, MO, USA) were added to the bottom side before beginning

the assay. 10 µL of the culture media w!as collected in the top side of the insert at t = 1 h, 10 h, 24 h for the analysis.

For the evaluation of the functionality of P-glycoprotein (P-gp), the transport of Rhodamine 123 (Ref. R302, Thermo Fisher Scientific, Waltham, MA, USA) was measured for both the apical-to-basolateral side or basolateral-to-apical side. For that, 10 µM Rhodamine 123 dissolved in triple media was added in the bottom side (apical-to-basolateral transport) or top side (basolateral-to-apical transport) of the inserts containing the 3D BBB gels. Triple media was added in the top side (apical-to-basolateral transport) or bottom side (basolateral-to-apical transport) without the tested molecule. 10 µL of the culture media was collected in the top side (apical-to-basolateral transport) or the bottom side (basolateral-to-apical transport) of the insert at t = 1 h, 5 h, 10 h, 24 h for the analysis.

For the receptor-mediated transcytosis assay, 10 µg/mL Alexa Fluor 647-MEM-189 (AF 647-MEM-189, Ref. NB500-493AF647, NovusBio, Centennial, USA), Alexa Fluor 647-13E4 (AF 647-13E4, Ref. NB100-73092AF647, NovusBio, Centennial, USA) or Alexa Fluor 647-immunoglobulin G1 (AF 647-IgG1, Ref. NBP1-97005AF647, NovusBio, Centennial, USA) was added in the bottom side of the insert during 24 h. 10 µL of the culture media was collected in the top side of the insert at t = 1 h, 5 h, 10 h, 24 h for the analysis.

The fluorescent intensity of the tested molecules was evaluated using Nanodrop^{TM} fluorospectrometer (N3300, Thermo Fisher Scientific, Waltham, MA, USA) from which was deduced the amount of transported compound across the fibrin gel. The cumulative amount transported across the membrane was plotted against time, and the slopes of the linear regions were used to calculate the permeability coefficients, as previously reported [10]:

The effective permeability coefficient (P_e) of the 3D BBB gel was calculated using the following equation (2):

(2) $PS = (dQ/dt)/ (D_0 \times A)$

With PS, dQ/dt, and D_0 being respectively the permeability surface area product, the slope of the linear region of a plot of the amount of permeant in the receiver chamber over time, and the initial concentration of the tested molecule on the donor side.

(3) $1/PS_{total} = 1/PS_e + 1/PS_{only\ gel}$

(4) $P_e = PS_e/A$

With PS_{total} and $PS_{only\ gel}$ being respectively the permeability surface area product corresponding to the 3D fibrin gel seeded with and without the three types of BBB cells and PS_e is the surface area product value for the 3D BBB cells. A is the average value of $CD31^+$ surface area of the 3D BBB gels calculated by IMARIS software.

1.1.8. Statistical analysis

All values are presented as means ± standard deviation (SD). Statistical analysis of the data was performed with Student's *t*-test or One-way *ANOVA* using EzAnova software (Version 0.985, University of South Carolina, Columbia, SC, USA) when more than two samples were compared with Tukey multiple comparison post-hoc tests. Differences were considered statistically significant when $p < 0.05$.

1.3. Results and discussion

1.3.1. Fabrication of a three-dimensional brain microvasculature network model with open structures

A 3D model of the 3D BBB microvascular network was established as illustrated in **Figure 1-1**. Briefly, the HBEC, HA and HP mixture was dispersed in the culture medium containing thrombin. The cell suspension was mixed with fibrinogen and quickly deposited in the 24-well insert before the formation of the fibrin gel. The ratio of each cell type incorporated in the fibrin gel was already established and optimized in a previous report [7]. Based on network appreciation by confocal observations and capillary diameter and length measurements, the best results were obtained for ratios of 1:2:0.5 HBEC:HA:HP. The selected cell ratio was in a similar order of magnitude than those observed *in vivo*, such as 1:5:1 HBEC:HA:HP [11] or 1:0.3 HBEC:HP [12]. The next day, a HBEC monolayer was deposited onto the bottom side of the membrane-free insert of the fibrin gel.

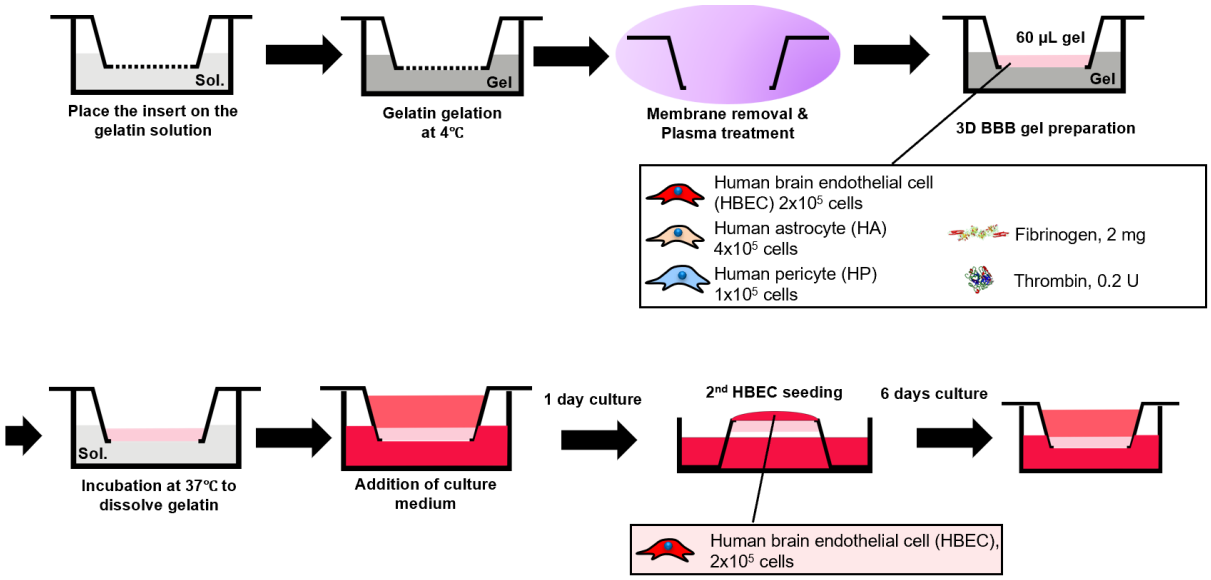

Figure 1-1. Schematic illustration of the fabrication method of the 3D BBB model with open structures by gelatin method.

The expected mechanism of the formation of the open structures is detailed in **Figure 1-2**. After 7 days culture, the HBEC monolayer and the HBEC inside the fibrin gel fused to generate a vascular network by self-organization with lumen structures, as similarly shown in our previous works [7,13].

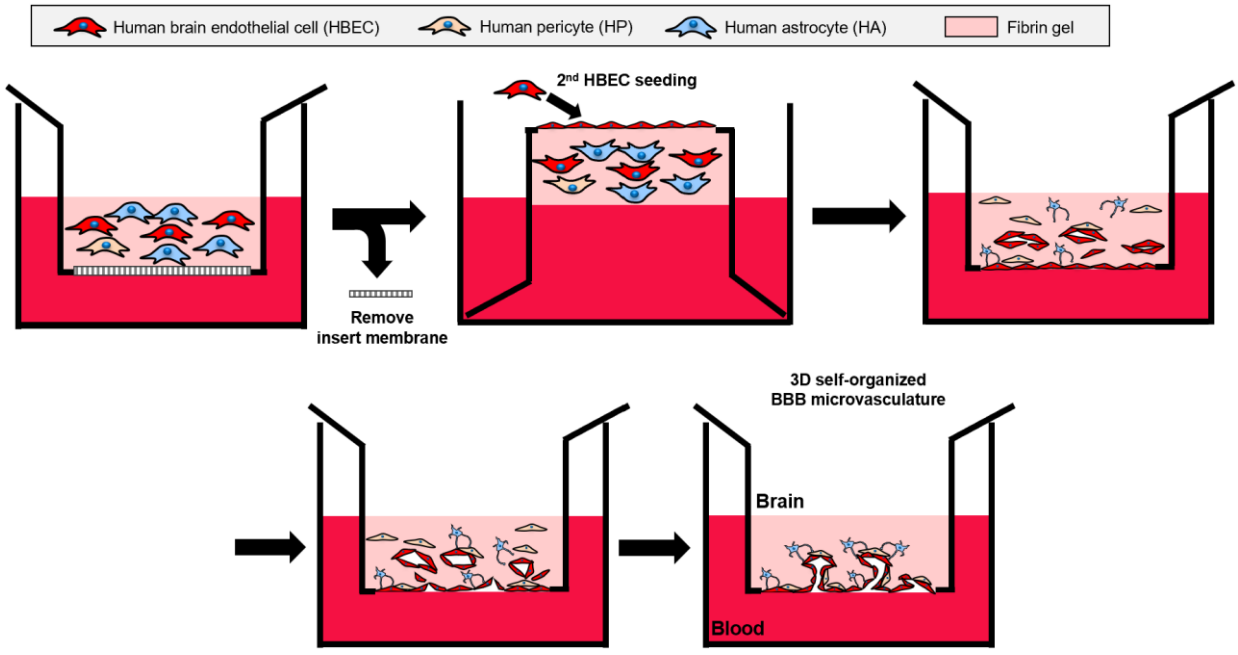

Figure 1-2. Schematic illustration of the expected formation of the open structures in the 3D BBB model.

Several holes, named open structures, were uniformly distributed in the entire bottom surface of the fibrin gel (**Figure 1-3A**). The confocal xz and yz planes showed a clear organization of the HBEC as capillary-like tubules with open lumen (**Figure 1-3B**). Moreover, the actin and CD31 staining showed the direct cell-cell contact between HBEC, HP and HA. This observation is consistent with previous studies which demonstrated HA and HP were found in the close vicinity of the HBEC network [6,7]. The open structures could be successfully perfused by 2000 kDa dextran (**Figure 1-3C**). These data suggested the successful formation of open structures composed of BBB microvascular network.

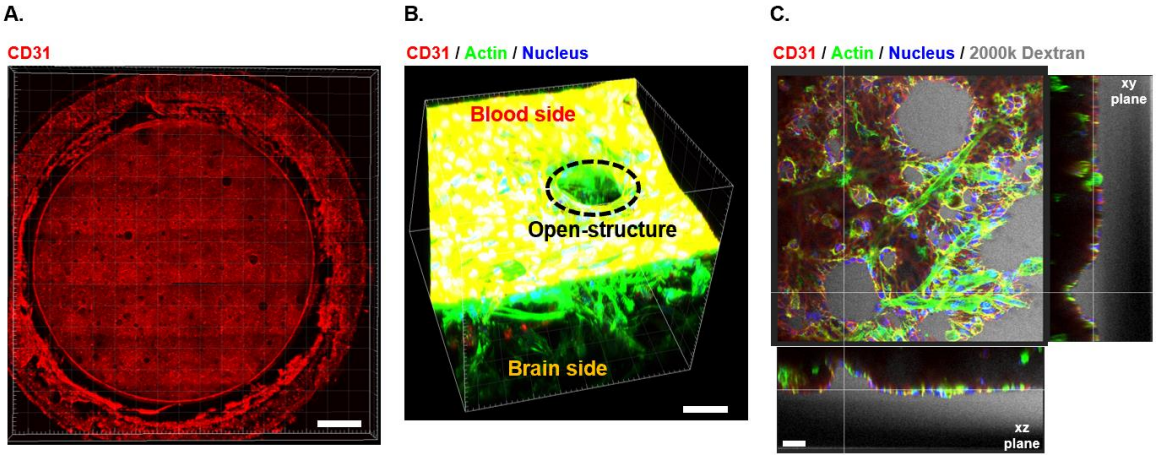

Figure 1-3. (A) Confocal image of the bottom side of the whole culture insert after 7 days culture showing the open structures. Scale bar = 1 mm. (B) 3D reconstruction of a confocal z-stack showing the open structures. HBEC were labeled with CD31 (red), all cells were stained for actin filaments (green) and nucleus (blue). Scale bar = 80 μm. (C) Cross-sectional image of the open structure perfused with FITC-labeled dextran (MW 2000 kDa) (grey). Scale bar = 50 μm.

1.3.2. Optimization of self-assembled microvasculature with open structures

We next wanted to understand whether there would be one specific cell type which could more contribute for stimulating the formation of the open structures in our model. As seen in **Figure 1-4A**, different combinations of the three BBB cell types were envisaged, with (i) only a monolayer of HBEC on the bottom of the insert ("HBEC mono"), or in combination with (ii) HP ("HBEC mono + HP"), (iii) HA ("HBEC mono + HA"), or (iv) both HP and HA ("HBEC mono + HP + HA"), or (v) HA, HP and HBEC ("HBEC mono + HP + HA + HBEC") inside the fibrin gel. Open structures were not formed with "HBEC mono" conditions but were present in "HBEC mono + HP", "HBEC mono + HA", "HBEC mono + HP + HA", and "HBEC mono + HP + HA + HBEC" conditions, with a respective number of open structures of 53 ± 6, 131 ±

8, 223 ± 20 and 301 ± 28. Only a few open structures were observed in “HBEC mono + HP” condition. The addition of HBEC inside the gel enabled the stabilization of a more developed vasculature with more open structures found in “HBEC mono + HP + HA + HBEC”. Fewer open structures were found in “HBEC mono + HA” condition than with “HBEC mono + HP + HA + HBEC” (**Figure 1-4B)**. Open structures were more numerous on the bottom of the gel for “HBEC mono + HA” than for “HBEC mono + HP” condition. These results suggest HA could be more necessary than HP to promote the formation of the open structures in the fibrin gel. This observation is consistent with previous report which also emphasizes the role of astrocytes in the improved morphology of the vascular network [3]. Astrocytes have indeed a major role in the development and maintenance of BBB features in BMEC. They can secrete several growth factors, such as vascular endothelial growth factor (VEGF), basic fibroblast growth factor (bFGF), glial cell line-derived neurotrophic factor (GDNF), or angiopoietin 1 (ANG-1), which can stimulate vasculogenesis, the expression of tight junctions and enzymatic systems and promote the polarization of transporters in HBEC [14,15]. The diameter of these open structures, when present, was in a similar range, independently of the cell combination inside the fibrin gels (**Figure 1-4B**). The formation of open structures is expected to result from the combination of biochemical and physical effects that promotes *in vitro* vascularization in engineered 3D-microenvironments. The HBEC are indeed able to migrate in a 3D environment, mainly towards the tissue surface, through angiogenic processes under the conditions that large amounts of angiogenic factors (e.g. VEGF) are secreted by neighboring supporting cells [16]. This method enables the 3D arrangement of HBEC that allows their encounter and connection with each other inside the fibrin gel and with those seeded on the bottom of the hydrogel in order to spontaneously form the HBEC capillary network with open structures. Based on the structural evaluation of the vascular network and the highest number of open structures, “HBEC mono + HP + HA + HBEC” was considered as the best combination after 7 days culture and was thus used for the subsequent experiments.

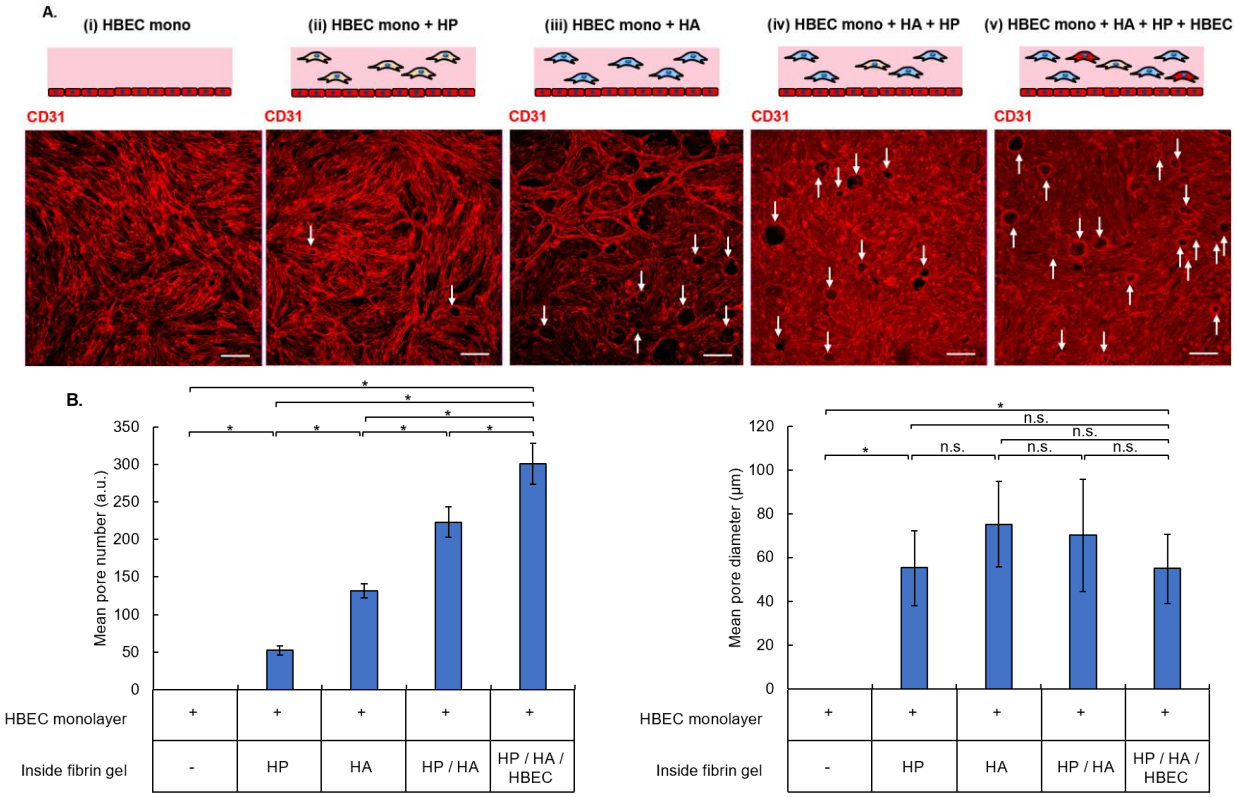

Figure 1-4. (A) Comparison of different types of BBB model with the HBEC monolayer seeded on the bottom of the fibrin gel (HBEC mono), with the HBEC monolayer seeded on the bottom of the fibrin gel and only HP (HBEC mono + HP) or only HA (HBEC mono + HA) or both HP and HA inside the fibrin gel (HBEC mono + HA +HP), or with the HBEC monolayer seeded on the bottom of the fibrin gel and HBEC, and HBEC, HP and HA inside the fibrin gel (HBEC mono + HA + HP + HBEC). Confocal images of the bottom side of the culture insert after 7 days culture for the different types of BBB model, HBEC were stained by the endothelial cell marker CD31 (red). White arrows indicate the open structures. Scale bar = 150 µm. (B) Quantification of number (left) and average diameter (right) of open structures on the bottom side of the whole culture insert after 7 days culture for the different types of BBB model (n=3 gels/condition). The average diameter was determined using 25 open structures per gel were used. Data are presented as means ± S.D.

1.3.3. Evaluation of the barrier function properties

The BBB is characterized by its reduced paracellular transport, with 100% of the large molecules and 98% of small molecules which cannot penetrate the brain [17]. Even the movement of small ions such as Na^+ and Cl^- is also restricted, resulting in a high

transendothelial electrical resistance (TEER) that reach more than 1,000 Ω x cm^2 [18,19]. We thus sought to investigate if our model could reproduce this reduced paracellular transport *in vitro*.

First, the permeability of TRITC-dextran with different molecular weights (4, 20 or 70 kDa) was evaluated in the 3D BBB model with open structures. As seen in **Figure 1-5A**, the permeability of TRITC-dextran gradually decreased with increased molecular weight, resulting from the different size of tested molecules transported across the 3D BBB model with open structures. The effective permeability coefficient value (P_e) value of 4 kDa, 20 kDa, and 70 kDa TRITC-labeled dextran were respectively 2.14 x 10^{-6}, 6.34 x 10^{-7}, and 4.76 x 10^{-8} cm/s. The P_e values of the dextran correlated with the previously reported *in vivo* rodent brain uptake (R^2 = 0.973) (**Figure 1-5B**) [20]. It should also be noted that our model showed a better correlation with *in vivo* values than those previously reported using iPSC-based BBB-Chip model (R^2 = 0.96) [1].

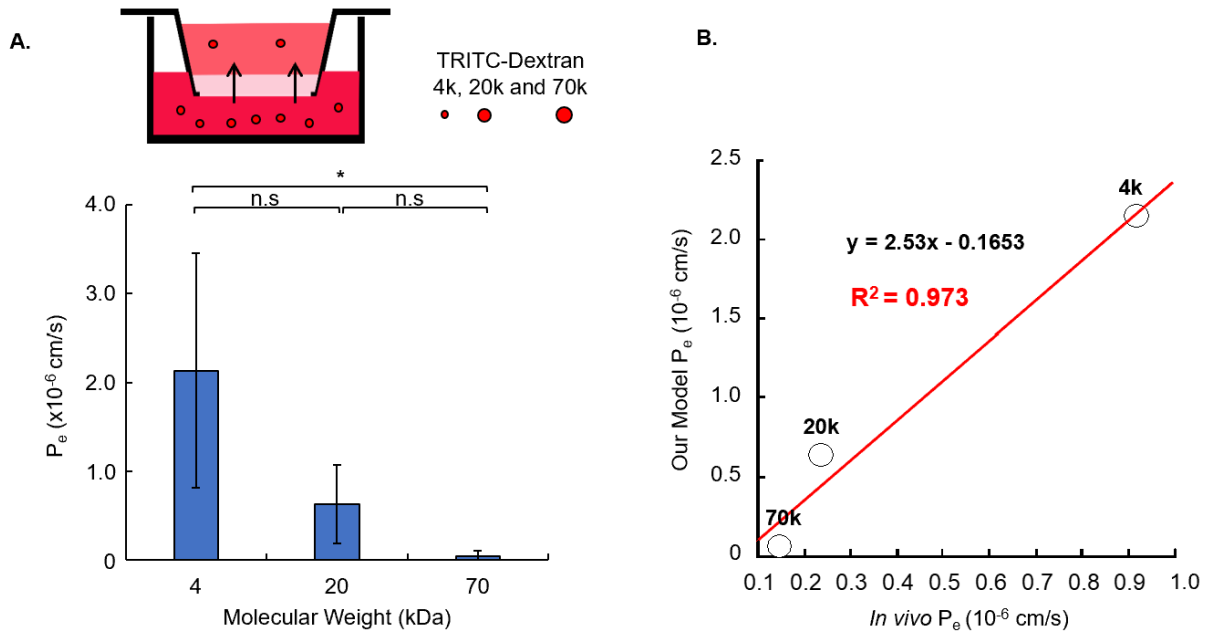

Figure 1-5. (A) P_e values of 1 mg/mL TRITC-dextran with different molecular weights (4 kDa, 20 kDa, and 70 kDa) (n=3). Data are presented as means ± S.D. (B) The permeability of dextran molecules across the 3D BBB model with open structures correlated with previously reported *in vivo* rodent brain uptake (R^2 = 0.973) [20].

The TEER value measured in our 3D model was about 560 Ω x cm^2, which is higher than the acellular fibrin gel which has a TEER of about 51 Ω x cm^2 (**Figure 1-6A**), but being much lower than the value found *in vivo*. Additionally, the paracellular tracer Lucifer Yellow showed a P_e value of 4.17 x 10^{-6} cm/s respectively (**Figure 1-6B**). The P_e value of Lucifer Yellow is higher than the *in vivo* permeability values measured in pial post-capillary venules in

a rodent model, reported to be around 1-2 x 10^{-7} cm/s [21]. It suggests our model showed some limitations to restrict the permeation of small-sized molecules, such as Lucifer Yellow which has a MW of 457 Da.

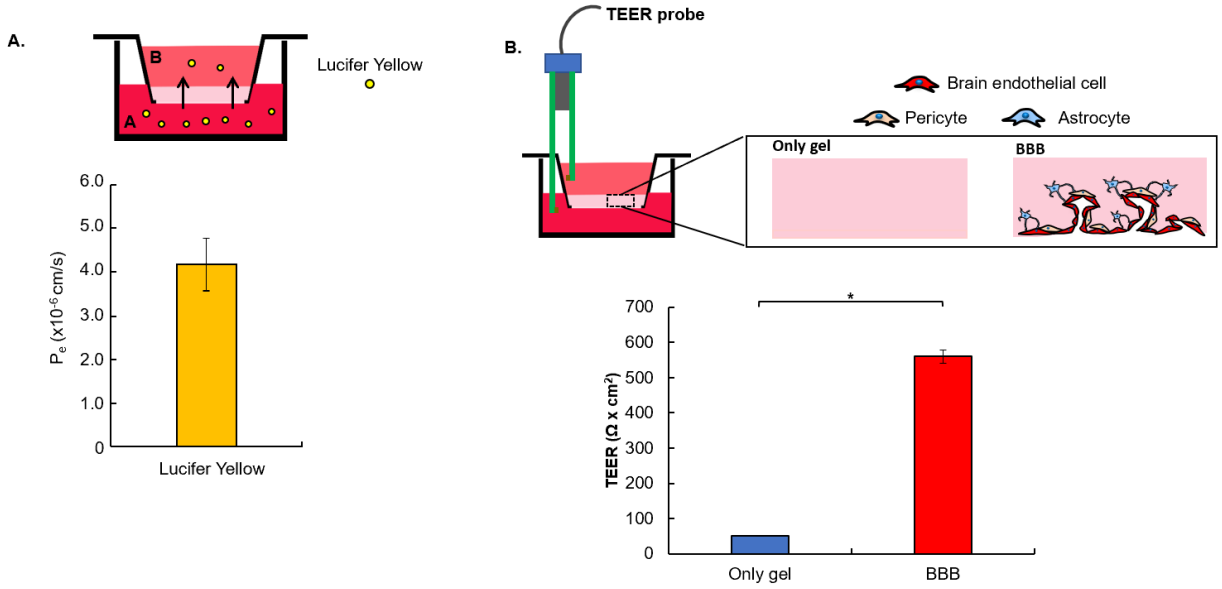

Figure 1-6. (A) P_e value of 10 µM Lucifer Yellow after 24 h incubation at 37 °C (n=3). Data are presented as means ± S.D. (B) TEER measurement (n=3). Data are presented as means ± S.D.

The expression of tight junctions (TJs) is known to have an important role in the regulation of the diffusion of molecules across the brain endothelium [22]. Claudin 5 is one of the dominant TJ proteins in the brain endothelium and is thought to play a major role in the macromolecular assembly of the TJs [23]. Zonula occludens-1 (ZO-1) is also involved in the maintenance of the TJs stability and functionality by serving as a linker molecule between the TJ components and the actin cytoskeleton [24–26]. Both ZO-1 and Claudin-5 were expressed by HBEC after 7 days culture both inside and in the bottom of the hydrogel (**Figure 1-7**). The high expression of the TJs could be partially responsible for the size-selective permeation of dextran. Taken together, these results demonstrate that our model could be useful to predict the brain penetrability of candidate molecules due to the formation and maintenance of a restrictive barrier sufficient for enabling the size-selective transport of different MW of dextran. This model however failed to restrict the passage of small-sized molecules, as shown by the low TEER value and moderate permeation of the Lucifer Yellow.

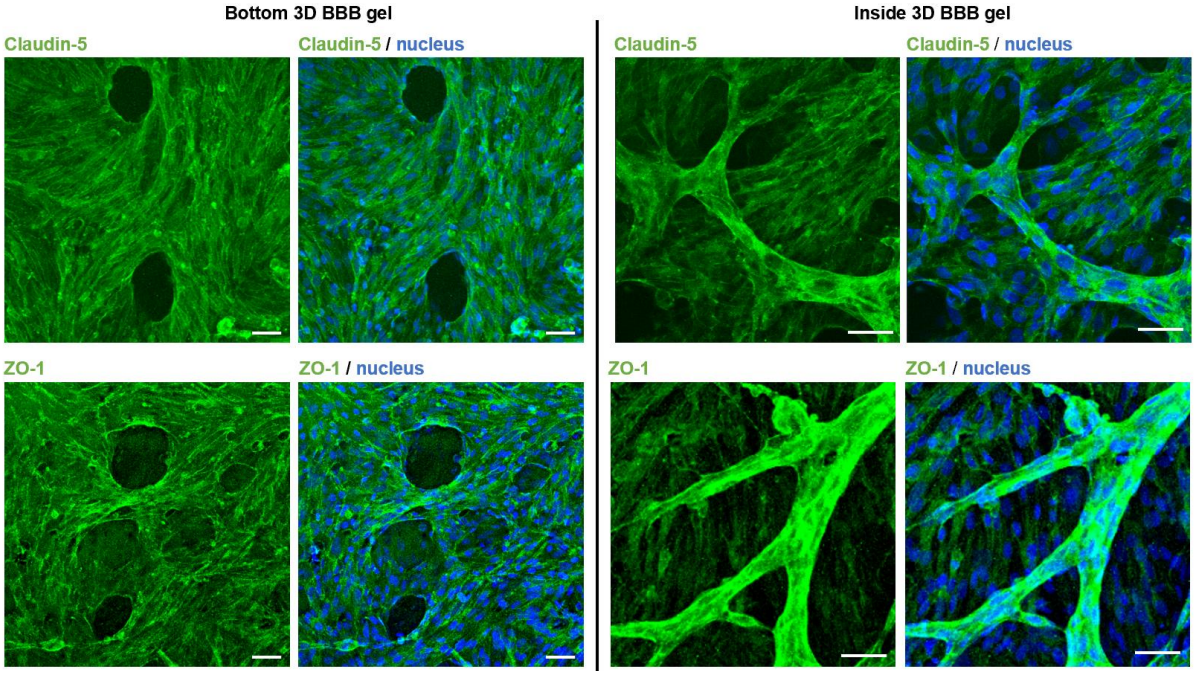

Figure 1-7. Immunofluorescence staining of the TJs, Claudin-5 (green, top) or ZO-1 (green, bottom) and cell nuclei (blue) in the bottom and inside the 3D BBB model with open structures after 7 days culture. Scale bar = 50 µm.

1.3.4. Evaluation of efflux pump activity

The presence of specific transport systems on the membranes of BMEC contributes to the regulation of the passage of molecules across the BBB, preventing potentially harmful compounds from entering in the brain and effluxing brain metabolic wastes [14]. Efflux transporters localized on the luminal surface of BMEC enable the clearance of potentially harmful xenobiotics from the brain and limit the access of toxic agents to the brain [27]. P-glycoprotein (P-gp) is one of the most studied efflux pumps responsible for rejection of a wide range of chemical compounds, including central nervous system drugs [28]. Although the expression of P-gp by HBEC at both gene and protein levels was confirmed in 3D model in a previous study [6], its functionality was yet to be investigated. Since transporter expression is indeed not necessarily correlated with its activity [29], it was primordial to confirm the functionality of the efflux pump in our model. For that, both apical-to-basolateral (A to B) and basolateral-to-apical (B to A) permeability of Rhodamine 123, a specific substrate of P-gp [30], was measured. As seen in **Figure 1-8**, the P_e value of Rhodamine 123 from A to B compartment and from B to A compartment was respectively 1.95 x 10^{-6} and 1.91 x 10^{-5} cm/s. The efflux

ratio, defined as $P_{e(B\ to\ A)}/P_{e(A\ to\ B)}$, is about 9.7, demonstrating the high polarization of the P-gp, with a higher expression on the apical side, which is similar to *in vivo* situation [31,32].

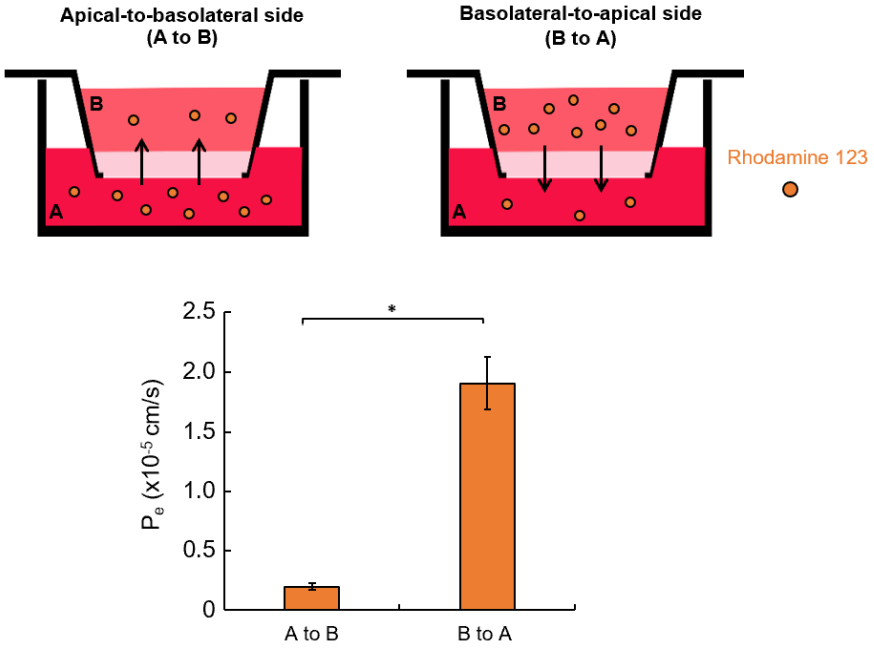

Figure 1-8. Comparison of the P_e value of 10 µM Rhodamine 123 from apical-to-basolateral side (A to B) and basolateral-to-apical side (B to A) after 24 h incubation at 37 °C (n=3). Data are presented as means ± S.D.

1.3.5. Assessment of transferrin receptor-mediated transcytosis

The transferrin receptor (TfR) is known to mediate the transport of iron-bound transferrin (Tf). TfR has recently attracted increasing attention due to its high expression by both brain BMEC and brain cancer cells, which could be useful for the specific transport of large-sized drugs across the BBB and to the cancer site [33–35].

We sought to confirm whether the combination "HBEC mono + HP + HA + HBEC" showed the highest TfR-mediated transport efficiency as compared to "HBEC mono" and "HBEC mono + HP + HA" conditions. For that, the permeability of AF 647-MEM-189 and the mouse Alexa Fluor 647-Immunoglobulin G1 isotype control (AF 647-IgG1), which does not bind any target on human cells, were compared for each model configuration **(Figure 1-9)**. The P_e value of AF 647-MEM-189 was 4.06 x 10^{-6} cm/s for "HBEC mono + HP + HA + HBEC", which is higher than that of "HBEC mono" and "HBEC mono + HP + HA" conditions, which have a respective P_e value of 7.96 x 10^{-7} and 9.54 x 10^{-7} cm/s. AF 647-IgG1 showed comparable low permeability for all the configurations, with a respective P_e value of 4.07 x 10^{-7}, 5.22 x 10^{-7} and 6.83 x 10^{-7} cm/s for "HBEC mono" "HBEC mono + HP + HA" and "HBEC mono + HP + HA + HBEC" conditions, suggesting similar maintained barrier function properties among

the different models. Although the number of open structures was the highest in "HBEC mono + HP + HA + HBEC" condition as compared to the "HBEC mono" "HBEC mono + HP + HA" conditions (**Figure 1-4B**), it did not significantly affect the permeability of AF 647-IgG1, suggesting the barrier function and paracellular transport efficiency of the antibodies are comparable among the different BBB models. These results suggest "HBEC mono + HP + HA + HBEC" displayed the highest TfR functionality, due to the higher transport of AF 647-MEM-189 as compared to the negative control AF 647-IgG1. The observed differences of permeability between AF 647-IgG1 and AF 647-MEM-189 did not depend on the number of open structures or differences in barrier function, but resulted from the higher TfR-mediated transport in "HBEC mono + HP + HA + HBEC" condition.

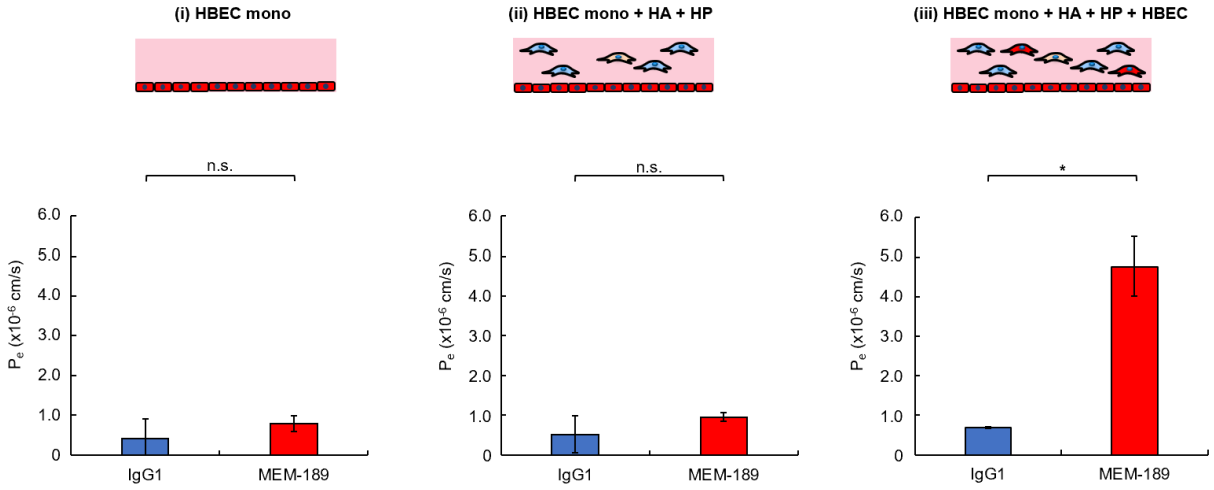

Figure 1-9. P_e values of 10 µg/mL AF 647-MEM-189 or AF 647-IgG1 using different 3D BBB models after 24 h incubation at 37 °C (n=3). Data are presented as means ± S.D.

In order to further characterize the permeation of TfR ligands in the "HBEC mono + HP + HA + HBEC" condition, we next compared the permeability of AF 647-MEM-189 with another human anti-TfR antibody Alexa Fluor 647-labeled 13E4 (AF 647-13E4), reported to have a reduced transportability [5,36]. A similar trend was found for the P_e values, with 4.77 x 10^{-6} cm/s for AF 647-MEM-189, which was seven-fold higher than that of AF 647-IgG1 and AF 647-13E4 which are respectively 6.83 x 10^{-7} and 6.12 x 10^{-7} cm/s (**Figure 1-10A**). It is worth mentioning that our model displayed a better capacity to discriminate antibodies based on their TfR-mediated permeation than the OrganoPlate©, where only a two-fold difference was observed between the permeability of MEM-189 and IgG1 [4]. The expected mechanism of permeation of the antibodies is detailed in **Figure 1-10B.** 13E4 is reported to have a reduced transportability as a consequence of its high affinity to the TfR. The binding affinity to the TfR has been indeed already reported to determine the transportability of antibodies directed against

the TfR, including MEM-189 and 13E4 [36]. Due to its high affinity to the TfR, 13E4 is degraded inside the cells, thus is not transported across the HBEC network in the 3D BBB model. Conversely, since MEM-189 have a moderate affinity to the TfR, it can be efficiently transported by the TfR. Moreover, AF 647-MEM-189, AF 647-13E4 and AF 647-IgG1 have a similar MW (~156 kDa), thus sharing the same contribution of the paracellular transport in the overall permeability. The permeation rate of AF 647-MEM-189 was however much higher than of AF 647-13E4 and AF 647-IgG1 in "HBEC mono + HP + HA + HBEC" condition (**Figure 1-10B**), confirming that MEM-189 was mainly transported by TfR-mediated transcytosis. Taken together, these results demonstrated our 3D BBB model with open structures could be useful for the study and the screening of molecules based on the TfR-mediated transport efficiency.

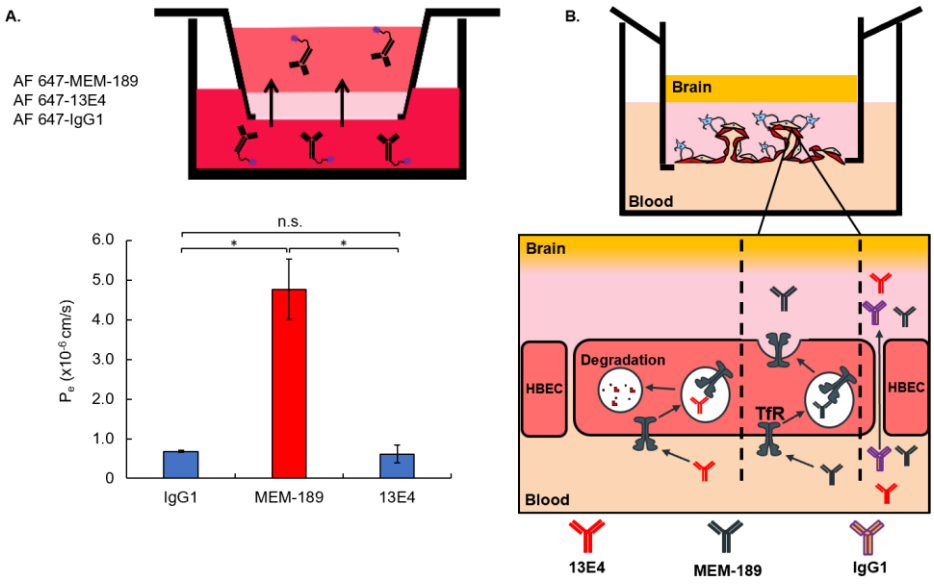

Figure 1-10. (A) P_e values of 10 µg/mL AF 647-MEM-189, AF 647-13E4 or AF 647-IgG1 using 3D BBB model with open structures after 24 h incubation at 37 °C (n=3). Data are presented as means ± S.D. (B) Expected mechanism of the permeation of AF 647-MEM-189, AF 647-13E4 or AF 647-IgG1 in the 3D BBB model with open structures.

1.4. Conclusion

In this study, we successfully developed a 3D self-organized capillary network composed of endothelial cells, astrocytes and pericytes with perfusable opening ends. After 7 days culture, the obtained vascular network exhibited lumen which diameter was similar to the native BBB capillaries and also showed a few larger similar to microvessels and venules. Additionally, many BBB features could be retrieved in this model, including functional P-gp efflux system and specific transporters, such as the TfR. Although the permeability of different

MW of dextran showed good correlation with *in vivo* permeability in rodent brain, it however displayed an insufficient barrier function as shown by the lower TEER value and permeability of the paracellular tracer Lucifer Yellow by the HBEC capillary network. The resulting paracellular transport may not be suitable for the accurate assessment of the permeation of both small-sized molecules, including small drugs, and large-sized molecules with a MW < 70 kDa. Changing cell source of BMEC could potentially improve barrier function properties for the preparation of a more biologically relevant 3D BBB model.

1.5. References

[1] G. D. Vatine, R. Barrile, M. J. Workman, S. Sances, B. K. Barriga, M. Rahnama, S. Barthakur, M. Kasendra, C. Lucchesi, J. Kerns, N. Wen, W. R. Spivia, Z. Chen, J. Van Eyk, C. N. Svendsen, *Cell Stem Cell* **2019**, *24*, 995.

[2] S. I. Ahn, Y. J. Sei, H.-J. Park, J. Kim, Y. Ryu, J. J. Choi, H.-J. Sung, T. J. MacDonald, A. I. Levey, Y. Kim, *Nature Communications* **2020**, *11*, 175.

[3] M. Campisi, Y. Shin, T. Osaki, C. Hajal, V. Chiono, R. D. Kamm, *Biomaterials* **2018**, *180*, 117.

[4] N. R. Wevers, D. G. Kasi, T. Gray, K. J. Wilschut, B. Smith, R. van Vught, F. Shimizu, Y. Sano, T. Kanda, G. Marsh, S. J. Trietsch, P. Vulto, H. L. Lanz, B. Obermeier, *Fluids and Barriers of the CNS* **2018**, *15*, 23.

[5] T.-E. Park, N. Mustafaoglu, A. Herland, R. Hasselkus, R. Mannix, E. A. FitzGerald, R. Prantil-Baun, A. Watters, O. Henry, M. Benz, H. Sanchez, H. J. McCrea, L. C. Goumnerova, H. W. Song, S. P. Palecek, E. Shusta, D. E. Ingber, *Nature Communications* **2019**, *10*, 2621.

[6] A. Figarol, Y. Naka, Y. Shigemoto-Mogami, T. Furihata, K. Sato, M. Matsusaki, *Biomed. Mater.* **2020**, DOI 10.1088/1748-605X/aba5f1.

[7] A. Figarol, M. Piantino, T. Furihata, T. Satoh, S. Sugiura, T. Kanamori, M. Matsusaki, *Biochemical and Biophysical Research Communications* **2020**, *533*, 600.

[8] D. Hikimoto, A. Nishiguchi, M. Matsusaki, M. Akashi, *Advanced Healthcare Materials* **2016**, *5*, 1969.

[9] B. Srinivasan, A. R. Kolli, M. B. Esch, H. E. Abaci, M. L. Shuler, J. J. Hickman, *J Lab Autom* **2015**, *20*, 107.

[10] T. Kurosawa, Y. Tega, K. Higuchi, T. Yamaguchi, T. Nakakura, T. Mochizuki, H. Kusuhara, K. Kawabata, Y. Deguchi, *Mol. Pharmaceutics* **2018**, *15*, 5546.

[11] W. M. Pardridge, *J Neurovirol* **1999**, *5*, 556.

[12] D. Shepro, N. M. L. Morel, *The FASEB Journal* **1993**, *7*, 1031.

[13] A. Nishiguchi, M. Matsusaki, M. R. Kano, H. Nishihara, D. Okano, Y. Asano, H. Shimoda, S. Kishimoto, S. Iwai, M. Akashi, *Biomaterials* **2018**, *179*, 144.

[14] N. J. Abbott, L. Rönnbäck, E. Hansson, *Nature Reviews Neuroscience* **2006**, *7*, 41.

[15] R. Cabezas, M. Ávila, J. Gonzalez, R. S. El-Bachá, E. Báez, L. M. García-Segura, J. C. Jurado Coronel, F. Capani, G. P. Cardona-Gomez, G. E. Barreto, *Front Cell Neurosci* **2014**, *8*, 211.

[16] A. Nishiguchi, M. Matsusaki, Y. Asano, H. Shimoda, M. Akashi, *Biomaterials* **2014**, *35*, 4739.

[17] W. M. Pardridge, *NeuroRx* **2005**, *2*, 3.

[18] A. M. Butt, H. C. Jones, N. J. Abbott, *The Journal of Physiology* **1990**, *429*, 47.

[19] C. Crone, S. P. Olesen, *Brain Research* **1982**, *241*, 49.

[20] W. Yuan, Y. Lv, M. Zeng, B. M. Fu, *Microvascular Research* **2009**, *77*, 166.
[21] A. S. Easton, M. H. Sarker, P. A. Fraser, *The Journal of Physiology* **1997**, *503*, 613.
[22] A. Reichel, D. J. Begley, N. J. Abbott, in *The Blood-Brain Barrier: Biology and Research Protocols* (Ed: S. Nag), Humana Press, Totowa, NJ, **2003**, pp. 307–324.
[23] K. J. Hewitt, R. Agarwal, P. J. Morin, *BMC Cancer* **2006**, *6*, 186.
[24] A. S. Fanning, B. J. Jameson, L. A. Jesaitis, J. M. Anderson, *Journal of Biological Chemistry* **1998**, *273*, 29745.
[25] K. Umeda, J. Ikenouchi, S. Katahira-Tayama, K. Furuse, H. Sasaki, M. Nakayama, T. Matsui, S. Tsukita, M. Furuse, S. Tsukita, *Cell* **2006**, *126*, 741.
[26] C. M. Van Itallie, A. S. Fanning, J. Holmes, J. M. Anderson, *Journal of Cell Science* **2010**, *123*, 2844.
[27] S. Seetharaman, M. A. Barrand, L. Maskell, R. J. Scheper, *Journal of Neurochemistry* **1998**, *70*, 1151.
[28] S. Dauchy, F. Dutheil, R. J. Weaver, F. Chassoux, C. Daumas-Duport, P.-O. Couraud, J.-M. Scherrmann, I. De Waziers, X. Declèves, *Journal of Neurochemistry* **2008**, *107*, 1518.
[29] L. Lescale-Matys, J. Dyer, D. Scott, T. C. Freeman, E. M. Wright, S. P. Shirazi-Beechey, *Biochemical Journal* **1993**, *291*, 435.
[30] M. Fontaine, W. F. Elmquist, D. W. Miller, *Life Sciences* **1996**, *59*, 1521.
[31] W. Löscher, H. Potschka, *NeuroRX* **2005**, *2*, 86.
[32] H. Sun, H. Dai, N. Shaik, W. F. Elmquist, *Advanced Drug Delivery Reviews* **2003**, *55*, 83.
[33] A. Calzolari, L. M. Larocca, S. Deaglio, V. Finisguerra, A. Boe, C. Raggi, L. Ricci-Vitani, F. Pierconti, F. Malavasi, R. De Maria, U. Testa, R. Pallini, *Transl Oncol* **2010**, *3*, 123.
[34] Z. M. Qian, H. Li, H. Sun, K. Ho, *Pharmacol Rev* **2002**, *54*, 561.
[35] K. B. Johnsen, A. Burkhart, L. B. Thomsen, T. L. Andresen, T. Moos, *Progress in Neurobiology* **2019**, *181*, 101665.
[36] H. Sade, C. Baumgartner, A. Hugenmatter, E. Moessner, P.-O. Freskgård, J. Niewoehner, *PLOS ONE* **2014**, *9*, e96340.

Chapter 2

Brain microvascular endothelial cells derived from human induced pluripotent stem cells as *in vitro* model for assessing blood-brain barrier transferrin receptor-mediated transcytosis

2.1. Introduction

As aforementioned, HBEC used in the 3D BBB model with open capillary network were found to exhibit inadequate barrier function properties for transport assay applications. The source of BMEC is an important factor to consider for the reproduction of the BBB properties *in vitro*, including the restricted paracellular transport. Although immortalized cell lines provide a readily available source of human brain microvascular endothelial cells (BMEC), they do not exhibit some of the characteristics of the *in vivo* BBB endothelium, being impaired by their inadequate barrier function and low expression of BBB-specific transporters and enzymes [1,2]. Human induced pluripotent stem cells derived BMEC-like cells (hiPS-BMEC) have recently generated great opportunities for the BBB modelling by exhibiting a paracellular tightness similar to the native BBB.[3] Although the formation of strong TJs and the expression of some transporter proteins were demonstrated for hiPS-BMEC, the functions of the receptor-mediated transcytosis (RMT) receptors remain to be elucidated, particularly the TfR-mediated transcytosis. Various drug delivery systems (DDS) have been designed for improving the delivery efficiency of drugs into the brain by adding moieties targeting RMT receptors for an enhanced transport across the BBB [4–8]. HiPS-BMEC-based models could be a valuable complementary tool prior to *in vivo* studies, as it could easily and rapidly screen the DDS functionalized with different ligands for RMT based on their *in vitro* permeation rate. Assessing the possibility of hiPS-BMEC to use TfR-mediated transport is highly desired, as it could create opportunities for finding novel treatments of central nervous system diseases, for example by the screening of peptides or antibody libraries that bind RMT receptors.

In this study, hiPS-BMEC [9] were compared to the immortalized human brain microvascular endothelial cell line (HBEC) [10] with respect to their gene and protein expression profile, as well as their barrier function properties. The functionality of the TfR-mediated transcytosis on hiPS-BMEC was then assessed using the native ligand of the TfR, transferrin. Finally, as an applicative validation, two candidate peptides previously reported to be internalized using TfR [11], cysteine-modified T7 (Sequence CHAIYPRH) or cysteine-modified

Tfr-T12 peptide (Sequence CTHRPPMWSPVWP), were screened with respect to their permeability ability across the hiPS-BMEC monolayer.

2.2. Experiments

2.2.1. Materials

Cysteine-modified T7 peptide (8 AA, CHAIYPRH, cys-T7) and cysteine-modified Tfr-T12 peptide (13 AA, CTHRPPMWSPVWP, cys-TfR-T12) were custom peptides synthesized by Scrum (Tokyo, Japan). (4-(4, 6-dimethoxy-1, 3, 5 -triazine-2-yl)-4-methyl-morpholinium chloride (DMT-MM, nH2O) was purchased from Watanabe Chemical (Hiroshima, Japan) (Ref. 3945-69-5). Unconjugated fluoresceinyl glycine amide (FGA) was obtained from Setareh Biotech (Eugene, OR, USA) (Ref. 136091-82-2). Dimethylsulfoxide (DMSO) was purchased from Nacalai Tesque (Kyoto, Japan) (Ref. 08489-45). Spectra/Por™ Biotech Cellulose Ester (CE) Dialysis Membrane Tubing (MWCO 500-1000Da) was purchased from Spectrum (New Brunswick, NJ, USA) (Ref. 131096). FITC-dextran of 9.5 kDa (Ref. FD10S), 70 kDa (Ref. FD70S), 250 kDa (Ref. FD250S), 2,000 kDa (Ref. FD2000S) were purchased from Sigma-Aldrich (St Louis, MO, USA).

2.2.2. Cell culture

Human brain microvascular endothelial cells/conditionally immortalized clone ci18 (HBEC) used for this work were kindly provided by Prof. Furihata. HBEC were cultured on collagen-coated dishes (100 mm, type I collagen, Iwaki, Tokyo, Japan). Cells were cultured in a humidified incubator (33 °C, 5% CO_2) for the maintenance of growth activity. Culture medium was supplemented with 4 μg/mL of Blasticidin S HCl (Invitrogen, Waltham, MA, USA) to maintain selective pressure for routine culture. HBEC were grown in Vasculife (VEGF-Mv, LifeLine, Carlsbad, CA, USA) supplemented with 0.5 mL rh FGF-b, 0.5 mL ascorbic acid, 0.5 mL hydrocortisone hemisuccinate, 25 mL L-glutamine, 0.5 mL rh IGF-1, 0.5 mL rh EGF, 0.5 mL rh VEGF, 0.5 mL heparin sulfate, 25 mL fetal bovine serum (kit LifeFactor VEGF-Mv, LifeLine, Carlsbad, CA, USA), 25 mL supplementary fetal bovine serum (FBS, Gibco ThermoFisher, Waltham, MA, USA), and 1% penicillin-streptomycin (10,000 U.mL-1 - 10,000 μg/mL, Nacalai Tesque, Kyoto, Japan). For transport studies, 1.0 x 10^5 HBEC were seeded in a 24 well insert (Ref. 662641, Greiner Bio-One, Monroe, NC, USA) pre-coated with 100 μL of fibronectin at 0.04% (fibronectin from human plasma, F2006-5G, Sigma-Aldrich, St. Louis, MO, USA). Insert cultures of HBEC were then incubated at 37 °C for 2 days to induce their differentiation before their use in subsequent experiments, also performed at 37 °C.

Human iPS cells (hiPS) were successfully differentiated to hiPS-BMEC as previously reported [9]. Briefly, hiPS were detached with Accutase (SCR005, Merck, Branchburg, NJ, USA) and seeded on Matrigel-coated 6-well plate at a density of 1-1.5 × 10^5 cells/well and cultured in mTeSR1 medium (Ref. 85850, STEMCELL Technologies, Vancouver, BC, Canada) containing 10 μM ROCK inhibitor Y27632 (Ref. 259-00613, Fujifilm Wako, Osaka, Japan) (day −3). After 24 h, the medium was replaced with fresh mTeSR1 medium without ROCK inhibitor Y27632 (day −2). On day 0, the medium was replaced with unconditioned medium (UM). On day 6, the medium was replaced by human endothelial serum-free medium (SFM, Ref. 11111044, Gibco ThermoFisher, Waltham, MA, USA) containing 1% human platelet-derived serum (hPDS, Ref. P2918 Sigma-Aldrich, St. Louis, MO, USA), 10 μM all-trans-retinoic acid (ATRA, Ref. 182-01116, Fujifilm Wako, Osaka, Japan) and 20 ng/mL human fibroblast growth factor 2 (FGF2, Ref. 161-0010-3, Katayama Chemical Industries Co., Osaka, Japan). On day 8, the cells were detached using Accutase and seeded at a density of 3.3 x 10^5 onto 24-well inserts with 0.4 μm pore size (Ref. 353095, Falcon, Flowery Branch, GA, USA) coated with fibronectin/collagen IV (FN/Col IV, Pharmaco-cell, Nagasaki, Japan) and cultured in SFM with hPDS, ATRA, and FGF2. On day 9, floating cells were removed by washing with SFM, and the medium was replaced with fresh SFM with hPDS. The hiPS-BMEC insert cultures at day 10 of the differentiation were used in subsequent experiments.

2.2.3. Assessment of transendothelial electrical resistance (TEER)

The TEER was monitored for 1 h at different time points (0, 10, 30, 45, 60 min) in SFM medium using the cultures of HBEC and hiPS-BMEC seeded in the 24-well insert. The TEER was measured using a Millicell® ERS-2 Volt-Ohm Meter (Millipore, Bedford, MA, USA) equipped with a STX01 chopstick electrode (Millipore, Bedford, MA, USA). The TEER value was calculated from the following equation (1) [12]:

$$TEER = (R_{monolayer} - R_{blank}) \times A \quad (1)$$

Where $R_{monolayer}$ is the resistance of the cell monolayer along with the filter membrane; R_{blank} is the resistance of the cell-free insert membrane in SFM medium, and A is the surface area of the membrane (0.33 cm^2).

2.2.4. Quantitative Reverse Transcription-PCR (qRT-PCR)

The HBEC and hiPS-BMEC cultured in inserts were rinsed with PBS, and RNA was extracted using PureLink RNA Micro Kit (Invitrogen, Waltham, MA, USA). RNA content was

assessed with a Nanodrop™ spectrometer (N1000, Thermo Fisher Scientific, Waltham, MA, USA). A reverse transcription of the RNA samples into cDNA using iSCRIPT cDNA synthesis kit (Bio-Rad, Hercules, USA) was performed. A real-time quantitative polymerase chain reaction (RT-qPCR) was then conducted on the cDNA samples using Taqman Fast Advanced Mix (Taqman Gene Expression Assays, Thermo Fisher Scientific, Waltham, MA, USA) in the StepOnePlus Real-Time PCR System (Thermo Fisher Scientific, Waltham, MA, USA). Peptidylprolyl Isomerase A (PPIA) was used as the housekeeping gene to normalize the gene expression.

2.2.5. Immunofluorescence

The HBEC and hiPS-BMEC insert cultures were rinsed three times in PBS then fixed in 4% paraformaldehyde (Fujifilm Wako, Osaka, Japan) at room temperature for 15 min. Permeabilization was carried out using 0.2% Triton X-100 for 15 min (Sigma-Aldrich, St. Louis, MO, USA) diluted in PBS. After PBS rinsing, blocking was performed for 1 h at room temperature with 1% bovine serum albumin (BSA, Sigma-Aldrich, St. Louis, MO, USA) in PBS, to minimize non-specific staining. The samples were incubated with primary antibodies overnight at 4 °C: anti-CD31 antibody (mouse anti-human, NCL-CD31-1A10, Leica, Wetzlar, Germany) was diluted in 1% BSA in PBS at 1/100, while antibodies against tight-junction proteins, adherens junction protein and transporters were diluted in 1% BSA in PBS at 1/50 (rabbit anti-human TfR, NB500-493AF647, NovusBio, Centennial, USA) (mouse anti-human ZO-1, ZO1-1A12, Invitrogen, Waltham, MA, USA), 1/100 (mouse anti-human Claudin-5, 35-2500, Thermo Fisher Scientific, Waltham, MA, USA) or at 1/500 (rabbit anti-human VE-cadherin, ab33168, Abcam, Cambridge, UK). Double staining was usually carried out at the same time, except for the anti-TfR antibody which was already conjugated with Alexa Fluor 647. After PBS rinsing, samples were incubated for 2 h at room temperature in the dark with secondary antibodies diluted at 1/100 in 1% BSA in PBS (goat anti-mouse, Alexa Fluor 647, A21235, Thermo Fisher Scientific, Waltham, MA, USA; or goat anti-rabbit, Alexa Fluor 488, ab150077, Abcam, Cambridge, UK). The nuclei were counterstained with Hoechst (Thermo Fisher Scientific, Waltham, MA, USA). After washing three times with PBS, the samples were observed using confocal laser scanning microscope FluoView FV3000 (Olympus, Tokyo, Japan) using x10 or x40 magnification. The images were taken by keeping the same exposure time and excitation power for each sample for fluorescence quantification assessment. Fluorescence intensity of x10 magnification pictures was quantified using Fiji software [13] and normalized by cell number.

2.2.6. Fluorescent labeling of peptides

A stock solution at 1 mg/mL of each peptide was prepared by dissolving 5 mg of cys-T7 or cys-Tfr-12 peptide in MilliQ water. A 500 mM stock solution of DMT-MM was prepared in MilliQ water. 10.04 µL of DMT-MM stock solution (5.02 µmol, 1 eq.) and 6.275 µL of DMT-MM stock solution (3.137 µmol, 1 eq.) were respectively added dropwise to the 5 mL of the stock solution of cys-T7 peptide or cys-Tfr-T12 peptide stock solution (5.02 µmol, 1 eq.). These solutions were stirred at room temperature for 10 min. In parallel, a stock solution of 25 mM of FGA were prepared in DMSO. 7.53 µmol (1.5 eq.) or 4.70 µmol (1.5 eq.) of 25 mM of FGA stock solution are respectively added to the DMT-MM/cys-T7 peptide and DMT-MM/cys-Tfr-T12 reaction mixture and stirred in an ice bath for 1 h and then at room temperature for 24 h. The mixture was then dialyzed for 3 days with a cellulose ester dialysis tubing (MWCO 500-1000 Da) and freeze dried (Freeze Dryer FDU-2200, Eyela, Tokyo, Japan) for 3 days to afford the FGA-labeled peptides.

2.2.7. Permeability Studies

Permeability studies were performed as similarly reported in previous studies [14,15]. For all the permeability studies, HBEC or hiPS-BMEC cultures were rinsed three times with PBS, Human Endothelial Serum Free Medium (SFM) (Ref. 11111044, ThermoFisher, Waltham, MA, USA) was then added to the upper side with the tested molecules (200 µL) and to the lower side (1,000 µL) of the inserts and the system was incubated at 37 °C for the permeability assays for 1 h. Different molecular weights (MW) (9.5, 70, 250, 2,000 kDa) of fluorescein isothiocyanate (FITC) labeled dextran at a final concentration of 1 mg/mL were added to the upper side before beginning the assay. For the competition binding assays, Alexa Fluor 488-transferrin (AF 488-Tf) (009-540-050, Jackson ImmunoResearch, West Grove, PA, USA) (final concentration 125 nM) was co-incubated with different concentrations of unlabeled transferrin (Tf) (009-000-050, Jackson ImmunoResearch, West Grove, PA, USA) (final concentration 0; 12.5; 125; 1250 nM). Alexa Fluor 647-MEM-189 (AF 647-MEM-189) (NB500-493AF647, NovusBio, Centennial, USA), Alexa Fluor 647-immunoglobulin G1 (IgG1) (NBP1-97005AF647, NovusBio, Centennial, USA) and Alexa Fluor 647-13E4 (NB100-73092, NovusBio, Centennial, USA) were incubated at a final concentration of 64 nM with HBEC or hiPS-BMEC. FGA-cys-T7 peptide or FGA-cys-Tfr-T12 peptide at a final concentration of 10 µg/mL were co-incubated with different amounts of unlabeled transferrin (Tf) (final concentration 0; 12.5; 125; 1250 nM) using hiPS-BMEC.

Following the incubation with the tested molecule, 10 µL of the medium was collected in the lower chambers and replaced with the same volume of fresh medium at t=10, 15, 30, 45, 60 min. The fluorescence in the lower chamber was measured using a Nanodrop™ fluorospectrometer (N3300, Thermo Fisher Scientific, Waltham, MA, USA) from which was deduced the amount of transported compound. The cumulative amount transported across the membrane was plotted against time, and the slopes of the linear regions were used to calculate the permeability coefficients, as previously described [15].

The effective permeability coefficient (P_e) was calculated using the following equation (2):

(2) $PS = (dQ/dt)/D_0$

Where PS, dQ/dt, and D_0 are, respectively, the permeability surface area product, the slope of the linear region of a plot of the amount of permeant in the receiver chamber over time, and the initial concentration of the tested molecule on the donor side.

(3) $1/ PS_{total} = 1/ PS_e + 1/ PS_m$

(4) $P_e = PS_e/ A$

Where PS_{total} and PS_m are respectively the permeability surface area product corresponding to the transwell membrane with and without the EC monolayer and PS_e is the surface area product value for the endothelial monolayer. A is the surface area of the insert membrane.

2.2.8. Confirmation of TfR-mediated endocytosis by confocal microscopy imaging

HBEC or hiPS-BMEC were co-incubated with 125 nM of AF488-Tf and 64 nM of AF647 MEM-189 for 1 h at 37 °C. Cells were then fixed with PFA 4%, washed three times with PBS prior to the observation. Images were then taken with a confocal laser scanning microscope AX (Nikon, Tokyo, Japan).

2.2.9. Co-localization studies

HiPS-BMEC insert cultures were washed with PBS three times and incubated with a solution of 10 µM of FGA-cys-T7 or FGA-cys-Tfr-T12 and 125 nM Alexa Fluor 647-transferrin (AF 647-Tf) diluted in SFM medium for 1 h prior to fixation with PFA 4%. Fixed cells were observed with a confocal laser scanning microscope FluoView FV3000 (Olympus, Tokyo, Japan). Images were taken by keeping the same exposure time and excitation power for

each sample. The colocalization ratio between AF 647-Tf and FGA-cys-T7 or FGA-cys-Tfr-T12 peptide was quantified by IMARIS software (Oxford Instruments, Version 9.2.1, Bitplane, Belfast, UK).

2.2.10. Statistical analysis

All values are presented as means ± standard deviation (SD). Statistical analysis of the data was performed with Student's *t*-test or one-way *ANOVA* using EzAnova software when more than two samples were compared (Version 0.985, University of South Carolina, Columbia, SC, USA) with Tukey multiple comparison post-hoc tests. Differences were considered statistically significant at $p < 0.05$.

2.3. Results and discussion

2.3.1. Evaluation of an endothelial marker, tight junctions and transporter expressions

The gene expression and phenotypical features of BMEC/conditionally immortalized clone ci18 (HBEC) or human iPS-derived BMEC-like cells (hiPS-BMEC) were first investigated, focusing on the expression of endothelial cell (EC) markers VE-cadherin and CD31, tight junction proteins (TJs) Claudin-5 and ZO-1 and the specific transporter TfR. The expression of complex TJs between the BMEC is also very important for barrier function properties, as they control the paracellular transport and the maintenance of cell polarity [16]. VE-cadherin is an endothelial-specific transmembrane protein which play a major role in the establishment and development of endothelial cell-cell junction [17,18]. As seen in **Figure 2-1**, RT-qPCR showed that the expression of CD31 was significantly higher (15,000-fold) in HBEC than hiPS-BMEC. Both cell types expressed the gene for Cld5 in a similar manner. However, the mRNA for ZO-1 and TfR were significantly higher for hiPS-BMEC than HBEC.

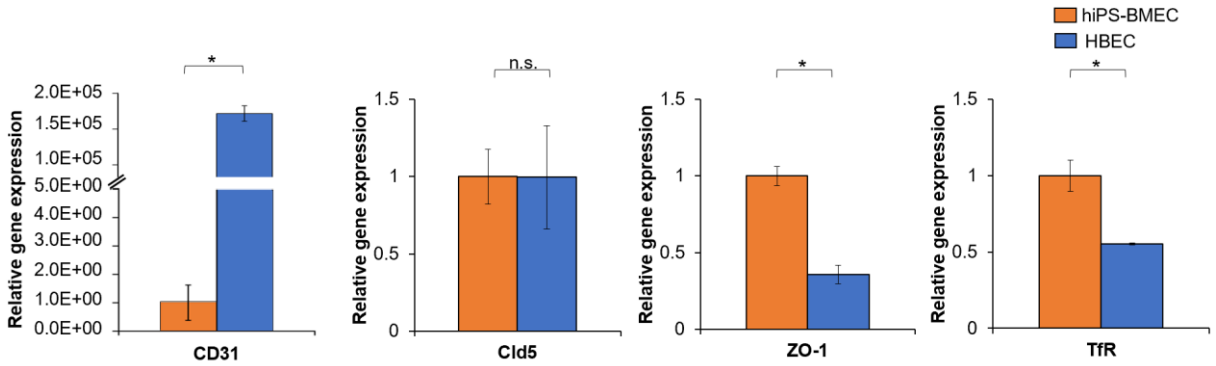

Figure 2-1. Gene expression of endothelial marker, tight junction proteins and transporters between HBEC (blue) and hiPS-BMEC (orange) (n=3). Data are presented as means ± S.D.

The protein expression of the same endothelial marker, TJs, and transporter was also assessed by immunofluorescence staining (**Figure 2-2A**). The comparison of the fluorescence intensity (**Figure 2-2B**) revealed a similar tendency as the RT-qPCR results, with an increased expression of ZO-1 for hiPS-BMEC compared to HBEC. These observations are in line with the previously reported characteristics for hiPS-BMEC, particularly the high expression of TJ proteins, including ZO-1 and Claudin-5 [19,20]. Although differences of Cld5 gene expression could not be detected by RT-qPCR, it was more expressed by hiPS-BMEC than HBEC at the protein level. Moreover, hiPS-BMEC showed uniform and continuous staining for Claudin-5 and ZO-1, while punctate contacts with intercellular gaps was detected with HBEC (**Figure 2-2B**), suggesting differences in barrier stability and integrity. TfR showed higher expression at both gene and protein levels by hiPS-BMEC, as compared to HBEC. Both hiPS-BMEC and HBEC were positive for CD31 and VE-cadherin (**Figure 2-2B**) which is in accordance with previous reports [20,9,10]. Even though CD31 expression at gene level was detected with hiPS-BMEC (**Figure 2-1**), it remains relatively very low as compared to HBEC (**Figure 2-2B**). This higher expression of CD31 by HBEC as compared to hiPS-BMEC is similarly found at the protein level, but to a lesser extent than the gene expression level. The observed differences between expression at gene and protein levels are expected to be due to transcriptional and post-transcriptional regulation processes [21]. Although the comparison of HBEC to primary human

BMEC has been already initiated in a previous work [10], the degree of phenotypical similarities to the *in vivo* brain endothelium for hiPS-BMEC remains however to be elucidated.

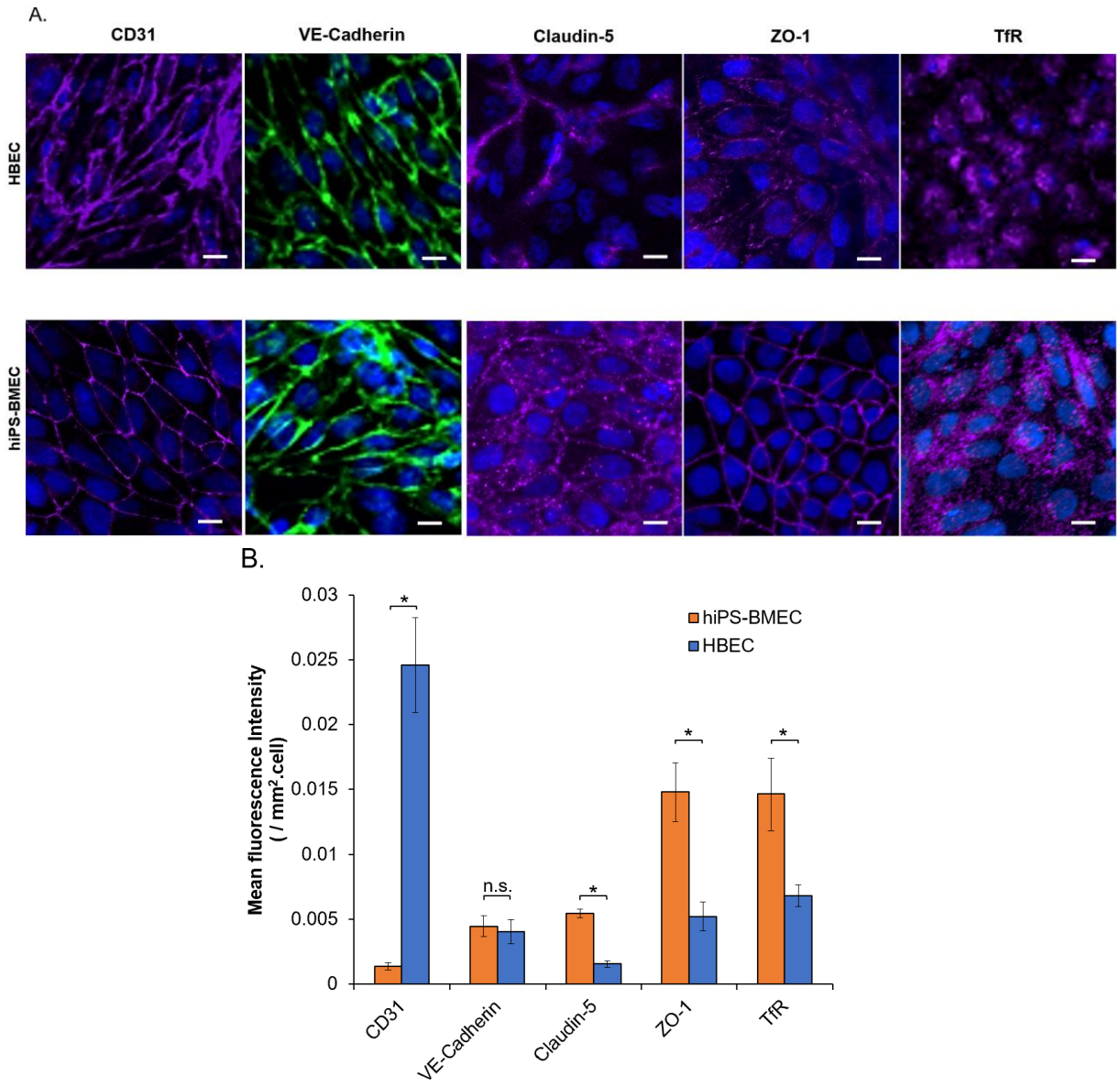

Figure 2-2. (A) Immunostaining of CD31, VE-cadherin, Claudin-5, ZO-1 and TfR observed by confocal microscopy for HBEC and hiPS-BMEC. Scale bar = 10 µm. (B) Immunostaining fluorescence intensity comparison between HBEC (blue) and hiPS-BMEC (orange) using pictures from Figure 2-2A (n=3). Data are presented as means ± S.D.

2.3.2. Evaluation of the barrier function properties

In addition to the expression of BBB markers and vascular phenotype, BMEC should exhibit tight barrier properties. One of the hallmarks of the BBB is its high trans-endothelial electrical resistance (TEER), mainly resulting from the presence of TJ protein interactions between adjacent BMEC [19]. For both cell types, the TEER value remains stable for a period of one hour (**Figure 2-3**), confirming the possibility of performing permeability assays without

any variability in the barrier function properties in this lapse of time. The TEER value for hiPS-BMEC exceeded 1,000 Ω x cm^2, around 100-fold higher than the value obtained for HBEC, independently of the time point measurement. The TEER value observed for hiPS-BMEC is in accordance with previously reported values [19].

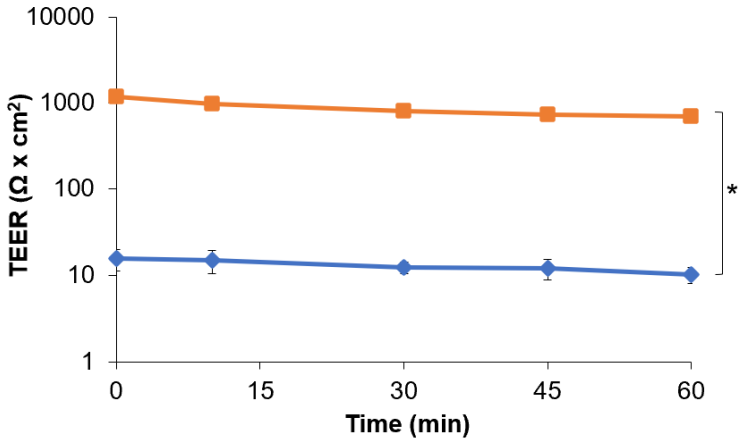

Figure 2-3. TEER measurement for HBEC (blue) and hiPS-BMEC (orange) (n=3). Data are presented as means ± S.D.

Although the *in vivo* TEER values across the BBB in human brain cannot be easily measured, values from the brains of other species such as rat [22] and frog [23] have been estimated to exceed 1,000 Ω x cm^2. Moreover, a study demonstrated that if the TEER can be maintained above 900 Ω x cm^2, the model has the potential to be used to predict *in vivo* human permeability of both small and large molecules [24]. The TEER value obtained for hiPS-BMEC is closer to physiological TEER than HBEC. Although the TEER is a versatile and non-invasive approach to confirm the barrier integrity of the EC monolayer, several factors such as temperature, medium composition, type of electrode probe or surface area can greatly affect the value of the measurement. The TEER value is thus subject to considerable variations between experiments and laboratories [25].

2.3.3. Size-dependent molecular permeability of fluorescent dextran

Paracellular fluorescent tracer compounds, such as fluorescein isothiocyanate-dextran (FITC-dextran), have also been widely used to detect potential leakages in the endothelial barrier [26]. To explore the potential molecular size effect on the permeability of fluorescent tracers, a range of different molecular weights (MW) of FITC-dextran (9.5 kDa, 70 kDa, 250 kDa and 2,000 kDa) were chosen to represent the small, intermediate- and large-sized agents. The P_e values were inversely correlated with the size of the tracer. As shown in **Figure 2-4**, both HBEC and hiPS-BMEC were totally impermeable to 250 and 2,000 kDa FITC-dextran. However, a drastic increase in the permeability was observed with smaller sizes of FITC-

dextran (9.5 and 70 kDa) for HBEC. Conversely, hiPS-BMEC showed a significantly lower permeability to fluorescent tracers than HBEC, even with the smallest ones such as 9.5 kDa FITC dextran. The P_e value of 9.5 kDa FITC-dextran showed a similar trend in the fluctuation changes, with 1.8 x 10^{-8} cm/s for hiPS-BMEC and 1.4 x 10^{-6} cm/s for HBEC (**Figure 2-4**). The junctions of the confluent HBEC cell monolayers appeared to be tight enough to block the transfer of large-sized dextran, 250 and 2,000 kDa FITC dextran, in the lower compartment of the insert but remained permeable to the small- and intermediate-sized ones, 9.5 and 70 kDa FITC dextran. These results are consistent with previous reports, demonstrating the low barrier function properties of EC cell lines compared to hiPS-BMEC. It is generally well accepted that human brain EC lines such as hCMEC/D3 are relatively leaky and exhibit low paracellular resistance. For example, it has been reported that the permeability coefficient of hCMEC/D3 for 4 kDa and 2,000 kDa FITC dextran was about 6.2 x 10^{-6} cm/s and 3.2 x 10^{-6} cm/s respectively [27]. Linville *et al.* reported a similar low permeability of 10 kDa FITC dextran using hiPS-BMEC of about 5.0 x 10^{-8} cm/s [28]. Taken together, these results demonstrated that hiPS-BMEC displayed a restrictive permeability ability of compounds through the cell monolayer that resemble to the *in vivo* brain endothelium [29]. The high TEER value and enhanced size-dependent selectivity of FITC dextran observed with hiPS-BMEC could result from their ability to form stronger and more stable TJs between adjacent cells than HBEC, as seen by ZO-1, VE-cadherin and Claudin-5 junctional continuity and barrier integrity (**Figure 2-2A**).

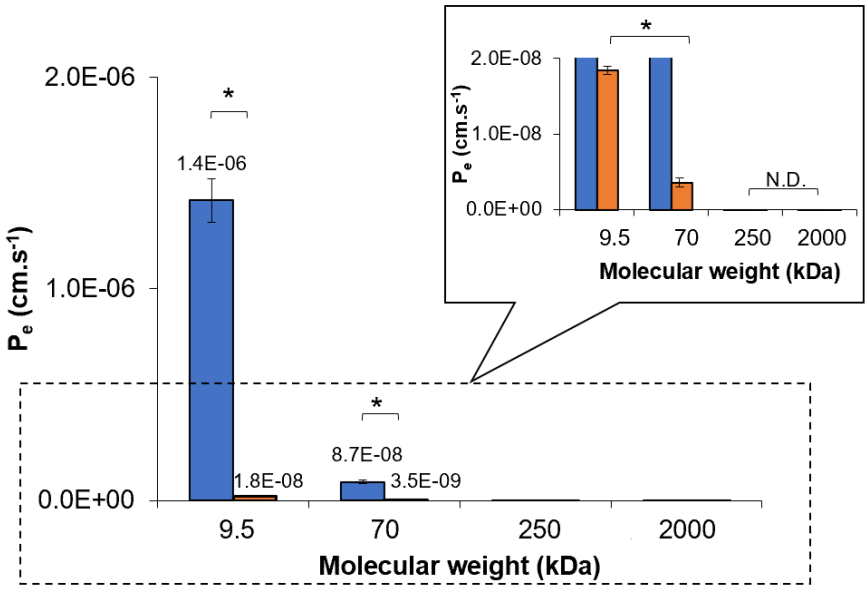

Figure 2-4. P_e values of 1 mg/mL FITC-dextran with different molecular weights (n=3). Data are presented as means ± S.D. N.D. means "not detected".

2.3.4. Confirmation of the Transferrin Receptor-Mediated Transcytosis

The ability of HBEC and hiPS-BMEC to use RMT pathway for the transport of molecules was investigated, with a particular focus on the transferrin receptor (TfR)-mediated transcytosis. In order to validate the interaction between Alexa Fluor 488-transferrin (AF 488-Tf) and TfR, a competition binding was performed using AF 488-Tf in the presence of an excess of unlabeled Tf, the native ligand of TfR. The exact localization of AF 488-Tf was evaluated with HBEC and hiPS-BMEC using confocal laser scanning microscopy. Interestingly, higher amounts of AF 488-Tf can be observed inside hiPS-BMEC than with HBEC in the absence of unlabeled Tf (**Figure 2-5A**), which can be explained by the higher expression of TfR by hiPS-BMEC (**Figure 2-2B**). Both HBEC and hiPS-BMEC showed higher fluorescent signals of AF 488-Tf in the cytoplasm in the absence of unlabeled Tf than when co-incubated with a 10-fold excess of unlabeled Tf (1250 nM) as compared to that of AF 488-Tf (125 nM). The reduced internalization of AF 488-Tf observed inside HBEC and hiPS-BMEC potentially resulted from the competition between AF 488-Tf and unlabeled Tf for the same or overlapping binding region on TfR. The co-incubation with an excess of unlabeled Tf impaired the possibility of AF 488-Tf to bind to TfR, leading to a decrease of the fluorescence signal inside the cells. A similar phenomenon was previously reported, where human serum Tf showed a dose-dependent inhibition of the binding of radiolabeled human serum Tf (^{125}I-hTf) to TfR [30]. By increasing the unlabeled Tf, a lower signal for the radiolabeled Tf was found in the cell lysates, confirming the lower cell internalization of ^{125}I-hTf. Collectively, these results suggest that the fluorescent labeling of Tf does not affect the possibility to bind to TfR, thus AF 488-Tf can be used for monitoring the binding to TfR. Since the cellular uptake of AF 488-Tf could be clearly visualized by confocal imaging when co-incubated with unlabeled Tf, we sought to investigate the possibility to modulate the permeation rate of AF 488-Tf across the monolayer of HBEC or hiPS-BMEC by using a quantitative competition binding assay to TfR. For that, we quantified the permeability of AF 488-Tf during the co-incubation with an increasing concentration of unlabeled Tf in a transwell assay (**Figure 2-5B**). The permeability of AF 488-Tf reached a maximum P_e of 3.9 x 10^{-4} cm/s and 6.0 x 10^{-5} cm/s in the absence of Tf with HBEC and hiPS-BMEC respectively. When co-incubated with a concentration of unlabeled Tf of 12.5 and 125 nM, a high fraction of AF 488-Tf was transported in the bottom compartment of the insert for HBEC but significantly decreased for hiPS-BMEC. The P_e value of AF 488-Tf significantly decreased only above the concentration of 125 nM of unlabeled Tf for HBEC, whereas a

concentration-dependent decrease of the P_e value of AF 488-Tf was found for hiPS-BMEC, indicating AF 488-Tf transport was dependent on the binding to TfR.

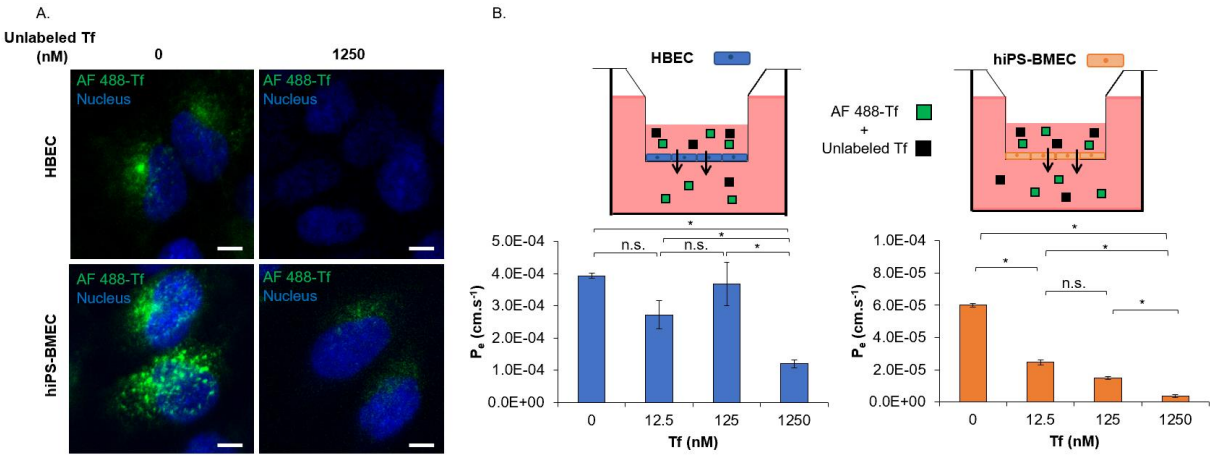

Figure 2-5. (A) Localization of Alexa Fluor 488 labeled Tf (AF 488-Tf) with the co-incubation without or with 1250 nM of unlabeled transferrin (Tf) using HBEC and hiPS-BMEC. Images were taken after 1 h incubation at 37 °C. Scale bar = 10 µm. (B) P_e values of 125 nM of AF 488-Tf with co-incubation at various concentrations (0; 12.5; 125; 1250 nM) of unlabeled Tf with HBEC (blue) and hiPS-BMEC (orange) (n=3). Data are presented as means ± S.D.

Although the presence of RMT transport was confirmed with HBEC, these cells are probably not the most suitable endothelial cell source for the measurement of the modulation of the permeation of RMT ligands, such as AF 488-Tf, due to the contribution of a potential additional paracellular transportation of Tf. **Figure 2-6** showed the expected mechanism to explain the competition binding assay to TfR by hiPS-BMEC. The presence of an increased concentration of unlabeled Tf diminished the probability of AF 488-Tf binding to TfR, leading to the decrease of endocytosis of AF 488-Tf. It is of note that the addition of 125 nM of AF 488-Tf was strongly inhibited by only 12.5 nM of unlabeled Tf, as observed in **Figure 2-5A**, which may be attributed to a higher affinity of unlabeled Tf as compared to AF 488-Tf. This potential change of affinity of AF 488-Tf for TfR could be explained by the presence of the fluorescent labeling. Some precautions may need to be taken when using fluorescent labeling as a detection method for the measurement of the permeability of Tf, as it could potentially affect the affinity of Tf to TfR, thus the permeation rate. The radiolabeling of Tf has been indeed reported to decrease the affinity to TfR [30], such phenomenon may also occur with the fluorescence labeling of Tf. A comparison of the binding affinity between unlabeled Tf or AF 488-Tf to the TfR by the measurement of their equilibrium dissociation constant could be helpful to validate such hypothesis.

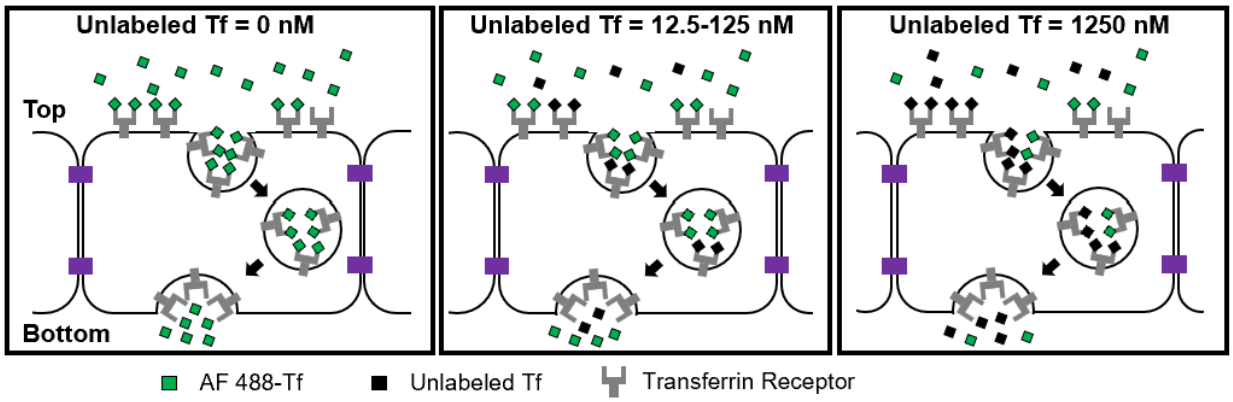

Figure 2-6. Proposed mechanism of the permeation of 125 nM of AF 488-Tf when co-incubated with or without 1250 nM of unlabeled Tf by hiPS-BMEC.

To confirm that AF 488-Tf is able to interact with the TfR despite the fluorescence labeling, we performed a colocalization study with Alexa Fluor 647-MEM-189 (AF 647-MEM-189), a transportable antibody targeting TfR. As observed in **Figure 2-7**, Alexa Fluor 488-transferrin (AF 488-Tf) could be transported into their cytoplasm. The colocalization of AF 488-Tf and AF 647-MEM-189 confirmed that AF 488-Tf was endocytosed by HBEC and hiPS-BMEC by binding to the TfR. The internalization of the Tf-TfR complex leading to release of iron from the ligand is associated with an endosomal acidification [31,32].

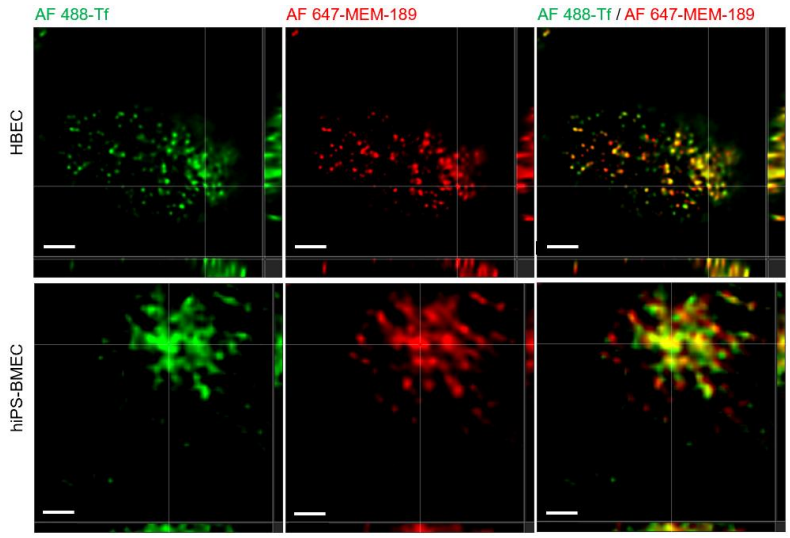

Figure 2-7. Confocal images of HBEC (top) and hiPS-BMEC (bottom) after the co-incubation of 125 nM AF 488-Tf and 64 nM Alexa Fluor 647-MEM-189 for 1 h at 37 °C. Scale bar = 2 μm.

To gain further insights of the permeability of large-sized TfR ligands with HBEC and hiPS-BMEC, we next compared the permeability of AF 647-MEM-189, with the high-affinity human anti-TfR antibody (13E4) and the mouse immunoglobulin G1 isotype control (IgG1), molecules reported to have a poor transportability [33,34]. As seen in **Figure 2-8**, hiPS-BMEC showed the possibility to efficiently transport AF 647-MEM-189 with a P_e value of 1.7 x 10^{-6} cm/s, further validating the presence of TfR-mediated transport. Some differences in the permeability of large-sized TfR ligands were observed between HBEC and hiPS-BMEC. AF 647-MEM-189 showed indeed a higher permeability with HBEC as compared to hiPS-BMEC with a P_e value around 2.5 x 10^{-5} cm/s (**Figure 2-8**). It could be explained by the "leaky" properties of HBEC, which showed an increased permeability for FITC-dextran with a MW < 70 kDa as compared to hiPS-BMEC (**Figure 2-4**). It suggests that AF 647-MEM-189, which has a MW~156.2 kDa, may be transported by both transcellular and paracellular transport with HBEC, but to a lesser extent with hiPS-BMEC. The AF 647-13E4 antibody and AF 647-IgG1 also showed a high permeability for HBEC, with a P_e value of and 1.8 x 10^{-6} cm/s and 3.9 x 10^{-6} cm/s respectively. Conversely, hiPS-BMEC were totally impermeable for AF 647-13E4 and AF 647-IgG1, during the permeability assay, as the fluorescence signal was below the detection limit for these two fluorescent molecules (<100 ng/mL). These results confirm the hypothesis about the additional paracellular transport of large-sized molecules by HBEC, such as AF 647-MEM-189, AF 647-IgG1 or AF 647-13E4, as compared to hiPS-BMEC. The fact that HBEC also have an unstable RMT-mediated permeability was already observed from **Figure 2-5** when Tf was labeled with AF 488, the fluorescent labeling potentially changing its transport efficiency towards an increased paracellular transport. Taken together, these results confirmed that hiPS-BMEC

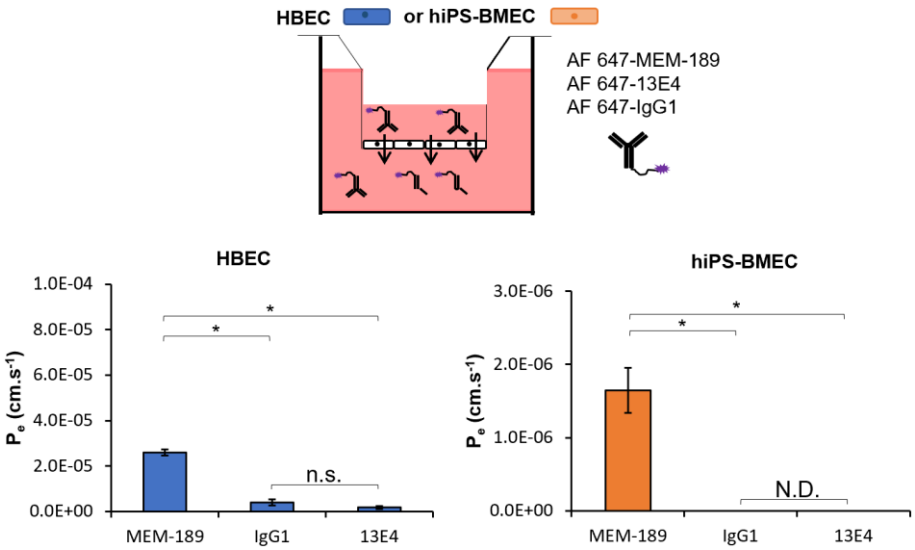

Figure 2-8. Permeation of antibodies binding to TfR using HBEC and hiPS-BMEC. P_e values of 64 nM of AF 647-MEM-189, AF 647-13E4 or AF 647-IgG1 after 1 h incubation at 37 °C (n=3). Data are presented as means ± S.D. N.D. means "not detected".

should be preferred for the accurate measurement of the permeation rates of TfR ligands due to the reduced contribution of the paracellular route as compared to HBEC. Especially, hiPS-BMEC seem to be more reliable for the measurement of the permeation of large-sized molecules such as antibodies.

2.3.5. Screening of cysteine modified T7 or TfR-T12 peptides targeting TfR by competition binding assay with unlabeled Tf

We next investigated whether hiPS-BMEC could be also useful for investigating the permeation of molecules with smaller size, such as peptides binding to TfR. The HAIYPRH (T7) peptide and the THRPPMWSPVWP (Tfr-T12) peptide, discovered by phage display, have been reported as potential ligands of TfR [11]. These peptides have been reported to exhibit a high binding affinity to TfR in the nM range, with a dissociation constant of K_d = 10 and 15 nM for the T7 peptide [35] and Tfr-T12 peptide [11], respectively. These values are comparable to the native ligand, Tf (K_d = 2.8 nM) [11]. The T7 and Tfr-T12 peptides have thus been widely used as ligands for constructing tumor-targeted nanodrug delivery systems [35–40].

Although it has already been reported in the literature that the binding site of the T7 and the Tfr-T12 peptide on TfR was identified to be different from that of the Tf to TfR [11], we wanted to confirm that the site of the fluorescein glycine amide (FGA) labeled cysteine-modified peptides (FGA-cys-T7 and FGA-cys-Tfr-T12 peptide) also does not overlap with that of the Tf on TfR. To verify this, a competition binding assay for TfR was performed by the co-incubation of an increasing concentration of unlabeled Tf and by maintaining the same concentration of the FGA-cys-T7 or FGA-cys-Tfr-T12 peptide (**Figure 2-9A**). As previously stated, both HBEC and hiPS-BMEC are both available to visualize TfR-mediated transcytosis (**Figure 2-7**), but for this permeability assessment, hiPS-BMEC were chosen instead of HBEC since the RMT transport of HBEC was previously found unstable when using labeled proteins such as the AF 488-Tf in the transwell permeability assay (**Figure 2-5**). For hiPS-BMEC, the permeability of both peptides was drastically reduced when co-incubated with a high concentration of unlabeled Tf (1250 nM) (**Figure 2-9B**). The dose-dependent inhibition of the FGA-cys-T7 peptide permeability showed a similar trend to the one found in the competition binding assay between AF 488-Tf and unlabeled Tf with hiPS-BMEC (**Figure 2-5**). Conversely, the FGA-cys-Tfr-T12 peptide did not show any drastic changes in its permeability.

This suggests that the cell transport of the FGA-cys-T7 peptide by hiPS-BMEC may follow the same mechanism as Tf, namely the RMT pathway.

To further validate this possibility, the exact localization of FGA-cys-T7 and FGA-cys-Tfr-T12 peptide was then investigated using hiPS-BMEC (**Figure 2-10A**). The colocalization percentage with AF 647-Tf was higher for the FGA-cys-T7 peptide than for FGA-cys-Tfr-T12 using hiPS-BMEC (**Figure 2-10B**). The FGA-cys-T7 peptide seems slightly more likely able to bind the TfR in presence of AF 488-Tf on TfR, as compared to FGA-cys-Tfr-T12 peptide (**Figure 2-10C**).

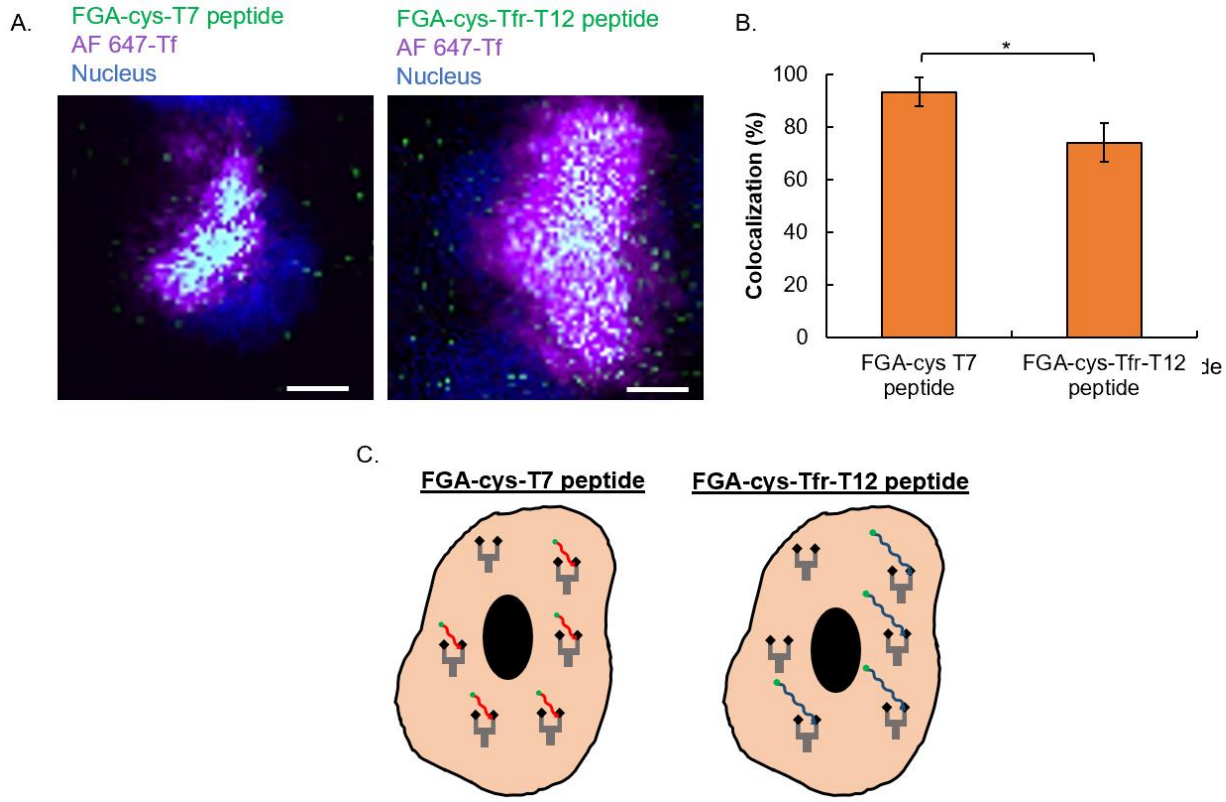

Figure 2-10. (A) Colocalization of FGA-cys-T7 or FGA-cys-Tfr-T12 peptide and AF 647-Tf with hiPS-BMEC. Scale bar = 10 µm. (B) Quantification of the colocalization percentage between FGA-peptides and AF 647-Tf using hiPS-BMEC calculated with IMARIS software (n=3). Data are presented as means ± S.D. (C) Schematic illustration of the interaction between FGA-cys-T7 or FGA-cys-Tfr-T12 peptide and Tf for the binding to TfR using hiPS-BMEC.

2.4. Conclusion

This study showed that hiPS-BMEC could represent a better alternative than the immortalized cell line HBEC to mimic the functional properties of the BBB endothelium. The gene and protein expression of tight junction proteins and transporters was globally upregulated with hiPS-BMEC compared to HBEC, excepting for the endothelial markers CD31 and VE-cadherin. Although both cell types globally showed the same trend in the permeability of the

tested molecules, HBEC exhibited an additional paracellular transport of large-sized molecules compared to hiPS-BMEC, due to their weak expression of tight junctions. The leakiness properties of HBEC are therefore not suitable for the accurate measurement of the permeability of tested molecules, which is fundamental for improving *in vitro* drug testing accuracy and the "bench-to-bedside'' transition of brain cancer drugs. Additionally, the permeability of two peptides transported by the RMT pathway was also confirmed, with a higher permeability of the cys-T7 peptide than the cys-Tfr-T12 peptide by hiPS-BMEC. The cys-T7 peptide could therefore serve as an efficient targeting moiety to enhance the delivery of therapeutics through the BBB endothelium.

2.5. References

[1] S. Yang, S. Mei, H. Jin, B. Zhu, Y. Tian, J. Huo, X. Cui, A. Guo, Z. Zhao, *PLoS One* **2017**, *12*, e0187017.

[2] B. Weksler, I. A. Romero, P.-O. Couraud, *Fluids and Barriers of the CNS* **2013**, *10*, 16.

[3] E. S. Lippmann, A. Al-Ahmad, S. M. Azarin, S. P. Palecek, E. V. Shusta, *Scientific Reports* **2014**, *4*, 4160.

[4] Z. Pang, H. Gao, Y. Yu, L. Guo, J. Chen, S. Pan, J. Ren, Z. Wen, X. Jiang, *Bioconjugate Chem.* **2011**, *22*, 1171.

[5] R. Prades, S. Guerrero, E. Araya, C. Molina, E. Salas, E. Zurita, J. Selva, G. Egea, C. López-Iglesias, M. Teixidó, M. J. Kogan, E. Giralt, *Biomaterials* **2012**, *33*, 7194.

[6] T. Kang, M. Jiang, D. Jiang, X. Feng, J. Yao, Q. Song, H. Chen, X. Gao, J. Chen, *Mol. Pharmaceutics* **2015**, *12*, 2947.

[7] K. Fan, X. Jia, M. Zhou, K. Wang, J. Conde, J. He, J. Tian, X. Yan, *ACS Nano* **2018**, *12*, 4105.

[8] S. Ruan, L. Qin, W. Xiao, C. Hu, Y. Zhou, R. Wang, X. Sun, W. Yu, Q. He, H. Gao, *Advanced Functional Materials* **2018**, *28*, 1802227.

[9] T. Kurosawa, Y. Tega, K. Higuchi, T. Yamaguchi, T. Nakakura, T. Mochizuki, H. Kusuhara, K. Kawabata, Y. Deguchi, *Mol. Pharmaceutics* **2018**, *15*, 5546.

[10] R. Ito, K. Umehara, S. Suzuki, K. Kitamura, K. Nunoya, Y. Yamaura, H. Imawaka, S. Izumi, N. Wakayama, T. Komori, N. Anzai, H. Akita, T. Furihata, *Mol. Pharmaceutics* **2019**, *16*, 4461.

[11] J. H. Lee, J. A. Engler, J. F. Collawn, B. A. Moore, *European Journal of Biochemistry* **2001**, *268*, 2004.

[12] B. Srinivasan, A. R. Kolli, M. B. Esch, H. E. Abaci, M. L. Shuler, J. J. Hickman, *J Lab Autom* **2015**, *20*, 107.

[13] J. Schindelin, I. Arganda-Carreras, E. Frise, V. Kaynig, M. Longair, T. Pietzsch, S. Preibisch, C. Rueden, S. Saalfeld, B. Schmid, J.-Y. Tinevez, D. J. White, V. Hartenstein, K. Eliceiri, P. Tomancak, A. Cardona, *Nature Methods* **2012**, *9*, 676.

[14] H. Sade, C. Baumgartner, A. Hugenmatter, E. Moessner, P.-O. Freskgård, J. Niewoehner, *PLOS ONE* **2014**, *9*, e96340.

[15] S. Nakagawa, M. A. Deli, H. Kawaguchi, T. Shimizudani, T. Shimono, Á. Kittel, K. Tanaka, M. Niwa, *Neurochemistry International* **2009**, *54*, 253.

[16] A. Reichel, D. J. Begley, N. J. Abbott, in *The Blood-Brain Barrier: Biology and Research Protocols* (Ed: S. Nag), Humana Press, Totowa, NJ, **2003**, pp. 307–324.

[17] A.-C. Luissint, C. Artus, F. Glacial, K. Ganeshamoorthy, P.-O. Couraud, *Fluids and Barriers of the CNS* **2012**, *9*, 23.
[18] W. Li, Z. Chen, I. Chin, Z. Chen, H. Dai, *Curr Neuropharmacol* **2018**, *16*, 1375.
[19] E. S. Lippmann, S. M. Azarin, J. E. Kay, R. A. Nessler, H. K. Wilson, A. Al-Ahmad, S. P. Palecek, E. V. Shusta, *Nat Biotechnol* **2012**, *30*, 783.
[20] E. S. Lippmann, A. Al-Ahmad, S. M. Azarin, S. P. Palecek, E. V. Shusta, *Scientific Reports* **2014**, *4*, 4160.
[21] P. Lu, C. Vogel, R. Wang, X. Yao, E. M. Marcotte, *Nat Biotechnol* **2007**, *25*, 117.
[22] A. M. Butt, H. C. Jones, N. J. Abbott, *The Journal of Physiology* **1990**, *429*, 47.
[23] C. Crone, S. P. Olesen, *Brain Research* **1982**, *241*, 49.
[24] J. L. Mantle, L. Min, K. H. Lee, *Mol. Pharmaceutics* **2016**, *13*, 4191.
[25] B. Srinivasan, A. R. Kolli, M. B. Esch, H. E. Abaci, M. L. Shuler, J. J. Hickman, *J Lab Autom* **2015**, *20*, 107.
[26] F. Yu, N. D. S. Kumar, L. C. Foo, S. H. Ng, W. Hunziker, D. Choudhury, *Biotechnology and Bioengineering* **2020**, *117*, 1127.
[27] E. De Jong, D. S. Williams, L. K. E. A. Abdelmohsen, J. C. M. Van Hest, I. S. Zuhorn, *Journal of Controlled Release* **2018**, *289*, 14.
[28] R. M. Linville, J. G. DeStefano, R. F. Nerenberg, G. N. Grifno, R. Ye, E. Gallagher, P. C. Searson, *Mol. Pharmaceutics* **2020**, *17*, 3425.
[29] A. S. Easton, M. H. Sarker, P. A. Fraser, *The Journal of Physiology* **1997**, *503*, 613.
[30] H. Fuchs, R. Gessner, *Biochim Biophys Acta* **2002**, *1570*, 19.
[31] A. N. Steere, S. L. Byrne, N. D. Chasteen, A. B. Mason, *Biochimica et Biophysica Acta (BBA) - General Subjects* **2012**, *1820*, 326.
[32] M. D. Kleven, S. Jue, C. A. Enns, *Biochemistry* **2018**, *57*, 1552.
[33] H. Sade, C. Baumgartner, A. Hugenmatter, E. Moessner, P.-O. Freskgård, J. Niewoehner, *PLOS ONE* **2014**, *9*, e96340.
[34] T.-E. Park, N. Mustafaoglu, A. Herland, R. Hasselkus, R. Mannix, E. A. FitzGerald, R. Prantil-Baun, A. Watters, O. Henry, M. Benz, H. Sanchez, H. J. McCrea, L. C. Goumnerova, H. W. Song, S. P. Palecek, E. Shusta, D. E. Ingber, *Nature Communications* **2019**, *10*, 2621.
[35] S. Oh, B. J. Kim, N. P. Singh, H. Lai, T. Sasaki, *Cancer Letters* **2009**, *274*, 33.
[36] L. Han, R. Huang, S. Liu, S. Huang, C. Jiang, *Mol. Pharmaceutics* **2010**, *7*, 2156.
[37] J. Tang, Q. Wang, Q. Yu, Y. Qiu, L. Mei, D. Wan, X. Wang, M. Li, Q. He, *Acta Biomater* **2019**, *83*, 379.
[38] S. Wang, H. Sun, *Pharmaceutical Development and Technology* **2020**, *25*, 1063.
[39] L.-M. Mu, Y.-Z. Bu, L. Liu, H.-J. Xie, R.-J. Ju, J.-S. Wu, F. Zeng, Y. Zhao, J.-Y. Zhang, W.-L. Lu, *Scientific Reports* **2017**, *7*, 3487.
[40] C. Wängler, D. Nada, G. Höfner, S. Maschauer, B. Wängler, S. Schneider, E. Schirrmacher, K. T. Wanner, R. Schirrmacher, O. Prante, *Mol Imaging Biol* **2011**, *13*, 332.

Chapter 3

Development of Highly Sensitive Molecular Blocks at Cancer Microenvironment for Rapid Cancer Cell Death

3.1. Introduction

Nanotechnology has been actively investigated to target malignant tissues due to their easy functionalization and their nano-size allowing a facile access to biological compartments [1]. Various DDS have been experimented for improving delivery efficiency into the tumor site, such as micelles [2,3], liposomes [4,5] or dendrimers [6,7]. These constructions allow the modulation of the physicochemical parameters of a drug and enhance their bioavailability in tissue. Among them, polymeric nanoparticles have attracted increasing attention owing to their bioavailability, biodegradability and long-time retention as compared to other formulations [8]. Many of the current strategies for drug accumulation at the tumor site rely on the enhanced permeability and retention effect (EPR) which take advantage of the leaky blood vessels and less lymph vessels at the cancer microenvironment [9]. Despite the great improvement in DDS formulation, it is still challenging to deliver high concentrations of drugs at the tumor site. It has been demonstrated that not only 0.7% of the DDS can reach the tumor site, but also the delivery efficiency did not improve for the few past years [10]. This is why other strategies should be considered to circumvent the current issues encountered with conventional methods. To improve the circulation in the bloodstream, avoid immune response and/or to overcome the physiological barrier [11], tumor microenvironment responsive aggregation would be effective. To overcome the difficulty of the delivery of anti-cancer drug into the cell nucleus, cell membrane disruption would be promising as a “drug-free” therapy. These approaches are characterized by the use of formulations in which the nanoparticle acts itself to induce cancer cell death [12,13].

Our group previously reported the synthesis of molecular block (MB) composed of 4-arm polyethylene glycol (4-arm PEG) and deoxycholic acid (DCA) [14]. The MB were designed to disperse as nanoscale assemblies in the bloodstream for efficient circulation and penetration through the stromal tissues. When the MBs reach the tumor site, they self-assembled in microscale aggregates on the cancer cell surfaces in response to the cancer microenvironment and induced cancer cell death. Dibenzocyclooctyne acid (DBCO) was used as a linker between azide modified-DCA and 4-arm PEG by copper-free click reaction. DCA was selected as a

cancer microenvironment-responsive unit owing to its acid dissociation constant (pK_a) of 6.6 [15]. DCA shows self-aggregation behavior in weak acidic environment (pH 6.5), which correspond to the pH found in the tumor microenvironment [16]. The self-assembling properties of the previous MB (4-PEG-DBCO-DCA) could induce cancer cell death by membrane disruption via hydrophobic interaction. However, *in vivo* studies showed that 4-PEG-DBCO-DCA was rapidly cleared from the body before reaching the tumor site and was mainly found in the liver, kidney and spleen regions. It was hypothesized that the presence of the highly hydrophobic molecule DBCO could affect the nanoscale dispersion of the MB in the bloodstream, hence the bioavailability in the body.

In this study, a new approach was investigated for the synthesis of MB in order to control its global hydrophobicity. Finding the proper hydrophobic-hydrophilic balance is critical to achieve a nanoscale dispersion of MB at neutral pH and obtain rapid aggregation at weak acid conditions for disrupting cancer cell membrane. It is highly desired to optimize of the design of MB so that it circulates as a nanoscale in the blood circulation, achieves high and fast accumulation at the tumor site, and induces cancer cell death through self-assembly in response to the cancer microenvironment. Propiolic acid (PA), which is an electron-deficient alkyne available for copper-free click reaction [17,18], was selected as a potential candidate to replace DBCO due to its smaller size and lower hydrophobicity (**Figure 3-1**). The effect of the substitution degree of DCA on the aggregation properties of 4-PEG-PA-DCA was investigated and compared to 4-PEG-DBCO-DCA. Finally, the cell killing capacity of 4-PEG-PA-DCA was assessed on *in vitro* 2D cultures of normal cells and cancer cell lines.

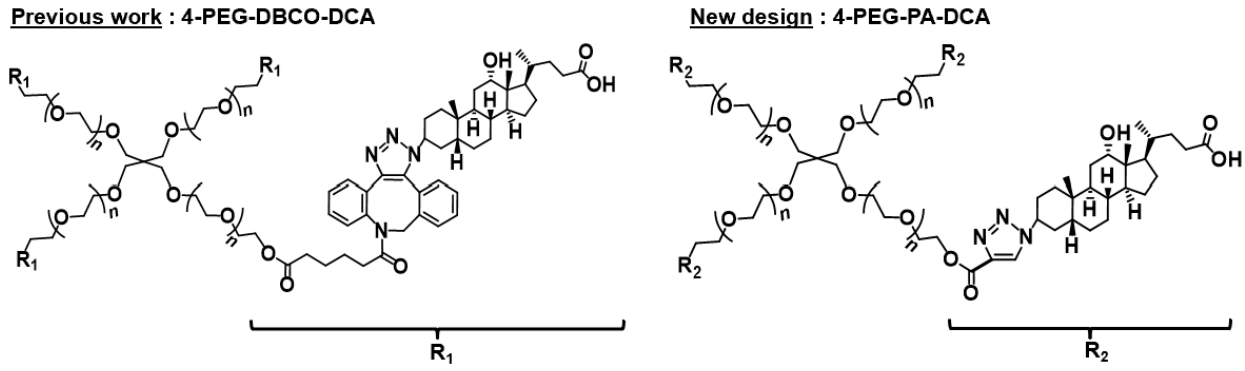

Figure 3-1. Chemical structure of the previous MB (4-PEG-DBCO-DCA) and newly designed MB (4-PEG-PA-DCA).

3.2. Experiments

3.2.1. Materials

4-arm polyethylene glycol (4-PEG-OH) with MW 20,000 Da (Ref. PJK-402) was purchased from CreativePEGworks (Chapel Hill, NC, USA). Propiolic acid (PA) (Ref. P0497, Purity >97.0%), *p*-toluene sulfonic acid monohydrate (PTSA) (T0267) and diethyl ether anhydrous (stabilized with BHT) (D3479) were purchased from Tokyo Chemical Industry (Tokyo, Japan). Ethanol (Ref. 14713-95, purity 99.5%), sodium azide (NaN_3) (Ref. 31208-82) and pyrene (Ref. 29506-42) were purchased from Nacalai Tesque (Kyoto, Japan). Pyridine dehydrated (Ref. 167-18455), *N, N* dimethylformamide (DMF) (Ref. 048-20623), ethyl acetate (Ref. 051-00351), methane sulfonyl chloride (MsCl) (Ref. 131-01583), methanol (Ref. 132-12385), chloroform (Ref. 035-02611), super dehydrated toluene (Ref. 202-17911) and 5 M hydrochloride acid (HCl) (Ref. 081-05435) were purchased from Wako Chemicals (Osaka, Japan). All chemicals were used without further purification.

3.2.2. Synthesis of 4-PEG-PA-DCA

3.2.2.1. Alkynation of 4-PEG-OH

The 4-PEG-OH (360 mg, 18 μmol), PA (89 μL, 1.44 mmol) and PTSA (8 mg, 48 μmol) were dissolved in 7.2 mL of toluene and refluxed using Dean-Stark conditions at 84 °C [19]. After 5 days, the obtained product was concentrated under reduced pressure, dissolved in chloroform, added dropwise to dry-ice cooled diethyl ether and then centrifuged for 5 min at 10,000 rpm. The supernatant was removed and the pellet was vacuum dried overnight before analysis by FT-IR and ^{1}H-NMR.

3.2.2.2. Azidation of deoxycholic acid

After dissolving DCA (592 mg, 1.5 mmol) in 10 mL of pyridine at 0 °C, methane sulfonyl chloride (140 μL, 1.8 mmol) was added dropwise and stirred for 30 min. The reaction was then stirred for an additional 3 h at room temperature. After the reaction, 100 mL of 2M HCl was added to the mixed solution to acidify the solution. The mixture was extracted by 100 mL of ethyl acetate for three times. The organic phase was separated, evaporated and further vacuum dried for 3 h. The structure of the obtained mesylated-DCA (DCA-Ms) was confirmed by FT-IR and ^{1}H-NMR.

DCA-Ms (47 mg, 0.10 µmol) was dissolved in 5 mL of DMF and sodium azide (20 mg, 0.31 µmol) was added and stirred at 70 °C for 24 h. After the reaction, 10 mL of 2 M HCl was added to acidify the mixture, and centrifuged during 2 h at 15,000 rpm. The supernatant was removed and the pellet was then further vacuum dried overnight to obtain a white solid. The structure of the azide-modified DCA (N_3-DCA) was analyzed by FT-IR and ^{1}H-NMR.

3.2.2.3. Click reaction between 4-PEG-PA and N_3-DCA

The 4-PEG-PA (55 mg, 2.71 µmol) was dissolved in 200 µL of methanol with N_3-DCA and stirred for 24 h at room temperature. Different amounts of N_3-DCA were used to prepare 4-PEG-PA-DCA20, 4-PEG-PA-DCA50, 4-PEG-PA-DCA75, respectively 1:1, 1:12, 1:6 alkyne: azide ratio. After the reaction, an equal volume of water was added to the resulting crude solution and then dialyzed against water for 3 days, followed by a freeze-drying for 3 days. The structure of the obtained product was confirmed by FT-IR and ^{1}H-NMR.

3.2.3. Structural and functional characterizations

3.2.3.1. Chemical structure and composition

^{1}H-NMR spectra were recorded with JNM-GSX 400 MHz spectrometer (JEOL, Tokyo, Japan) in $CDCl_3$ at 25 °C. FT-IR spectra were obtained with Spectrum 100 spectrophotometer (PerkinElmer, Llantrisant, UK).

3.2.3.2. Characterization of the microscale aggregation formation

DCA-sodium, 4-PEG-PA, and 4-PEG-PA-DCA were dissolved in PBS at 1 mg/mL. The pH of these solutions were adjusted to 6.2 using 0.1 M HCl. Pictures of the solutions were taken using either a numeric camera and phase contrast microscopy images were recorded with EVOS microscope (ThermoFisher Scientific, Waltham, US).

3.2.3.3. Characterization of the dispersion and nanoscale aggregation formation

The 4-PEG-PA-DCA was dissolved in PBS at pH 7.4 or pH 6.2 at 1 mg/mL. Before measurement, the solution was filtered with a 1 µm pore size PTFE syringe filter (Ref. 6784-2510), purchased from Whatman (Sigma Aldrich, St Louis, MO, US). The diameter size of each

sample were measured at 25 ^{o}C by dynamic light scattering (DLS) measurement using a Zetasizer nano ZS (Malvern Panalytical, Worcs, UK).

3.2.3.4. Determination of critical micelle concentration

Fluorescence spectroscopy was employed to determine the critical micelle concentration (CMC) of DCA-Na and 4-PEG-PA-DCA at pH 7.4 and 6.2 [20]. Briefly, 10 µL of 10^{-4} M pyrene in ethanol was added to 1.5 mL vials and evaporated with nitrogen flux. Various concentrations of the tested compound were incubated in each vial overnight at room temperature before fluorescence measurement. Fluorescence spectra were analyzed using a fluorospectrophotometer (Perkin-Elmer LS55, Perkin-Elmer Ltd., Llantrisant, UK) at 37 °C. The emission and excitation wavelengths were set at 372 and 339 nm, respectively. The ratio of the intensity between the peaks at 373 nm and at 383 nm was calculated to determine the CMC.

3.2.4. Observation of the nanostructures of 4-PEG-PA-DCA by transmission electron microscope

The 4-PEG-PA-DCA was dissolved at 1 mg/mL in MiliQ water at pH 7.4 or 6.2 and then dropped on the carbon coated copper disk for 10 min at room temperature. The samples obtained were stained with 2% uranyl acetate before observation using a transmission electron microscope (TEM) microscope.

3.2.5. Evaluation of cytotoxicity response to weak acidic conditions

NHDF and HT29 were purchased from Lonza (Basel, Switzerland). MiaPaCa-2 was purchased from ATCC (Manassas, VA, USA). NHDF, HT29 and MiaPaCa-2 were maintained in DMEM supplemented with 10% fetal bovine serum (FBS) and 1 % antibiotics. Cells were cultured in 5% CO_2 and 95% humidified air at 37 °C and passaged every 3 days. NHDF, MiaPaCa-2, or HT29 were seeded on 24-well plate at 1 x 10^5 cells/well. After 24 h, 1 mL of 4-PEG-PA-DCA at 1 mg/mL was added in DMEM medium supplemented with 10% FBS and 1% antibiotics at pH 7.4 or pH 6.2 in each plate and incubated for 8 h at 37 °C. Control samples were also prepared at pH 7.4 or pH 6.2 without treatment with 4-PEG-PA-DCA. The pH was adjusted to 6.2 using 1M HCl solution. Phase contrast microscope images were taken every 2 h during the incubation time. After the incubation, the cells were trypsinized for 5 min at 37 °C

and harvested. Cell viability was evaluated by trypan blue method with automatic cell counter Countess II (ThermoFisher Scientific, Waltham, US).

3.2.6. Statistical analysis

The results were expressed as means ± standard deviation (SD). Student's *t*-test and One-way analysis of variance (*ANOVA*) with Pairwise comparison were used for data analysis, with $p < 0.05$ being considered statistically significant.

3.3. Results and discussion

3.3.1. Synthesis and characterization of 4-PEG-PA-DCA

The design of a new type of MB for higher assembling sensitivity at cancer microenvironment, named 4-PEG-PA-DCA, was considered using propiolic acid (PA) as a small and hydrophilic copper-free click reagent [17] to replace DBCO linker. The DBCO unit was expected to be a potential cause of the off-target aggregation in blood stream due to its excessive hydrophobicity. Li and coworkers reported that electron-deficient internal or terminal alkynes, such as PA, is useful for 1,3-dipolar cycloaddition with azide under mild condition in water [17].

The 4-PEG-PA-DCA was successfully synthesized, as characterized by ^{1}H NMR and FT-IR measurement. As seen in **Figure 3-2**, the characteristic peaks of both 4-PEG-PA and DCA could be indeed found in the NMR spectrum of the final product, with peaks between 3.3 and 3.8 ppm

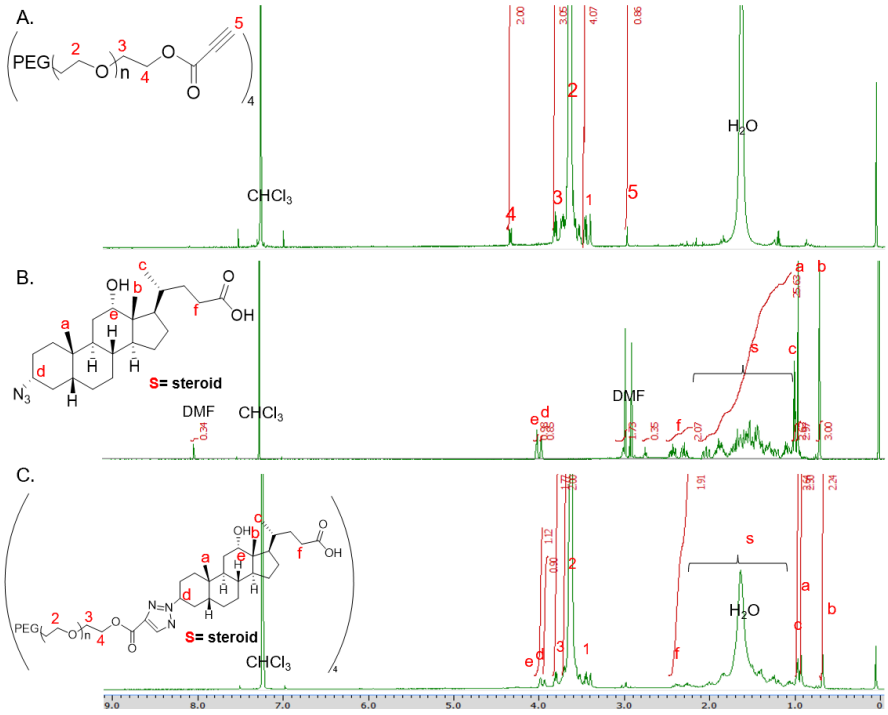

Figure 3-2. ^{1}H NMR spectra ($CDCl_3$, 400 MHz, 25 °C) (A) 4-PEG-PA, (B) DCA-N3, (C) 4-PEG-PA-DCA.

peak at 3.9 and the peak at 4.0 ppm belonging to DCA. In the FT-IR spectra (**Figure 3-3**), we could see the characteristic stretching bands of C=O at 1700 cm^{-1} from DCA group, as well as the stretching bands of alkyne (C≡C) and azide group (N_3) at 2100 cm^{-1} from PA and DCA groups.

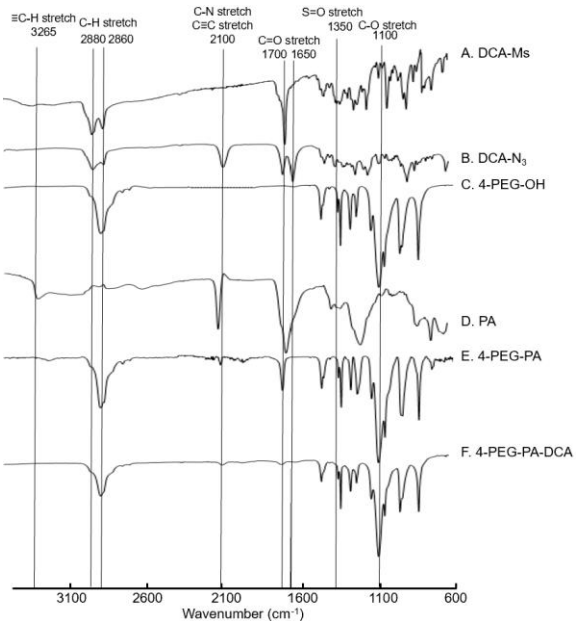

Figure 3-3. FT-IR spectra of (A) DCA-Ms, (B) DCA-N3, (C) 4-PEG-OH, (D) PA, (E) 4-PEG-PA, (F) 4-PEG-PA-DCA.

The 4-PEG-PA-DCA quickly showed the aggregation formation at pH 6.2 in aqueous solutions because of protonation of the carboxylate group of the deoxycholic acid (DCA), same as the previous MB constructs (**Figure 3-4A,B**). TEM observation clearly revealed the presence of small particles at around 30 nm size at pH 7.4, whereas large-sized aggregates resulting from the self-assembly of the small particles could be found at pH 6.2 (**Figure 3-4C**).

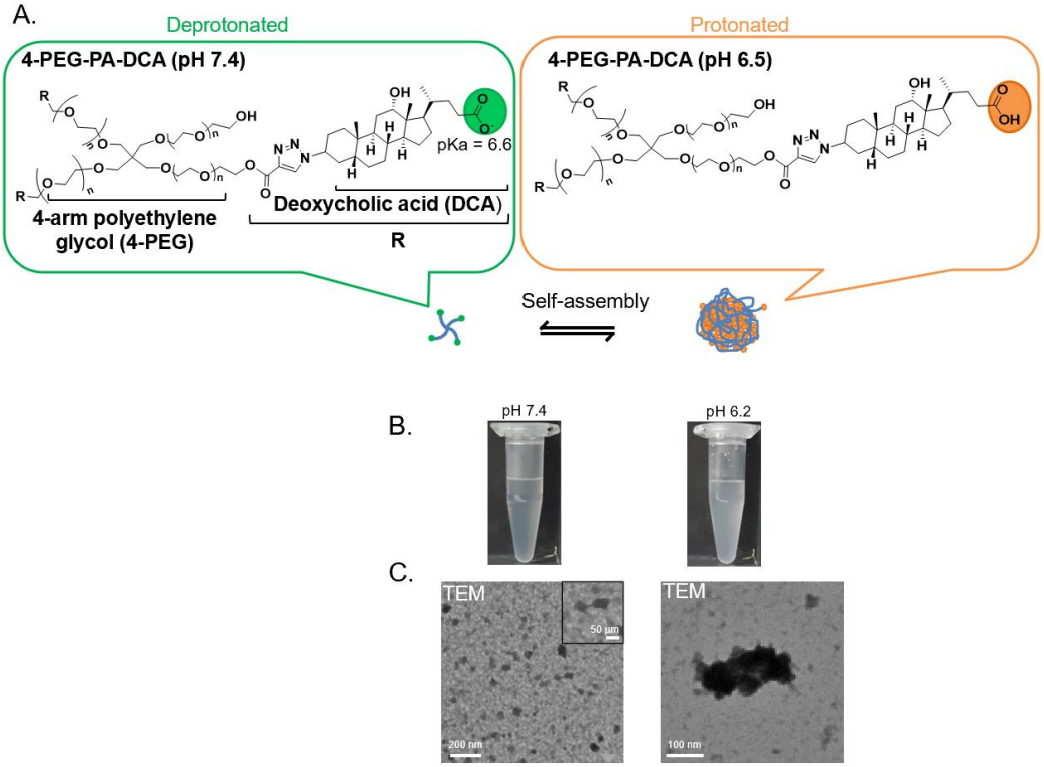

Figure 3-4. Schematic illustration of 4-PEG-PA-DCA in response to the pH change. (A) Chemical structure of 4-PEG-PA-DCA at pH 7.4 (green) and pH 6.2 (orange). (B) Pictures of 4-PEG-PA-DCA75 in PBS at pH 7.4 and pH 6.2. (C) TEM images of 4-PEG-PA-DCA75 in water at pH 7.4 and pH 6.2.

The different degree of substitution (DS) of DCA was successfully obtained by changing infeed molar ratio of azide and alkyne (**Table S1**).

Table 1. Synthetic conditions and characterization of synthesized MB.

Designation	MW PEG (kDa)	Repeat Unit	Yield (%)	DS (%)	alkyne: azide ratio
4-PEG-PA-DCA20	20	110	65	19	1:1
4-PEG-PA-DCA50	20	110	86	51	1:12
4-PEG-PA-DCA75	20	110	91	74	1:6

* The DS of DCA was measured by ^{1}H-NMR in $CDCl_3$.

The influence of the DCA unit number on 4-PEG-PA-DCA was evaluated, using 20% DCA (4-PEG-PA-DCA20), 50% DCA (4-PEG-PA-DCA50) or 75% DCA (4-PEG-PA-DCA75) constructs. DCA is one of the secondary bile salts, which have a rigid and planar hydrophobic steroid core with hydroxyl and carboxylate groups. Due to its amphiphilic properties, DCA can easily form micelles [21]. The critical micelle concentration (CMC), defined as the surfactant concentration at which micelles are formed, was evaluated by the pyrene method [22]. The CMC of sodium DCA (DCA-Na) decreased to half, from 0.4 mg/mL at pH 7.4 to 0.2 mg/mL at pH 6.2 respectively (**Figure 3-5**) due to the increasing hydrophobicity resulting from the protonation of the carboxylate group of DCA. Interestingly, all 20, 50, 75% DCA substitutions showed the same trend with DCA-Na but decreasing ratio of CMC at pH 6.2 from 7.4 was dependent of the substitution percentage of DCA, which strongly changed for the highest DCA substitution percentage (75%) but not for the other constructs (20 and 50%). It was indeed observed 40% decrease for 4-PEG-PA-DCA20 and 32% decrease for 4-PEG-PA-DCA50 but 63% decrease for 4-PEG-PA-DCA75. Taken together, these results suggest that the balance between hydrophilic and hydrophobic regions in 4-PEG-PA-DCA greatly influences the physical properties and plays a major role in the micellization process.

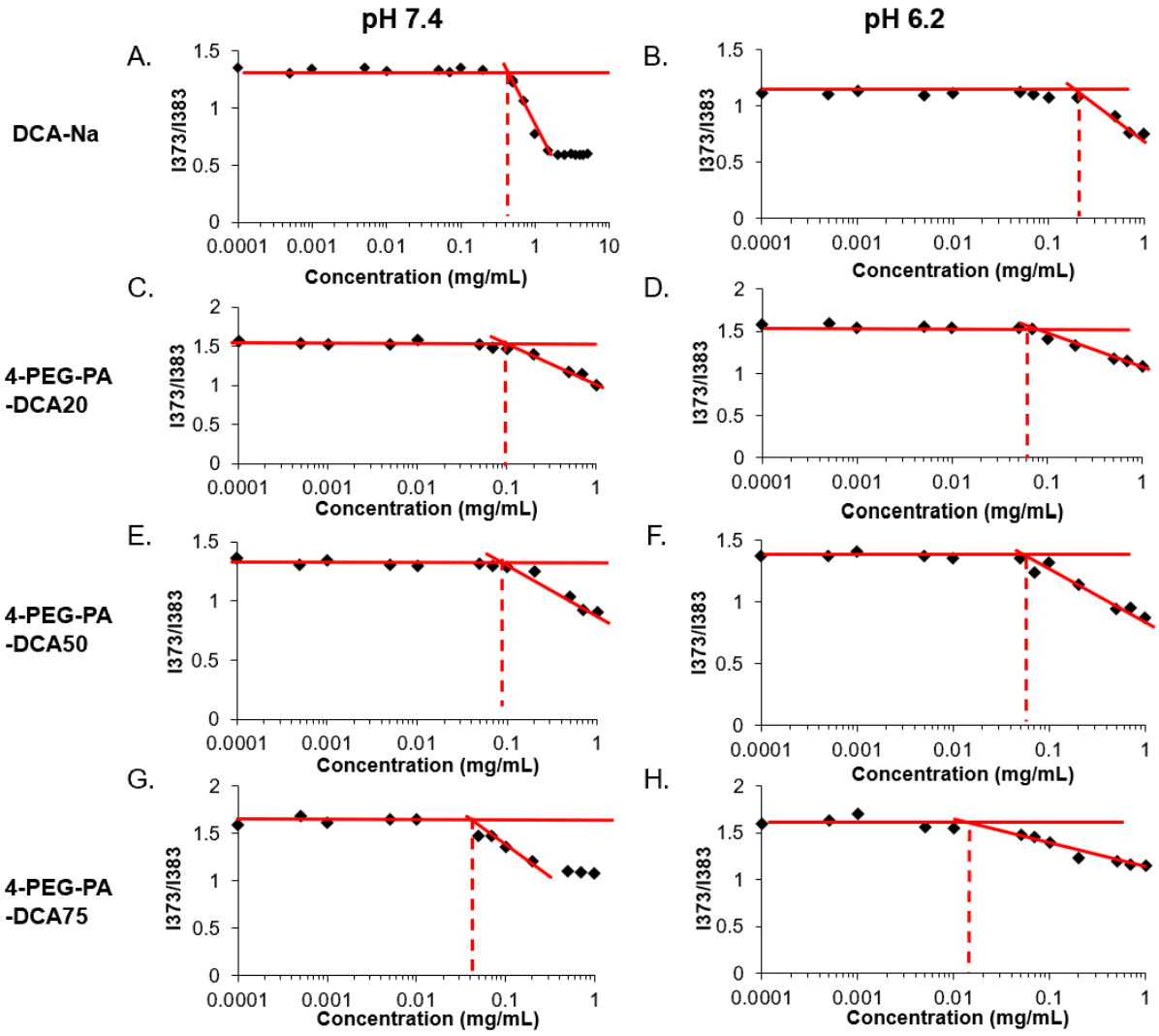

Figure 3-5. CMC measurement evaluated by the pyrene method. (A) Sodium DCA (DCA-Na) at pH 7.4. (B) Sodium DCA (DCA-Na) at pH 6.2. (C) 4-PEG-PA-DCA20 at pH 7.4. (D) 4-PEG-PA-DCA20 at pH 6.2. (E) 4-PEG-PA-DCA50 at pH 7.4. (F) 4-PEG-PA-DCA50 at pH 6.2. (G) 4-PEG-PA-DCA75 at pH 7.4. (H) 4-PEG-PA-DCA75 at pH 6.2. The red dashed lines indicate CMC values.

3.3.2. Aggregation property of 4-PEG-PA-DCA in response to weak acid condition

The effect of the DS of DCA on the 4-PEG-PA-DCA on the aggregation properties was also investigated. The hydrodynamic diameter of 4-PEG-PA-DCA20, 4-PEG-PA-DCA50 and 4-PEG-PA-DCA75 was analyzed by DLS (**Figure 3-6**). The diameter of 4-PEG-PA-DCA20 and 4-PEG-PA-DCA50 was the same (~220 nm) at pH 7.4 and it was slightly increased by decreasing the pH at 6.2 (~250 nm). On the other hand, the highest DS (4-PEG-PA-DCA75) revealed the smallest size at 35 nm at pH 7.4 and significant size increase to 10-fold higher (~350 nm) at pH 6.2, suggesting the highest sensitivity at cancer microenvironment. Since the

size of 4-PEG-PA-DCA75 at pH 7.4 was smaller than that of the previous MB (4-PEG-DBCO-DCA87; 50 nm) [14], probably due to the lower hydrophobicity of PA, a higher dispersion and lower elimination of 4-PEG-PA-DCA in the bloodstream can be expected. Furthermore, because nanometer-scale aggregation size of 4-PEG-PA-DCA75 at pH 6.2 was over two-fold larger than that of the previous MB with 164 nm, 4-PEG-PA-DCA75 is expected to have higher pH sensitivity.

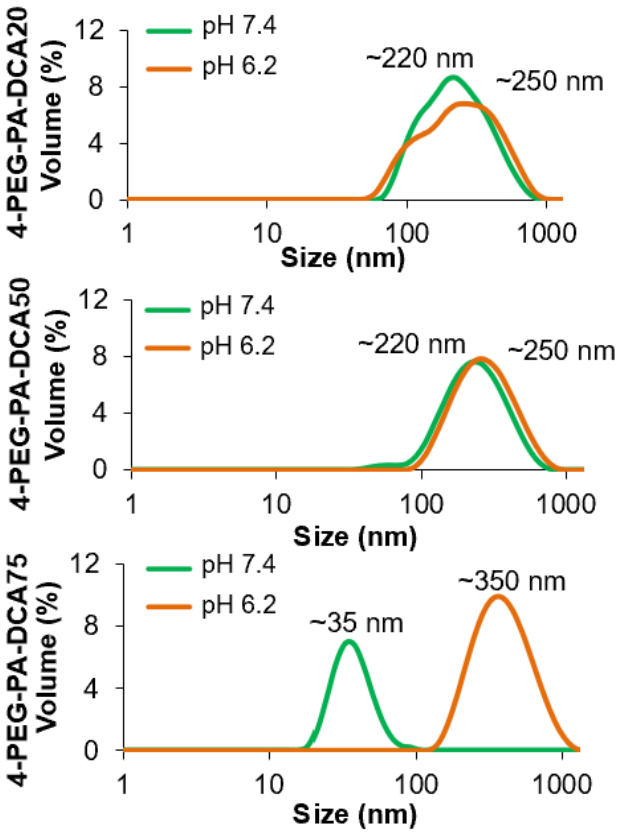

Figure 3-6. Size distribution of 4-PEG-PA-DCA20, 4-PEG-PA-DCA50 and 4-PEG-PA-DCA75 in PBS at 1 mg/mL at pH 7.4 (green) or pH 6.2 (orange) at r.t. evaluated by DLS.

Further observation using the phase contrast microscopy revealed micrometer-sized aggregates of 4-PEG-PA-DCA50 and 75 at pH 6.2, but not 4-PEG-PA-DCA20 (**Figure 3-7A).** Over hundred aggregates numbers of these two samples were clearly observed and the diameter size of the micrometer-sized aggregates of 4-PEG-PA-DCA50 and 4-PEG-PA-DCA75 was about 5 and 12 μm respectively (**Figure 3-7B,C**). Notably, the size of the aggregates of 4-PEG-PA-DCA50 and 4-PEG-PA-DCA75 is much larger than that of the previous MB with 2 μm [14]. Since DCA can self-associate in water and form micelles, it is expected that the PEG-PA-DCA also self-associates to form aggregates, whose size can be positively correlated with the increasing number of DCA moieties [23]. Taken together, these results suggest that the balance

between hydrophilic and hydrophobic regions in 4-PEG-PA-DCA greatly affect the pH-driven self-assembly of the polymeric construct.

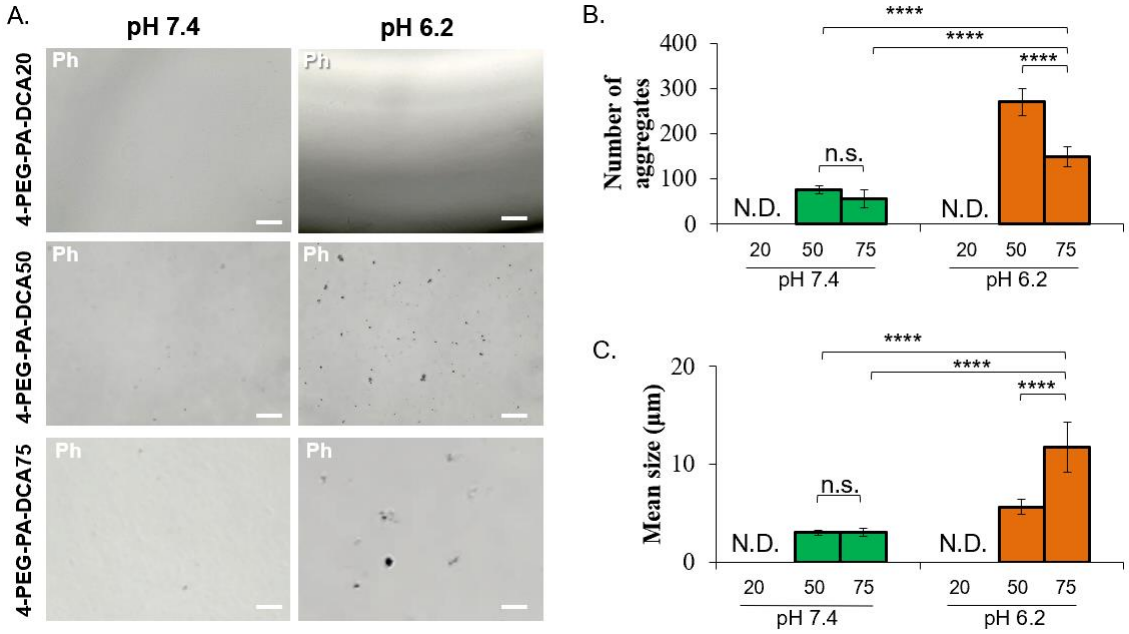

Figure 3-7. (A) Phase contrast (Ph) microscopy images of 4-PEG-PA-DCA20, 4-PEG-PA-DCA50 and 4-PEG-PA-DCA75 in PBS at 1 mg/mL at r.t.. Scale bar = 100 µm. (B) Average number of sub-micron-sized aggregates in Ph images of 4-PEG-PA-DCA20, 4-PEG-PA-DCA50 and 4-PEG-PA-DCA75 at 1 mg/mL in PBS at pH 7.4 and 6.2. The data are represented as means ± SD (n=50). (C) Average diameter of aggregates in Ph images of 4-PEG-PA-DCA20, 4-PEG-PA-DCA50 and 4-PEG-PA-DCA75 at 1 mg/mL in PBS at pH 7.4 and 6.2. N.D means "not detected". The data are represented as means ± SD (n=50). (**** $p \leq 0.0001$).

Figure 3-8 shows the expected mechanism of the self-assembly process at weak acid condition. The 4-PEG-PA-DCA20 and 4-PEG-PA-DCA50 showed aggregations with 220 nm at pH 7.4, probably due to the weak hydrophobic interactions of the terminal alkyne groups, whereas 4-PEG-PA-DCA75 indicated smaller size because of only one terminal alkyne group grafted per molecule, suggesting the monodispersity. At mild acidic condition, 4-PEG-PA-DCA can self-assemble due to the increased global hydrophobicity induced by the protonation of the carboxylic group of DCA. The protonated carboxylic group of DCA has the potential to form additional intermolecular hydrogen bonding, which further stabilize the formation of the aggregates. The diameter of the aggregates can be correlated to the content of DCA in the constructs because the intermolecular hydrophobic interactions between the DCA groups are increased. In the case of 4-PEG-PA-DCA20 and 50, they cannot form strong intermolecular hydrophobic interaction because of one or two DCA unit grafted per molecule. On the other hand, the higher content in DCA in 4-PEG-PA-DCA75 contributes to the formation of larger

nanometer-sized aggregates. When the DCA content is over 50%, the samples easily interact with neighboring nanometer-sized aggregated to grow over 5 or 10 μm, respectively.

These results suggest that the *in vivo* bioavailability of the MB could be potentially enhanced by the increased DS of DCA in 4-PEG-PA-DCA, as it might show less aggregation in the blood circulation than 4-PEG-DBCO-DCA. The size is indeed one of the most important design factors that must be optimized for the nano-formulation, since it directly affects their transport and tissue uptake. Their sizes should be optimally ranging from 10-100 nm to prevent the elimination by the kidneys and recognition by the immune response [24–26]. The size of 4-PEG-PA-DCA75 satisfy these criteria as it has a diameter around 35 nm at neutral condition.

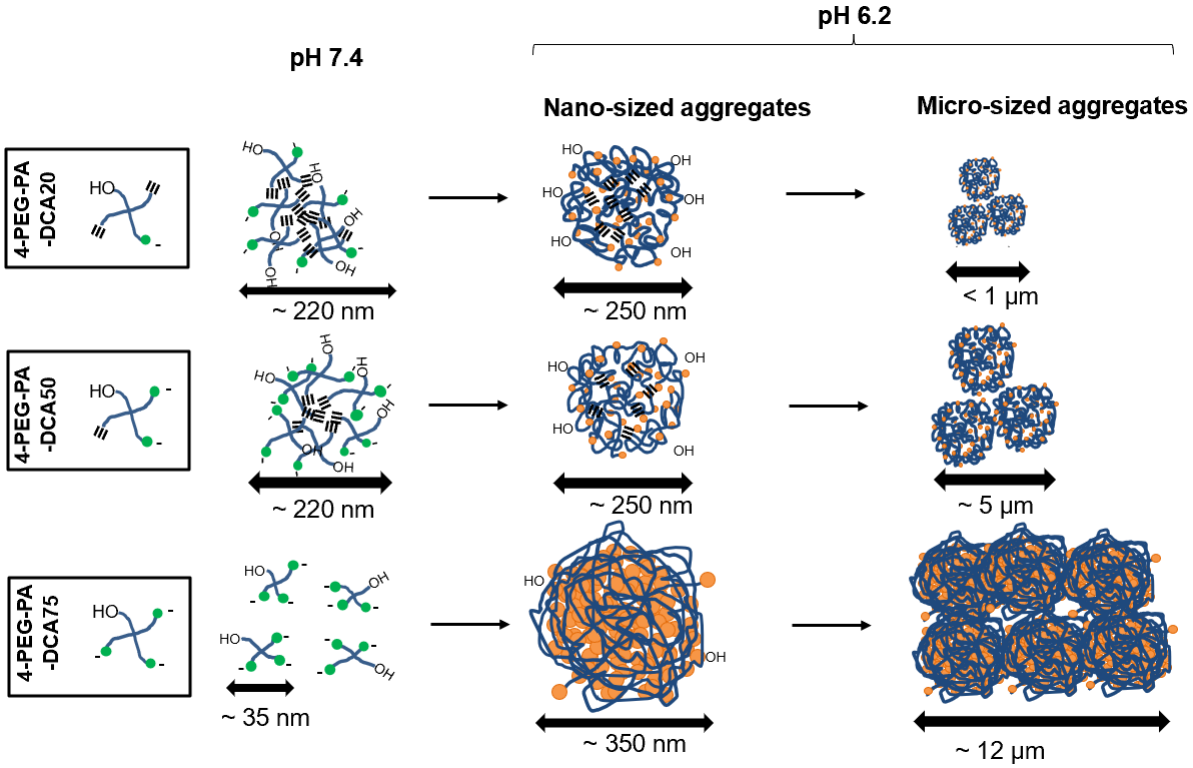

Figure 3-8. Proposed mechanism for the aggregation of 4-PEG-PA-DCA depending on the DS of DCA.

3.3.3. Cytotoxicity effect of 4-PEG-PA-DCA75 at weak acid condition

The 4-PEG-PA-DCA75 seems a promising candidate for cancer therapy due to the enhanced self-assembly properties at weak acidic condition, suggesting the induction of rapid and significant cytotoxicity at cancer tumor microenvironment. The cytotoxicity effect of 4-PEG-PA-DCA75 was assessed on *in vitro* monolayer cultures of various cell types, such as normal human dermal fibroblasts (NHDF) as a normal cell and two cancer cell lines (pancreatic cancer MiaPaCa-2 and colon cancer HT29) by incubating 4-PEG-PA-DCA75 at 1 mg/mL for 8 hours at pH 7.4 or pH 6.2 (**Figure 3-9**). The extracellular pH in the central region of tumors decreases at pH 6.7 and below because of lactate accumulation [27]. Since 2D cell cultures are unable to reproduce the pH gradients observed in solid tumors, we lowered the pH in cell culture media to pH 6.2 to mimic this process *in vitro*, and evaluated the cytotoxicity of 4-PEG-PA-DCA75. Importantly, 4-PEG-PA-DCA75 showed a low cytotoxicity at neutral conditions, with a dead cells percentage below 10% for all cell types (**Figure 3-9A**). The polymeric conjugates showed an enhanced cytotoxicity at weak acid conditions, as confirmed by the high percentage of dead cells (over 60%) and cells detachment after 8 h incubation (**Figure 3-9B**).

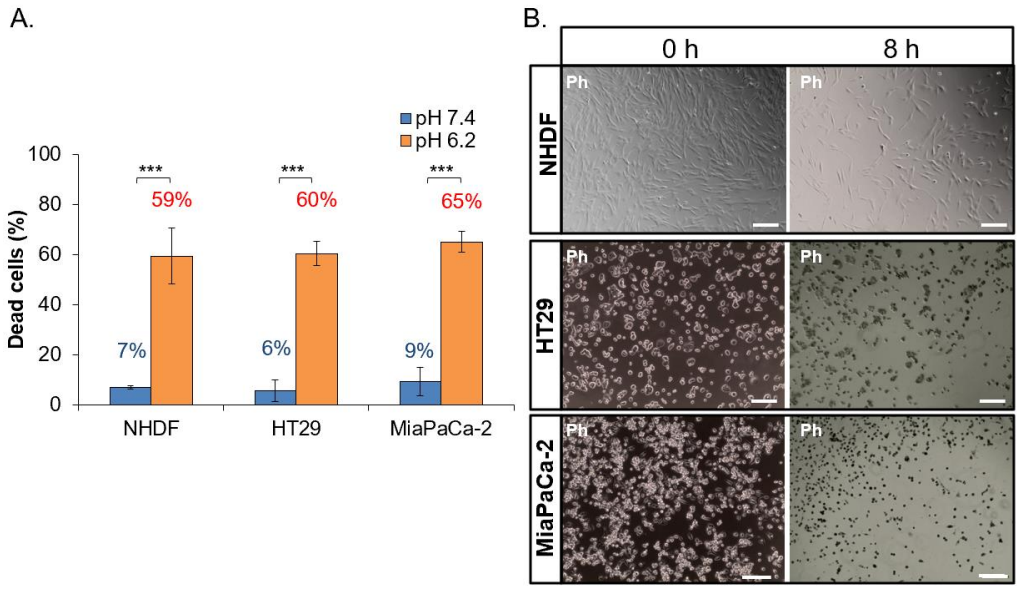

Figure 3-9. Cytotoxic effect of 4-PEG-PA-DCA75 at 1mg/mL on various cell types under neutral and weak acid conditions. (A) Dead cell percentage of Normal Human Dermal Fibroblast (NHDF), HT29 (colon cancer cell line) and MiaPaCa-2 (pancreas cancer cell line) at pH 7.4 (blue) and pH 6.2 (orange) after 8 h incubation with 4-PEG-PA-DCA75 at 37 °C. The data are represented as means ± SD (n=3) (*** $p \leq 0.001$). (B) Phase contrast images of NHDF, HT29 and MiaPaCa-2 before and after 8 h incubation with 4-PEG-PA-DCA75 at pH 6.2 at 37 °C. Scale bar = 200 μm.

The cytotoxicity of 4-PEG-PA-DCA75 was evaluated over the time by morphological assessment via phase contrast microscopy images. Cell started to detach and became round-shaped after 6 h treatment with 4-PEG-PA-DCA75 (**Figure 3-10A**). Interestingly, 4-PEG-PA-DCA75 showed a similar cytotoxicity to the previous MB but in much shorter time, within 8h. The previous 4-PEG-DBCO-DCA87 showed indeed an enhanced cytotoxicity only after 18-24 h incubation (**Figure 3-10B**) [14].

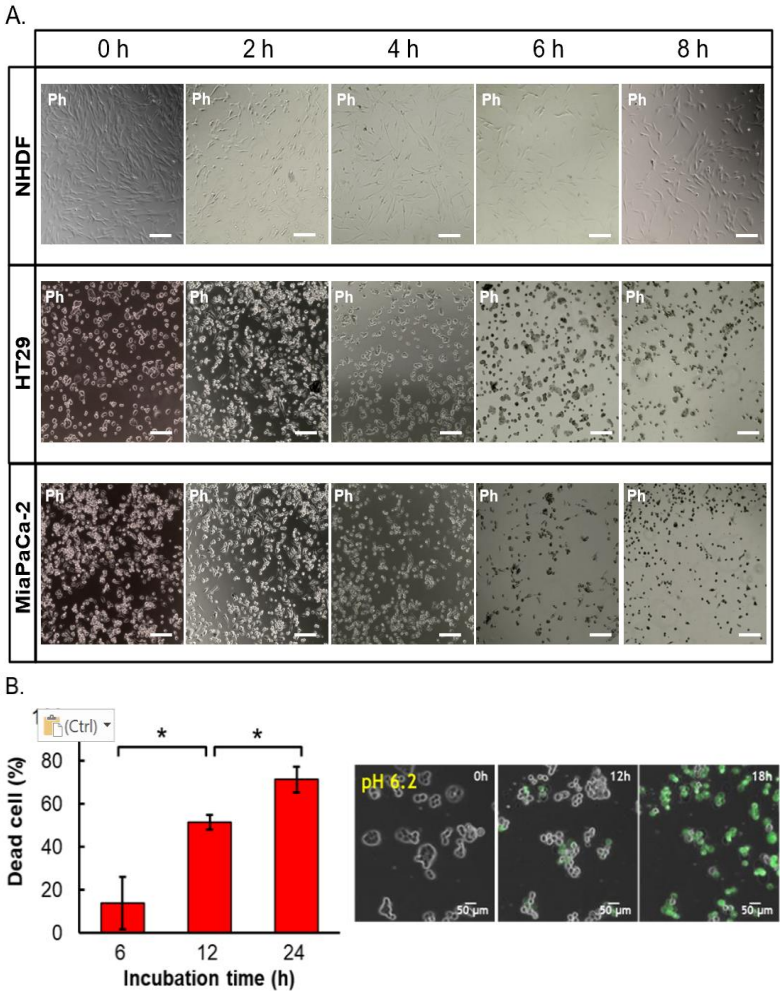

Figure 3-10. (A) Phase contrast images of NHDF, HT29 and MiaPaCa-2 with 4-PEG-PA-DCA75 at 1 mg/mL at pH 6.2 during 8 h incubation at 37 °C. (B) Time dependent change of dead cell percentage of HT29 treated with fluorescent labeled 4-PEG-DBCO-DCA at pH 6.2 (n=3). (* $p < 0.05$). Reproduced from Ref. [14] with permission from the Royal Society of Chemistry.

The difference in the time needed for the cell death induction between 4-PEG-DBCO-DCA87 and 4-PEG-PA-DCA75 may be potentially attributed to the difference in the hydrophobic and hydrophilic balance, leading to different stability of the aggregates in solution. The 4-PEG-DBCO-DCA87 indeed bears an excessive hydrophobicity resulting from the presence of the DBCO moiety, thus, it may show a lag period before the cell death induction due to the formation of stable micrometer-sized aggregates in the culture medium (**Figure 3-11**). The 4-PEG-DBCO-DCA87 might first self-assemble into large aggregates within short time which remain in solution for a certain period of time before reaching cell membrane and inducing its cytotoxic effects. Conversely, 4-PEG-PA-DCA could potentially form smaller aggregates in solution within a short amount of time, thus could initiate the self-assembly process into large aggregates directly on the cancer cell

surfaces to induce faster cell death. The exact mechanism of cancer cell death induction of 4-PEG-PA-DCA needs to be further investigated to confirm this hypothesis.

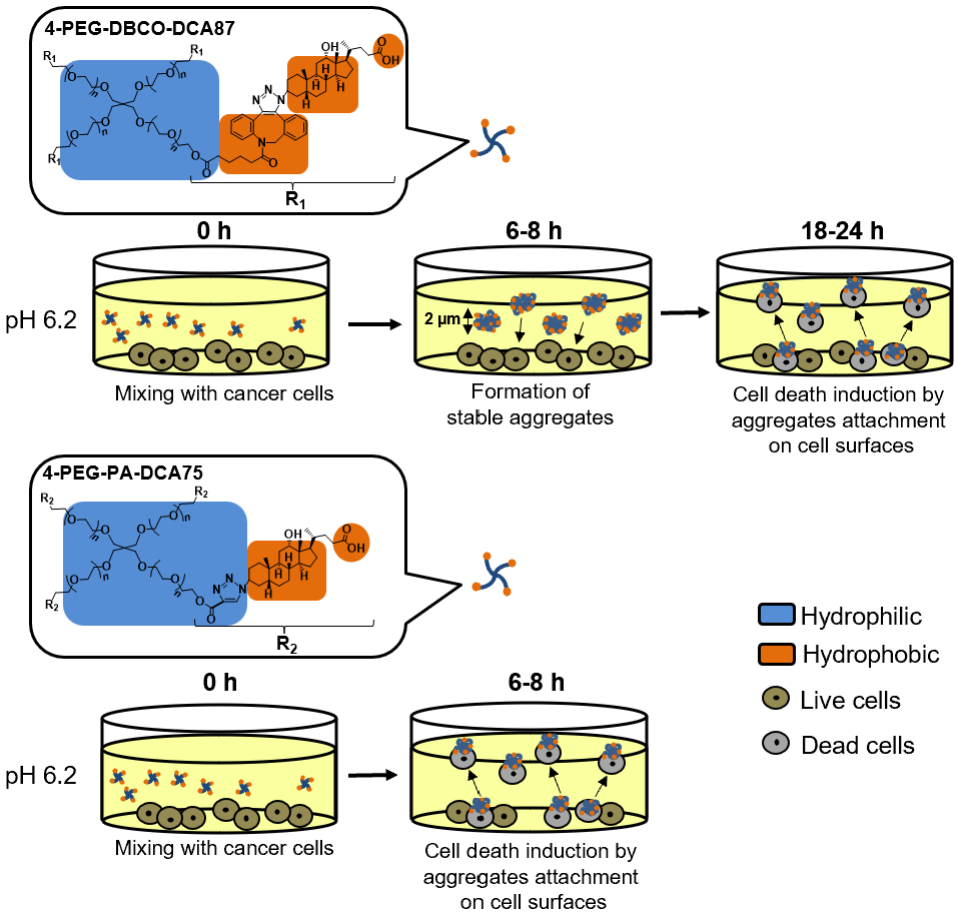

Figure 3-11. Expected mechanism of cell death induction for 4-PEG-DBCO-DCA and 4-PEG-PA-DCA at pH 6.2.

3.4. Conclusion

In summary, this study highlights the importance of the proper balance between the hydrophilicity-hydrophobicity for the formulation of the new MB. This parameter, finely tuned by different substitution degree of DCA, was shown to greatly affect the aggregation behavior. Importantly, we demonstrated three important characteristics of 4-PEG-PA-DCA75, including dispersion as a small particle at physiological conditions, pH-driven self-assembly and cell toxicity at acidic conditions. This "drug-free" MB seems promising for cancer therapy applications, including for the treatment of brain cancers.

3.5. References

[1] J. Shi, A. R. Votruba, O. C. Farokhzad, R. Langer, *Nano Lett* 2010, *10*, 3223.
[2] Y. Anraku, H. Kuwahara, Y. Fukusato, A. Mizoguchi, T. Ishii, K. Nitta, Y. Matsumoto, K. Toh, K. Miyata, S. Uchida, K. Nishina, K. Osada, K. Itaka, N. Nishiyama, H. Mizusawa, T. Yamasoba, T. Yokota, K. Kataoka, *Nature Communications* 2017, *8*, 1001.
[3] J. Guan, Z.-Q. Zhou, M.-H. Chen, H.-Y. Li, D.-N. Tong, J. Yang, J. Yao, Z.-Y. Zhang, *Acta Biomaterialia* 2017, *60*, 244.
[4] G. Wang, Z. Zhou, Z. Zhao, Q. Li, Y. Wu, S. Yan, Y. Shen, P. Huang, *ACS Nano* 2020, *14*, 4890.
[5] Y. Wang, B. Lei, M. Sun, X. Han, S. Xu, H. Liu, *Macromolecular Chemistry and Physics* 2020, *221*, 1900536.
[6] G. Wang, B. Wu, Q. Li, S. Chen, X. Jin, Y. Liu, Z. Zhou, Y. Shen, P. Huang, *Small* 2020, *16*, 2004172.
[7] S.-Y. Wu, H.-Y. Chou, C.-H. Yuh, S. L. Mekuria, Y.-C. Kao, H.-C. Tsai, *Advanced Science* 2018, *5*, 1700339.
[8] F. Alexis, E. Pridgen, L. K. Molnar, O. C. Farokhzad, *Mol Pharm* 2008, *5*, 505.
[9] H. Maeda, H. Nakamura, J. Fang, *Advanced Drug Delivery Reviews* 2013, *65*, 71.
[10] S. Wilhelm, A. J. Tavares, Q. Dai, S. Ohta, J. Audet, H. F. Dvorak, W. C. W. Chan, *Nature Reviews Materials* 2016, *1*, 1.
[11] D. Rosenblum, N. Joshi, W. Tao, J. M. Karp, D. Peer, *Nature Communications* 2018, *9*, 1410.
[12] A. Tanaka, Y. Fukuoka, Y. Morimoto, T. Honjo, D. Koda, M. Goto, T. Maruyama, *J. Am. Chem. Soc.* 2015, *137*, 770.
[13] J. Wang, L. Li, J. Yang, P. M. Clair, M. J. Glenn, D. M. Stephens, D. C. Radford, K. M. Kosak, M. W. Deininger, P. J. Shami, J. Kopeček, *Nanomedicine: Nanotechnology, Biology and Medicine* 2019, *16*, 217.
[14] H. Nakatsuji, Y. Shioji, N. Hiraoka, Y. Okada, N. Kato, S. Shibata, I. Aoki, M. Matsusaki, *Mater. Horiz.* 2021, DOI 10.1039/D0MH02058C.
[15] D. J. Cabral, D. M. Small, in *Comprehensive Physiology*, American Cancer Society, 2011, pp. 621–662.
[16] J. L. Wike-Hooley, J. Haveman, H. S. Reinhold, *Radiotherapy and Oncology* 1984, *2*, 343.
[17] Z. Li, T. S. Seo, J. Ju, *Tetrahedron Letters* 2004, *45*, 3143.
[18] V. X. Truong, M. P. Ablett, H. T. J. Gilbert, J. Bowen, S. M. Richardson, J. A. Hoyland, A. P. Dove, *Biomaterials Science* 2014, *2*, 167.
[19] O. S. Fenton, J. L. Andresen, M. Paolini, R. Langer, *Angewandte Chemie* 2018, *130*, 16258.
[20] M. Wilhelm, C. L. Zhao, Y. Wang, R. Xu, M. A. Winnik, J. L. Mura, G. Riess, M. D. Croucher, *Macromolecules* 1991, *24*, 1033.
[21] R. Ninomiya, K. Matsuoka, Y. Moroi, *Biochimica et Biophysica Acta (BBA) - Molecular and Cell Biology of Lipids* 2003, *1634*, 116.
[22] G. Basu Ray, I. Chakraborty, S. P. Moulik, *Journal of Colloid and Interface Science* 2006, *294*, 248.
[23] K. Y. Lee, W. H. Jo, I. C. Kwon, Y.-H. Kim, S. Y. Jeong, *Macromolecules* 1998, *31*, 378.
[24] N. Hoshyar, S. Gray, H. Han, G. Bao, *Nanomedicine (Lond)* 2016, *11*, 673.
[25] A. B. de Barros, A. Tsourkas, B. Saboury, V. N. Cardoso, A. Alavi, *EJNMMI Research* 2012, *2*, 39.
[26] A. H. Faraji, P. Wipf, *Bioorganic & Medicinal Chemistry* 2009, *17*, 2950.
[27] O. Warburg, *Science* 1956, *123*, 309.

Concluding remarks

In this study was demonstrated the ability to prepare a 3D BBB model suitable for the high-throughput screening of polymeric anti-cancer drugs.

In chapter 1, a 3D BBB capillary network with perfusable opening structures was fabricated in versatile commercially available transwell culture system. This model would not require any special equipment, and would thus be easier and faster to set up than current microfluidic platforms for HTS. Controlling the capillary organization and opening in our BBB model was beneficial for the functional assessment of TfR by permeability assays. This model also demonstrates sufficiently low paracellular permeability to enable a size-selective transport of different molecular weight of dextran. The activity of the P-gp efflux pump was then validated using the specific substrate Rhodamine 123 which showed a preferential transport from the "brain" side to the "blood" side. Finally, the functionality of specific transport systems, such as the transferrin receptor (TfR), was confirmed by competition assays using its native ligand, transferrin, and permeability assays using TfR-targeted antibodies. Effective permeability coefficient (P_e) value of transportable TfR antibody (MEM-189) was 7-fold higher than the P_e value of isotype antibody (IgG1) and low transportable antibody (13E4), suggesting a higher functional and efficient TfR-mediated transport as compared to the other previous reports. By mimicking several features of the native BBB in a user-friendly manner, our model shows potential to be used as a platform for screening of CNS drugs transported across the BBB. Immortalized cell lines of the three BBB cell types were preferred for the preparation of the model due their robustness and reproducibility, which are indeed desired by pharmaceutical companies for HTS assays. However, this model did not show sufficient paracellular tightness as compared to the native BBB, which is highly desired for the accurate assessment of the transportability of small-sized drugs. Changing the BMEC source in this 3D BBB model could offer opportunities for BBB modelling by enhancing the BBB properties in order to obtain more accurate evaluation of small drug permeation across the BMEC network.

Chapter 2 demonstrated that hiPS-BMEC could represent a better alternative than HBEC to reproduce *in vitro* the functional properties of the native BBB endothelium, particularly regarding the paracellular tightness. The use of hiPS-BMEC in BBB modelling could be beneficial for a more accurate evaluation of the permeation of both small-sized and large-sized therapeutics, due to the restricted paracellular transport. Even though both cell types

globally showed the same trend in the permeability of the tested molecules, HBEC exhibited an additional paracellular transport of large-sized molecules compared to hiPS-BMEC, due to their weak expression of tight junctions. The leakiness properties of HBEC are therefore not suitable for the accurate measurement of the permeability of tested molecules, which is fundamental for improving *in vitro* drug testing accuracy and the "bench-to-bedside'' transition of brain cancer drugs. Additionally, the permeability of two peptides transported by the RMT pathway was also confirmed, with a higher permeability of the cys-T7 peptide than the cys-Tfr-T12 peptide by hiPS-BMEC. The cys-T7 peptide could therefore serve as an efficient targeting moiety to enhance the delivery of therapeutics through the BBB endothelium. Additionally, although cell monolayer is a handful model to directly study inherent properties of HBEC and hiPS-BMEC, the incorporation of astrocytes and pericytes could be useful to represent more closely native-like environment. The BBB functions of cocultured BMEC with astrocytes and/or pericytes were found to be greater than those of monocultured ones, including the upregulation of the expression of TJ and transporters, such as the TfR. The incorporation of human astrocytes and pericytes could enhance even more the functional properties of the monoculture model of hiPS-BMEC used in this study. The increased complexity of this *in vitro* model would greatly benefit the study of the passage of molecules mediated by the TfR, such as the TfR-targeted antibodies and peptides used in this study, as it would more closely recapitulate the native structure of the brain endothelium. Future work remained to be done to determine whether hiPS-BMEC could form the same perfusable network with open structures in a 3D configuration and compared the functionality of the model with the results obtained in Chapter 1.

In Chapter 3, we synthesized a cancer-microenvironment responsive drug-free chemotherapy, named 4-PEG-PA-DCA, which displayed better dispersion as a small particle at physiological conditions, higher pH-driven self-assembly and faster cell toxicity at acidic conditions than previously reported 4-PEG-DBCO-DCA. The 4-PEG-PA-DCA could potentially serve as a template molecule for the fabrication of drug-free chemotherapy treating brain diseases which could be screened in a tumor model of the 3D BBB open capillary network. For example, a TfR targeting moiety, such as the cys-T7 peptide screened in chapter 2, could be grafted in the 4-PEG-PA-DCA for an improved BBB crossing ability and enhanced brain tumor targeting (**Figure 1**). The expected construct, named BBB-MB, could be potentially screened in a human BBB tumor model incorporating cancer cells for assessing its BBB

crossing ability mediated by the TfR as well as the targeting efficiency and cytotoxic effect on the cancer cells.

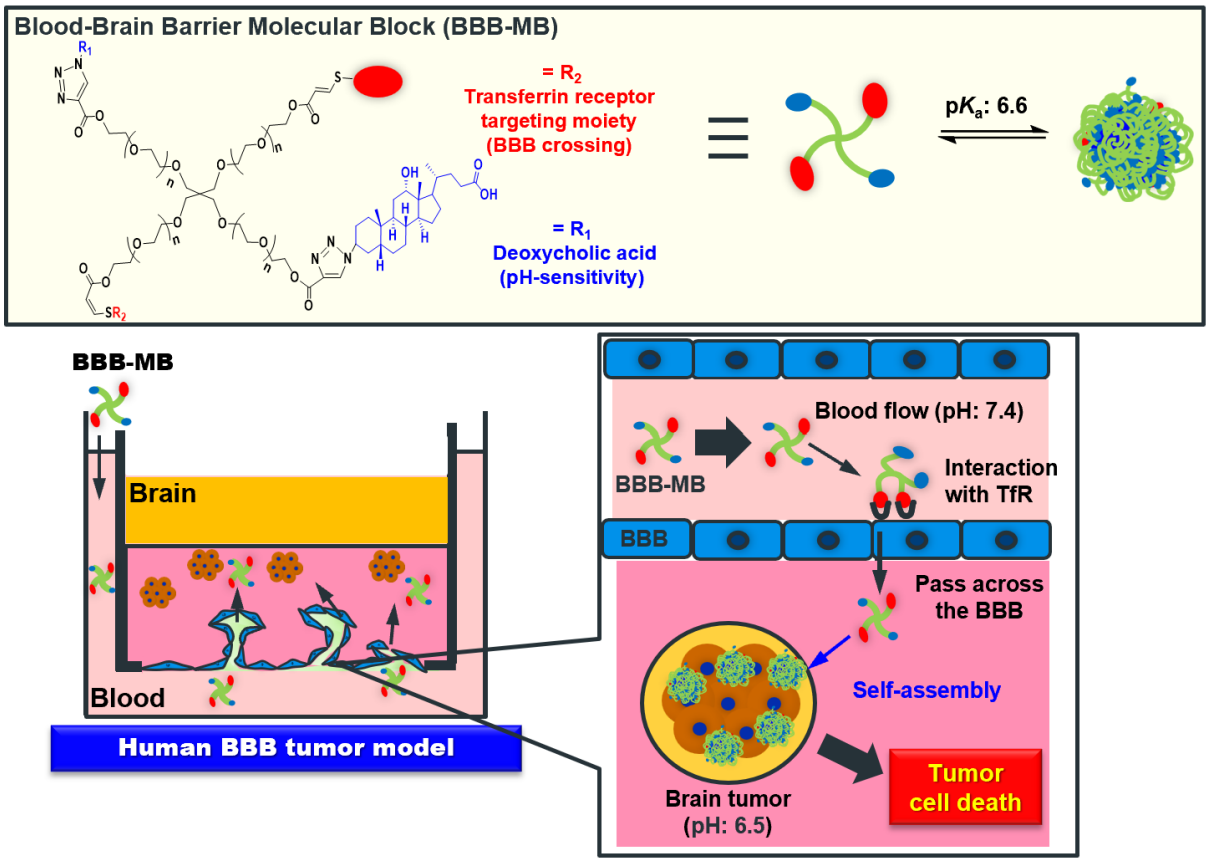

Figure 1. Development of BBB Molecular Block (BBB-MB) for brain tumor treatment.

List of publications

Chapter 1

Development of a three-dimensional blood-brain barrier network with opening capillary structures for drug transport screening assays

Marie Piantino, Dong-Hee Kang, Tomomi Furihata, Noriyuki Nakatani, Kimiko Kitamura, Yukari Shigemoto-Mogami, Kaoru Sato, Michiya Matsusaki

Mater. Today Bio **2022**, 15, 100324.

Chapter 2

Brain microvascular endothelial cells derived from human induced pluripotent stem cells as *in vitro* model for assessing blood-brain barrier transferrin receptor-mediated transcytosis

Marie Piantino, Fiona Louis, Yukari Shigemoto-Mogami, Kimiko Kitamura, Kaoru Sato, Tomoko Yamaguchi, Kenji Kawabata, Syunsuke Yamamoto, Shinji Iwasaki, Hideki Hirabayashi, Michiya Matsusaki

Mater. Today Bio **2022,** 14, 100232.

Chapter 3

Development of Highly Sensitive Molecular Blocks at Cancer Microenvironment for Rapid Cancer Cell Death

Marie Piantino, Masahiko Nakamoto, Michiya Matsusaki

Langmuir **2022,** 38, 17, 5209–5217.

Supplementary publications

1. Interstitial flow regulates *in vitro* three-dimensional self-organized brain micro-vessels
   Agathe Figarol, **Marie Piantino**, Tomomi Furihata, Taku Satoh, Shinji Sugiura, Toshiyuki Kanamori, Michiya Matsusaki
   Biochem. Biophys. Res. Commun. **2020**, 533, 600-606.

2. Three-Dimensional *in vitro* Models of Healthy and Tumor Brain Microvasculature for Drug and Toxicity Screening
   Marie Piantino, Agathe Figarol, Michiya Matsusaki
   Front. Toxicol. **2021**, 3, 656254.

3. Bioprinted Vascularized Mature Adipose Tissue with Collagen Microfibers for Soft Tissue Regeneration

   Fiona Louis, **Marie Piantino**, Hao Liu, Dong-Hee Kang, Yoshihiro Sowa, Shiro Kitano, and Michiya Matsusaki

   Cyborg bionic syst. **2021**, 1412542, 15.

Acknowledgements

This study was carried out from 2019 to 2022 at Department of Applied Chemistry, Graduate School of Engineering, Osaka University. In the past three years, I have received a lot of assistance and support during my thesis and daily life. I would like to thank all the people who contributed in some way to the work described in this thesis.

Foremost, I would like to express my sincere gratitude to my supervisor, Prof. Michiya Matsusaki for the continuous support over the last three years, for his patience, motivation, enthusiasm on research. His guidance helped me in all the time of research and writing of the manuscript and this thesis. His support and immense knowledge in this field have made this an inspiring experience for me.

I am deeply grateful to the thesis committee: Prof. Toshiyuki Kida and Prof. Kazuya Kikuchi, who generously provided knowledge and expertise. I would like to express my deepest appreciation to Mr. Syunsuke Yamamoto, Mr. Hideki Hirayabashi, Mr. Shinji Iwasaki from Takeda Pharmaceutical Company for their insightful comments and suggestions in the experiment, data discussion and article writing. Thanks to Prof. Tomomi Furihata in School of Pharmacy, Tokyo University of Pharmacy and Life Sciences (Hachioji, Tokyo) Japan for providing the three BBB cell lines (HBEC, HA, HP). Thanks to Prof. Kenji Kawabata in National Institutes of Biomedical Innovation, Health and Nutrition (Ibaraki, Osaka) for providing the HiPS-BMEC used in this work.

Besides my supervisor, I am also deeply grateful to Assistant Prof. Masahiko Nakamoto and Assistant Prof. Kenta Homma, and Specially Appointed Assistant Prof. Fiona Louis for their insightful comments and suggestions for my research. Thanks Dr. Dong-Hee Kang, Dr. Agathe Figarol, Dr. Naoko Sasaki, Dr. Jinfeng Zeng, Dr. Zhengtian Xie, Dr. Hirotaka Nakatsuji and for their comments, suggestions and guidance to my experiments.

I would like to offer my special thanks to Ms. Eri Enomoto, Ms. Chika Sugiki, and Ms. Kiyomi Lee for their kind support and help in the laboratory affairs, scholarships application and daily life.

My appreciation also goes to the previous and current fellows in Matsusaki laboratory: Thanks to visiting researcher Asuka Kato, Yasuyuki Naito, Yuka Yoshinouchi, Keisuke Sumiyoshi, and Mizuho Suzuki. Thanks to Ms. Yukiko Sorayama, Mr. Yasuhiro Naka, Mr. Yuichi Yukawa,

Mr. Hao Liu, Ms. Jinyu Li, Mr. Kazuma Ishiguro, Mr. Noboru Hiraoka, Ms. Suphanun Phuphanitcharoenkun, Mr. Abdul Sisak Muhammad Asri, Mr. Yucheng Shang, Ms. Asli Sena Karanfil, Ms. Zhang Zhuying, Mr. Daisuke Tomioka, Mr. Tomoyuki Suezawa, Ms. Yuning Zhang, Ms. Lingyu Pei, Mr. Shogo Shimada, Mr. Ryo Mitsuyasu, Mr. Rei Miyata, Mr. Yuki Koba, Mr. Tomoya Matsuo, Mr. Kazuki Moroishi, Mr. Kazuki Yoshida, Ms. Nozomi Kasahara, Mr. Tamaki Kumauchi, Ms. Sukulya Bunuasunthon, Mr. Ryosuke Isobe, Mr. Yusuke Kajiura, Mr. Rentaro Sakamoto, Ms. Misa Miyamoto, Ms. Kaori Hayazaki, Ms. Wu Chun-Yi, Mr. Ryoto Itani, Mr. Kanta Iwamoto, Ms. Itsuki Miyaguni, Ms. Aya Nagura, and Ms. Hong Young Kyoung. Thanks to their accompany and kind support for both research and daily life.

I would like to acknowledge the financial supporting from Otsuka Toshimi Scholarship Foundation and from Japan Student Services Organization (JASSO) who provide me with the financial means for living in Japan. And finally, thanks to my parents and friends who endured this long process with me, always offering support and love.

June 2022

PIANTINO MARIE VIRGINIE